Electron, Positron and Photon Polarimetry

ISBN: 90-367-0737-4

This work was performed as part of the research program of the 'Stichting voor Fundamenteel Onderzoek der Materie' (FOM), which is financially supported by the 'Nederlandse organisatie voor Wetenschappelijk Onderzoek' (NWO).

Afbeelding omslag: Henrietta Harkink.

Drukwerk: Stichting Drukkerij C. Regenboog, Groningen.

RIJKSUNIVERSITEIT GRONINGEN

Electron, Positron and Photon Polarimetry

Proefschrift

ter verkrijging van het doctoraat in de
Wiskunde en Natuurwetenschappen
aan de Rijksuniversiteit Groningen
op gezag van de Rector Magnificus, dr F. van der Woude,
in het openbaar te verdedigen op vrijdag 23 mei 1997
des namiddags te 4.15 uur

door

Johannes Marinus Hoogduin

geboren op 6 januari 1967 te Emmeloord

Promotor: Prof. dr R. H. Siemssen
Co-promotor: Dr J. van Klinken

Voor mijn ouders

Acknowledgements

The work presented in this thesis would not have been possible without the involvement of a number of people. I would like to thank the following persons in particular:

Johan van Klinken, my supervisor, who was involved in every aspect of this project from day number one. His creativity and never ending stream of ideas led to the polarimeter which is discussed in this thesis. His enthusiasm was very stimulating. I also enjoyed travelling to Germany with him. I shall not easily forget our visit to the 'Dillenburg', located on top of a steep hill, with a van loaded with electronics.

Rolf Siemssen, my 'promotor', for his critical questions about the research and his suggestions which led to an improved presentation of the results.

Prof. dr J. Deutsch, Prof. dr D. Atkinson and Dr W. Fetscher, the 'reading committee', for reading and giving their comments on the manuscript.

Eric Schooneveld, who built the silicon strip detectors and associated electronics. He also joined us during the experiments in Frankfurt.

Hans Wilschut, who taught me a lot on electronics and data acquisition for nuclear physics. He also commented on an early version of chapter 5 and 6.

Kurt Stiebing, Oliver Fröhlich and Alkis Müller, 'die Mannschaft von Herrn Baumgarten' and Herr W. Theisinger from the workshop all at the Institut für Kernphysik for their help and hospitality during our visits in Frankfurt.

Klaus Flöttmann for reading and commenting on chapter 3 and 4. I learned a lot from his work on incorporating polarization transfer for Compton

scattering, bremsstrahlung and pair production in EGS4.

Rob Timmermans for reading chapter 3.

The people and colleagues at the KVI who helped me whenever I asked them.

The students who joined us to do their 'experimental research for theoreticians'. Their questions improved my knowledge on the subjects they worked on.

Albert, Dick, Esther, Paul and last but not least Treja for their critical reading of the Dutch summary.

Hans Hoogduin Groningen, april 1997.

Contents

Chapter 1

A new polarimeter

It is remarkable that it is more difficult to think of methods of detecting polarization, which seems apt for realization, than of methods of producing polarization. *H.A. Tolhoek [1]*

The above quotation is taken from the classic and often cited review on "Electron Polarization, Theory and Experiment" by Tolhoek [1] published 40 years ago. The field has changed since then. However, the number of *realized* methods to detect the polarization of electrons and photons is still limited and remains mostly restricted to lower energies (below 10 MeV) or to the very high energies (GeV regime).

This thesis describes a search for possibilities to arrive at novel polarimetry for electrons, positrons and photons in the less accessible energy regime from 10 to 100 MeV. The main idea is to develop a polarimeter whose sensitivity is increased by incorporating several polarization sensitive processes in one device and by placing multiple scattering layers behind each other in one and the same polarimeter.

In the literature only few polarimeters operating in the energy range between 10 and 100 MeV [2, 3] can be found. At lower energies Mott scattering is generally used. In the past Mott scattering played an important role at energies below 1 MeV. The 'fall of parity' in β decay was experimentally studied by using Mott scattering. See for example the work of van Klinken [4] and the overview in the book of Kessler [5]. Recently, Sromicki et al. [6] obtained results for energies up to 14 MeV. With the advent of polarized high-energy (>100 MeV) electron beams, other types of polarimeters suitable for this energy regime were developed. They are either based on Møller

scattering (see for example [7, 8]) or Compton scattering (see for example [9]). In chapter 2 a general introduction to and an overview of polarimetry methods will be given.

1.1 Motivation for a new polarimeter

The motivation to consider the feasibility of a novel polarimeter originated during the planning of proton-proton-bremsstrahlung experiments with polarized proton beams at the KVI-Groningen. Such studies are presently restricted to measurements of the analyzing power of the nucleons participating in the reaction. Here attention is directed to the possibility of performing polarimetry with the emitted photon. In the '$\vec{p}p\gamma$ experiment' [10], at present ongoing with the first polarized proton beams of the new KVI accelerator AGOR, a beam of polarized protons of 200 MeV is interacting with a liquid hydrogen target. The scattered and recoiling protons are measured in coincidence with bremsstrahlung photons of around 50 MeV. The experiments are intended to provide valuable information on the off-shell nucleon-nucleon interaction by measuring the analyzing power. However, it was expected, and confirmed by calculations [11], that the polarization of the bremsstrahlung photon also contains information on the off-shell behaviour of the interaction. Photon polarimetry could thus provide a novel, and so far not yet pursued, approach to study the nucleon-nucleon interaction.

The use of the envisioned polarimeter is not restricted to photons but may also be extended to electrons and positrons. This possibility allows an extension of the concept to 'electromagnetic polarimetry'. For example, it might be incorporated in muon decay experiments planned at PSI in Switzerland [12, 13].

1.2 The proposed polarimeter

Electromagnetic polarimetry at energies of several tens of MeV has thus far hardly been pursued because the polarization sensitive methods are characterized by a decreasing efficiency with increasing energy. One of the few experiments with photons found in the literature was done by Garwin and co-workers [2] as early as 1957. Their aim was to determine the circular polarization of 70 MeV photons emitted by neutral pions. The detector used in

their pioneering experiment was based on the spin dependence of Compton scattering of photons in magnetized iron. Because Compton scattering is not the most dominant process in photon interactions with matter at 70 MeV the resulting detector efficiency is low. Pair production, the dominating process at these energies, is in theory polarization sensitive but in practice difficult to use (see chapter 2 and 3). However, in pair production part of the circular polarization of the photon is transferred to the electrons and positrons. The secondaries are partly longitudinally polarized: this opens the way to polarimetry based on Møller and Bhabha scattering and the annihilation process.

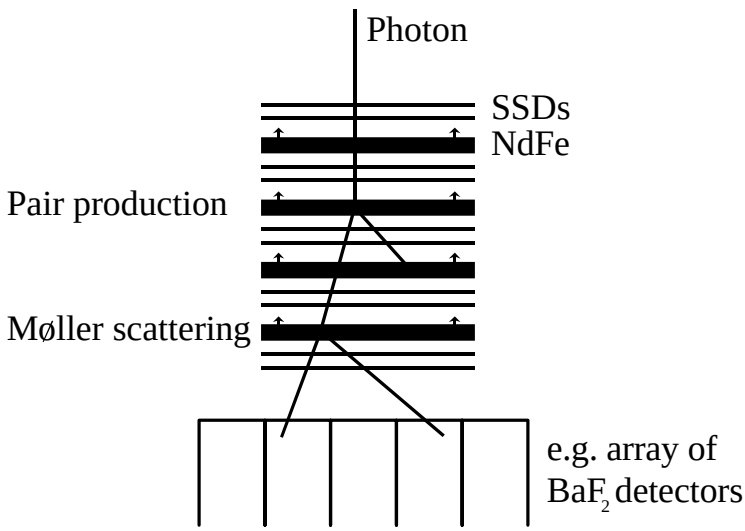

Figure 1.1: *The multilayer polarimeter using NdFe scattering foils. The BaF_2 detectors are included to reconstruct the full energy of the primary photons (or electrons) and to provide a trigger for the silicon strip detectors (SSDs; see 6.2). The arrows symbolize the magnetization direction of the NdFe target.*

This leads to a polarimeter concept as sketched in figure 1.1. It consists of magnetic neodynium iron ($Nd_2Fe_{14}B$; in short notation NdFe) layers sandwiched between position sensitive silicon strip detectors (SSDs). Three aspects are novel in this polarimeter: First, the use of a permanent magnet as scattering target, second, the use of SSDs to detect the scattering processes, and third, the multilayer approach.

The soft magnetic iron foil of the Garwin experiment is replaced by layers of hard magnetic NdFe. This has two advantages: First, an NdFe layer can be magnetized perpendicularly to its plane (which is impossible when using soft magnetic materials in weak external magnetizing fields). And second, the NdFe does not need magnetizing coils. The NdFe layers can have thicknesses of about 1 mm. Usually, a thin permanent magnet has its magnetization direction *in* the plane of the material rather than *perpendicular* to it. Magnetization perpendicular to the surface became possible with the appearance of magnetic materials featuring large coercive forces. Such magnets can be made from materials containing rare earth elements, well known compounds being $SmCo_5$ and $Nd_2Fe_{14}B$.

The SSDs in between the layers of neodynium iron offer the possibility to localize and recognize the polarization sensitive interactions on an event-by-event basis. The silicon detectors give no signal when a photon passes through them, while a minimal ionizing electron loses a well-defined amount of energy. The different interactions in the NdFe layers like Compton scattering, Møller/Bhabha scattering, positron annihilation, pair production and bremsstrahlung can be discriminated on the basis of the number of particles observed with the SSDs before and after the magnetized layer. For example, the pair production occurring in the electromagnetic shower shown in figure 1.1 is identified by the absence of signals in the SSDs before the process occurs and the presence of signals of two particles afterwards. The Møller interaction is identified by detecting one particle before the scattering event and two particles after it.

The multilayer design increases the efficiency of the polarimeter in two ways. First, the chance that a particle interacts in the polarimeter is increased and second, by opening the possibility of detecting the polarization after the polarization is transferred from the primary particle to its secondaries in the electromagnetic shower.

Two aspects of the new polarimeter concept are investigated in this thesis:

1 The suitability of neodynium iron as polarimeter target material.

2 The above outlined scheme to discriminate the various relevant interactions.

1.3 Towards a new polarimeter

The feasibility of the polarimeter was investigated by designing and constructing one basic element of the detector. In the prototype one layer of NdFe is sandwiched between four SSDs, two on either side providing two-dimensional position detection. Tests were performed with fully longitudinally polarized electrons and positrons from β-decay sources with energies up to 16 MeV in an effort to demonstrate the polarimeter capability of the layer in its low-energy regime. Experiments with a ^{106}Ru/Rh -source (endpoint energy 3.5 MeV) and online produced ^{12}N- (16.4 MeV) and ^{12}B-sources (13.4 MeV) are discussed in chapter 6. Properties of NdFe and other rare earth based magnetic materials are the subject of chapter 5.

Until recently technological constraints prevented the utilization of the various polarization sensitive processes in the way outlined above (NdFe was not available, there were no SSDs). The QED-theory for most of these processes was, however, available. It was developed before 1965 and will be presented in chapter 3 in a uniform way using the Stokes parameters [14, 15, 16].

Simulations play an important role in both the design and analysis of experiments. The Monte Carlo method is widely used and is applied in chapter 6. The GEANT [17] package contains all the relevant electromagnetic processes playing a role in the polarimeter. However, no polarization transport is included in this code. The implementation of the polarization phenomena discussed in chapter 3 in GEANT 3.21 is discussed in chapter 4. Both polarization transfer and scattering asymmetries can be simulated with the extended version of the package. The work was partly inspired by and in continuation of ideas and developments in the work of den Bok [18] and Flöttmann [16].

With the extended version of GEANT the experiments with the ^{106}Ru/Rh source are simulated and the behaviour of the basic detector layer at particle energies of up to 90 MeV is investigated. The simulations provide information on the event recognition capabilities and offer a way to estimate the polarization sensitivity of the polarimeter. The results are presented and compared with the explorative measurements in chapter 6.

Chapter 7 summarizes the main conclusions and gives an outlook on future research.

1.4 Results

The efforts to show the polarization capability of the prototype polarimeter did not yet result in a clear demonstration of the polarization sensitivity. The measurements with the ^{106}Ru/Rh -source did not reveal a statistically significant polarization asymmetry. Monte Carlo simulations explain that this lack of asymmetry is caused by a large non-polarization sensitive background which reduces the expected effect to below the detection limit of the polarimeter. The background is caused by non-NdFe-target related scattering events. The low energy (<3.5 MeV) of the electrons from the ^{106}Ru/Rh-source made the use of a thin NdFe-target (0.5 mm) necessary. This resulted in a relatively large contribution from events originating in the SSDs. The time available for the experiments with the ^{12}B- and ^{12}N-sources was insufficient (two weeks) to be conclusive and to overcome the unexpected problems with the beam and target conditions and the SSD electronics in an accelerator environment. Background radiation related to the source production made a measurement of the scattering asymmetry impossible. The conclusions from these data are discussed in chapter 6. Simulations with mono-energetic electrons and photons with energies of 10 MeV and more indicate that further work on the polarimeter for these energies is promising. The simulations are presented at the end of chapter 6.

Chapter 2

Electron, positron and photon polarimetry: an overview

After introducing the basics of polarimetry, an overview of the available polarimetry methods is presented in this chapter. The discussion is done along the line of increasing energy: starting with methods for polarimetry at keV energies and ending at GeV energies. The discussion of polarimetry of electrons and positrons and the discussion of the polarimetry of photons is combined to a large extent. Such a combined treatment is natural when electromagnetic showers occur as is the case for the polarimeter under consideration. Also no strict division is made between longitudinal (or circular) and transverse (or linear) polarimetry. Examples of polarimeters which contain aspects that play a role in the polarimeter of figure 1.1 are presented in italics.

2.1 Polarimetry basics

2.1.1 Polarization of beams

In chapter 3 the describtion of the polarization of electron, positron and photon beams will be presented in detail. For the time being it is assumed that the polarization of a beam can be described by a vector $\vec{P}$. The orientation of the vector determines the polarization direction and the length of the vector determines the degree of polarization. If $|\vec{P}| = 1$ the beam is fully polarized, if $|\vec{P}| = 0$ the beam is unpolarized and for values between 0

and 1 the beam is partially polarized. If the vector is parallel or anti-parallel to the direction of motion of the beam particles, it is called a longitudinally polarized beam if the particles are electrons or positrons and a circularly polarized beam for photons. If the vector is perpendicular to the direction of motion the terminology used is transversely and linearly polarized for electrons/positrons and photons, respectively. In general, the beam polarization has both a longitudinal (or circular) and transverse (or linear) component.

2.1.2 Detection of polarization

There are several ways to detect the polarization of electron, positron and photon beams, depending among other things on beamenergy, beamflux and background radiation. Figure 2.1 schematically shows the basic features of

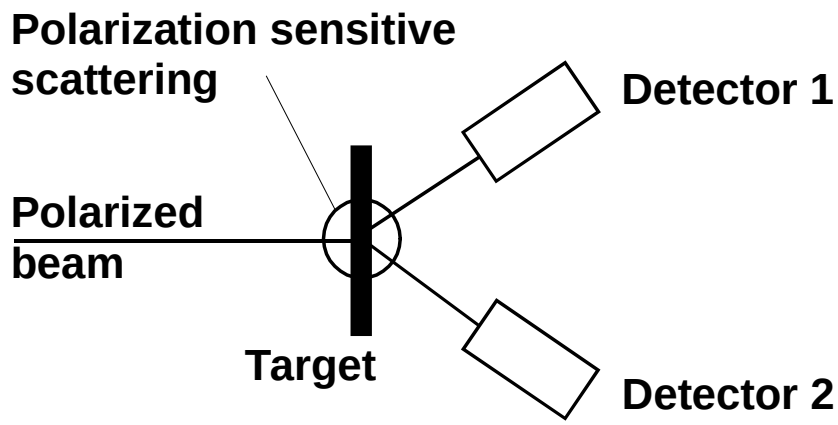

Figure 2.1: *Basic polarimeter*

a polarimeter with a beam of unknown polarization $\vec{P}_b$, a scattering target which, if it contains polarized electrons, has polarization $\vec{P}_t$ and a set of detectors to *select* the desired polarization dependent scattering process. A scattering target with polarized electrons is usually made of magnetized iron of which the magnetization can be reversed periodically. Sometimes the target is replaced by a beam as is the case with the high energy Compton polarimeters discussed in section 2.5.1

If the beam is polarized and the differential cross section is polarization sensitive the two detectors 1 and 2 will have different countrates $N_1 = N_l$

and $N_2 = N_r$. The so called 'left-right asymmetry' [1] resulting from these countrates is defined as

$$\delta_{\rm lr} = \frac{N_l - N_r}{N_l + N_r} = \frac{1 - N_r/N_l}{1 + N_r/N_l}. \tag{2.1}$$

Sometimes an extra factor 2 is included by convention to cancel the numerator $1 + N_l/N_r \approx 2$. In order to obtain a left-right asymmetry the target need not have polarized electrons. This is for example the case with Mott scattering where unpolarized high-Z, usually gold, targets are applied.

When the polarization of the beam is determined by scattering with target electrons the polarization of these target electrons becomes essential: reversal of their polarization direction will change the scattering cross section. The total countrate ($N = N_1 + N_2$) of the detectors is monitored for two different relative beam-target polarization directions. The two countrates, called $N = N_u$ and $N = N_d$, result in an 'up-down asymmetry' [2] defined as

$$\delta_{\rm ud} \;=\; \frac{N_u - N_d}{N_u + N_d}.$$

The type and number of detectors and their spatial arrangement can be varied to obtain the best possible scattering process recognition. The correct identification of these processes is important because misidentifications lead to a dilution of the observed asymmetry δ and require the introduction of a dilution factor f. The asymmetry δ, corrected for instrumental asymmetries δ_0, then becomes

$$\delta - \delta_0 = (1 - f)\vec{S} \cdot \vec{P_b}. \tag{2.2}$$

The vector $\vec{S}$, the polarization sensitivity, is in general a function of the target polarization and of the polarization dependent asymmetric part of the cross section of the process under consideration.

The uncertainty in the magnitude of the deduced beam polarization $P_b = |\vec{P_b}|$ is given by

$$\Delta P_b = \frac{1}{S_{\rm eff}}\sqrt{\frac{1}{2N} + (\Delta\delta_0)^2}, \tag{2.3}$$

[1] The detectors are often placed to the left and to the right of the plane determined by the beam and polarization direction which explains the name given to the asymmetry.

[2] Often the direction of the target polarization is changed while the beam polarization remains unchanged. The two directions of the target polarization are called 'up' and 'down' which explains the name.

where $N \approx N_{u/l} \approx N_{d/r}$. The effective polarization sensitivity is $S_{\text{eff}} = |\vec{S}|(1-f)\cos\alpha$, where α is the angle between $\vec{P}_b$ and $\vec{S}$. Equation 2.3 is deduced neglecting the uncertainties in $S = |\vec{S}|$, f and α. However, these uncertainties become important when experiments aim at absolute polarimetry. Quite often such experiments have to rely on theoretical estimates for f and α, without means of experimental verification. An exception is Mott polarimetry of β^--rays combined with double scattering of electrons as introduced by van Klinken [19]. However, in case of relative measurements one can take the ratio of P_β values resulting from alternating measurements with two β-sources. By taking the ratio the possibly insufficiently known values of $(1-f)$, $\vec{S}$ and to a large extend δ_0 in equation 2.3 cancel. Precision measurements in the past [20, 21, 22] rely on this relative measuring method. From equations 2.2 and 2.3 the requirements for an optimal polarimeter are:

- Minimized values for the *instrumental* asymmetry δ_0 and its error.
- Minimized dilution factor f and $\cos\alpha$ close to one.
- Optimized product $S_{\text{eff}}\sqrt{N}$. Often, events with an optimal value of S_{eff} have the lowest probability to occur.

Besides the above mentioned points, the efficiency $\epsilon = N/N_{\text{inc}}$, of the polarimeter is important. N_{inc} is the number of particles incident on the polarimeter. This together with the third item gives rise to a 'figure of merit' (FOM) defined as [5]

$$\text{FOM} = \epsilon S_{\text{eff}}^2 . \tag{2.4}$$

2.2 Polarization sensitive processes

Various polarization sensitive processes are reviewed in table 2.1 which is an updated version of a table given in a review by Frauenfelder and Steffen [23]. The processes are discussed in more detail in the following part of this chapter. The scattering asymmetry for Compton, Møller and Bhabha scattering as well as annihilation in flight is given in chapter 3.

Sometimes the polarization is transferred from an electron/positron to a photon or vice versa before one of the methods of the table is applied. Bremsstrahlung, Compton scattering and pair production can be used for this purpose. In these processes the incident energy is divided over two outgoing

quanta and they can both become polarized. However, the polarization is predominantly transferred to the highest energy secondary particle in the process.

The passage of polarized electrons and positrons through matter is associated with some degree of depolarization. At higher energies (>10 MeV) the depolarization is small and the polarization is more or less preserved in the 'high energy members' of the electromagnetic shower [24].

Table 2.1: *Overview of polarization sensitive electromagnetic processes as discussed in the text. References apply to representative experiments. References to the theory are in the text and chapter 3.*

Method	For	E	Remarks
Mott [6, 25, 26, 27]	e^-	10^{-5}-10 MeV	The scattering asymmetry is based on spin-orbit coupling. Sensitive to transverse polarization. Corrections for multiple scattering are necessary in target foils of finite thickness.
Positronium formation [28, 29, 30, 31, 32]	e^+	<100 eV	The timespectrum of the decay of positronium in a strong and reversible magnetic $\vec{B}$-field yields information on $\vec{P} \cdot \vec{B}$. Sensitive to all polarization directions. Corrections for depolarization during the slowing-down process of the positron are necessary.
Compton scattering [2, 33, 34]	γ	0.1-100 MeV	Sensitive to both circular and linear polarization. In case of linear polarization a polarized target is not needed. For circular polarization measurements such a target is mandatory; the asymmetry is observed upon reversal of the target polarization.
Møller scattering [8, 35, 36]	e^-	>1 MeV	A polarized target is necessary. Sensitive to both longitudinal and transverse polarization. The sensitivity for longitudinal polarization is larger than for transverse polarization. Asymmetry results from the spin-spin interaction between the scattering particles and the polarized target electrons.

continued on next page

continued from previous page

Method	For	E	Remarks
Bhabha scattering [35, 36, 37]	e^+	>1 MeV	See Møller scattering. At energies below < 5 MeV Bhabha scattering is less sensitive than Møller scattering.
Annihilation in flight [37]	e^+	>1 MeV	A polarized target is necessary. Approximately equally sensitive to longitudinal and transverse polarization. Asymmetry results from the spin-spin interaction between the positrons and polarized target electrons.
Compton backscattering [9]	$e^\pm$	>100 MeV	Analogous to Compton scattering except that the polarization of the photons (from a laser) is known and the polarization of the electrons/positrons is to be determined. The method is used in high energy physics.
Pair production [38, 39]	γ	>10 MeV	Sensitive to linear polarization. Measuring the azimuthal distribution of the plane in which the pairs are created. Sensitive to circular polarization if the positron and electron can be identified [40]. No experimental demonstration of the latter was found in the literature.
Triplet photoproduction [41, 42]	γ	>100 MeV	Sensitive to linear polarization. Based on an asymmetry in the azimuthal angular distribution of recoil electrons after pair production in the field of these electrons.

2.3 Electron and positron polarimetry at low energies

2.3.1 Mott polarimeters

Mott scattering is a well proven and matured method to determine the transverse polarization of low energy (<1 MeV) electrons. The method is based on the interaction between the spin of the electron and the Coulomb field of the scattering nucleus and it is the earliest technique for electron polarimetry. However, without spin-rotation the Mott scattering is exclusively sensitive to transverse polarization. To measure longitudinal electron polarization with a Mott polarimeter requires a spin rotation to transform the initial longitudinal polarization into an observable transverse polarization. This spin rotation can be achieved for example by placing in front of the Mott polarimeter an electrostatic deflector or a Wien-filter. A more detailed explanation of the

spin-orbit-interaction can be found in a recent review paper by Gay and Dunning [26] and in the book on polarized electrons by Kessler [5]. The figure of merit (equation 2.4) for a Mott polarimeter can be as high as 10^{-4}.

Sromicki et al. [6] investigated the possibility of using a Mott polarimeter at higher energies; up to 14 MeV. They concluded that the necessary corrections for multiple scattering in the polarimeter foil (see also [25] on corrections for multiple scattering) can be calculated accurately enough to use the method at these energies. Because Mott polarimetry is not incorporated in the polarimeter discussed in this thesis it is not further considered here. A review on electron polarimeters for atomic physics experiments where Mott polarimetry is essential was recently published by Gay [27].

Mott scattering is used for electron polarimetry, but can in principle also be used for positrons. However, in that case the sensitivity is considerably reduced because the Coulomb repulsion between the nucleus and the positrons leads to a reduced spin-orbit coupling.

2.3.2 Polarimeters based on positronium formation

When positrons are slowed down in a medium to atomic energies of less than 10 eV, they can form positronium before they annihilate. The positronium groundstate is a doublet of a singlet and a triplet state. In vacuum and in the absence of an external magnetic field, the singlet and triplet states decay into two and three photons, respectively. In the presence of a magnetic field B the $m = |1|$ triplet substates are unperturbed while the $m = 0$ triplet and the singlet state combine to a pseudotriplet and a pseudosinglet state. The pseudostates have both a two and three photon decay channel. When unpolarized positrons are stopped in an unpolarized medium the positronium is also unpolarized and the four magnetic substates ($m = \pm 1$ and the two pseudostates) are all equally populated. However, the pseudostates are not equally populated when the positron is polarized, as has been pointed out by Page and Heinberg [43]. The population ratio is $1 + \epsilon'$ and $1 - \epsilon'$ for the pseudotriplet and pseudosinglet state, respectively. The ϵ' parameter depends on B and on the positron polarization in an almost linear way. By observing the population ratio of the two pseudostates the polarization of the positron can be measured by reversing the magnetic field. The crucial point of the method is to separate the two pseudostates. The lifetimes of the states in the stopping medium are different and depend on the applied field as well as the composition of the medium. These facts can be used to separate the

states, as done in the pioneering days by Page and Heinberg [43] and by Dick and colleagues [44]. Later, the method was refined and the sensitivity was improved by a group around Rich at Ann Arbor/USA [28, 29, 30] and by Girard, Deutsch and colleagues at Louvain-la-Neuve/Belgium [31, 32]. The latter group used the instrument to search for possible right-handed currents in nuclear β-decay. MgO powder is used as a stopping medium and the decay curve of the positronium is measured for two opposite magnetic field directions. The method is well suited for relative measurements but not so well for absolute polarimetry because the slowing down of the positrons in the stopping medium is accompanied with depolarization. This depolarization is difficult to estimate with sufficient precision and remains the dominant systematic error when measuring absolute P-values. However, when performing comparative measurements with two β^+-sources this effect, as well as the polarization sensitivity of the whole apparatus, is approximately the same and cancels in the ratio of the polarization values for the two sources. The figure of merit (equation 2.4) is high and comparable with Mott scattering [29]: 10^{-4} to 10^{-5}.

The method based on positronium formation is thus a very sensitive one and takes as such a special position between the various polarimetry methods. However, its greatest potential lies in the lower energy regimes not important to the polarimeter discussed in this thesis.

2.4 Electromagnetic polarimetry at intermediate energies

2.4.1 Compton polarimeters

Compton scattering of photons by polarized electrons is sensitive to circular photon polarization. In the case of linear photon polarization the electrons of the scattering target can be unpolarized. The Klein-Nishina formula gives the differential cross section for the process (see chapter 3). A Compton cross section depending explicitly on the polarization states of all particles involved was derived by Lipps and Tolhoek [45, 46].

The detection of linear polarization with Compton scattering is a result of a term depending on the cosine squared of the angle between the polarization vector and the scattering plane in the cross section. The method has been used often in assigning multipolarities to nuclear gamma rays and in

determining spins and parities of nuclear states, as for example explained in a review by Fagg and Hanna [34].

The first experiment that was able to demonstrate the circular polarization of gamma rays by means of Compton scattering was done by Gunst and Page [47] in 1953. They used a 'transmission-type' polarimeter to observe the circular polarization of the 2.62 MeV gamma rays of one of the thorium isotopes. In this method the polarization is found by comparing the number of photons transmitted through a magnetized iron bar with the number transmitted through an identical bar which is not magnetized. Besides using Compton scattering in a transmission polarimeter, the process is used in a variety of forward- and backward-scattering devices using magnetized iron foils [33, 34].

More recently, Compton scattering is used at energies above 100 MeV to determine the polarization of electron beams in accelerators by means of Compton backscattering of circularly polarized laserlight. This will be discussed at the end of this chapter.

One of the few publications on Compton polarimetry in the energy regime between 10 MeV and 100 MeV found in the literature is by Garwin et al. [2]. They tried to observe a degree of circular polarization of 70 MeV photons emitted by decaying unpolarized π^0 *mesons. In their arrangement (figure 2.2) the photons were scattering off a magnetized iron target placed at 30 degrees with respect to the photon beam. The plastic scintillator counters #1, #2 and #3 served to discriminate between Compton scattering and pair production events. The trigger used was* $\overline{1}234\overline{3'}$ *where a bar means an anti-coincidence. Counts* $3'$ *represent events in detector #3 with a pulse height above a preset value. This level separates single minimum ionizing electrons (from Compton scattering) from two minimum ionizing electrons (from pair production). Detector #2 was included to exclude pairs produced in detector #3 itself. This setup is mentioned in some detail because its discrimination scheme and its double detector layer behind the iron foil are aspects that are also part of the polarimeter explored in this thesis. At 70 MeV pair production dominates over Compton scattering: without discrimination, fifteen times more pairs than Compton recoils are produced in the iron foil. This reduces the asymmetry from 1.167 (the asymmetry is based on 2 out of 26 polarized electrons in iron and defined as (1+(2/26))/(1-(2/26)); it is the asymmetry for a 100% polarized photon beam) to 1.010. By adjusting the discriminator level setting for* $3'$ *events the pair to Compton ratio improved to* ≈ 2*, restoring the asymmetry to 1.05. Approximately 80% of the Compton*

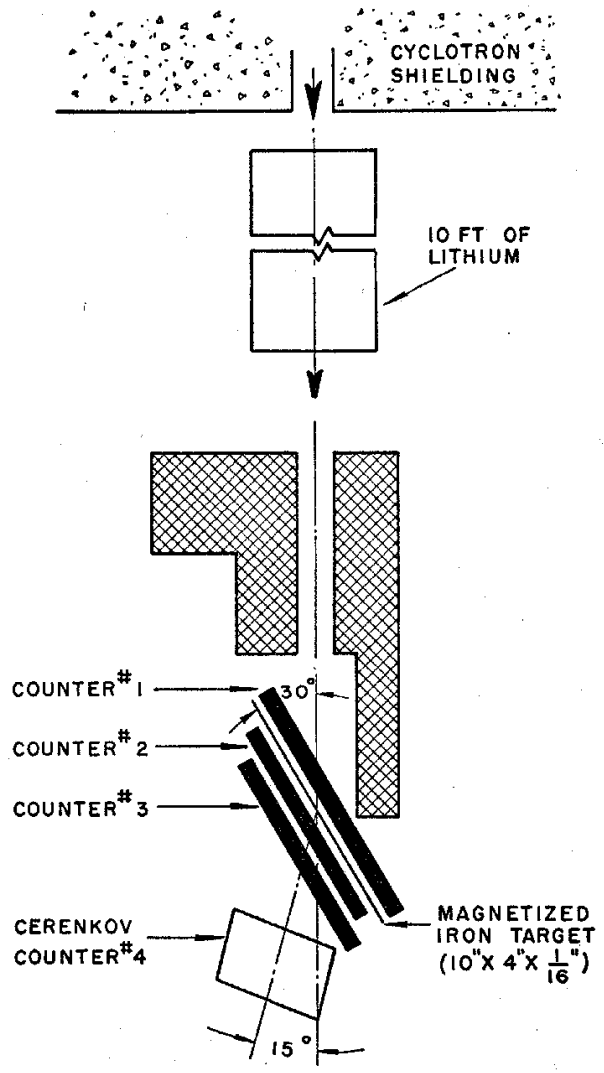

Figure 2.2: *Setup of the experiment by Garwin and colleagues. With 70 MeV photons from π^0-decays. The lithium is used to shield against neutrons from the cyclotron target used for π^0 production. The counters #1, #2 and #3 were $\frac{1}{4}$ inch plastic scintillators. The original figure appeared in reference [2].*

events in the iron target survived the trigger. The result of the experiment is of less relevance in the present context but was consistent with no circular polarization of the photon; $P = (2.0 \pm 9.0)\%$

2.4.2 Møller/Bhabha polarimeters

Møller and Bhabha scattering are sensitive to transverse and longitudinal polarization of electrons and positrons, respectively. However, in practice almost all Møller/Bhabha polarimeters aim at detection of the longitudinal polarization. This is because at relativistic energies ($E >> 2m_0c^2$) the asymmetry is as large as 7/9 for longitudinal spins, but remains low at 1/9 in case of transverse spin orientation. The appearance of a spin-spin dependent term in the cross section can intuitively be understood for electron-electron scattering in the low energy limit by considering the Pauli exclusion principle: When two electrons have their spins parallel they are not allowed to be at the same position at the same time, i.e. to scatter, while this is allowed when their spins are anti-parallel.

The theory of the scattering processes is well understood. Several authors (e.g. [48, 49]) calculated Møller and Bhabha cross-sections and their dependence on the particle polarization. Reviews were written by Frauenfelder and Rossi [50], by Frauenfelder and Steffen [23] and by Page [51].

Møller polarimetry was for the first time successfully applied in 1957 by Frauenfelder and co-workers [52]. Since then the polarimeters were steadily improved and made well suited for relative polarimetry. Absolute polarimetry remained difficult, because it has to rely on theoretical estimates for the polarization sensitivity. Although the asymmetry of the scattering process can be calculated accurately, it is not straightforward to obtain the effective polarization sensitivity in a polarimeter. After a time in which relatively little happened in this field, following the decade of the parity experiments, Møller and Bhabha polarimeters regained interest with the advent of high-energy electron accelerators and a developing interest in polarization phenomena at higher energies.

A modern Bhabha polarimeter is shown in the stereographic view of figure 2.3. The fourfould arrangement developed at the KVI [36] and used at energies from 1.3 to 2.2 MeV was used to investigate the possible existence of right-handed currents in nuclear β*-decay. The polarization of* β*-decay positrons from* ^{26m}Al*, a Fermi transition, was measured relative to those emitted by* ^{30}P*, a Gamow-Teller transition. By using the accurately known*

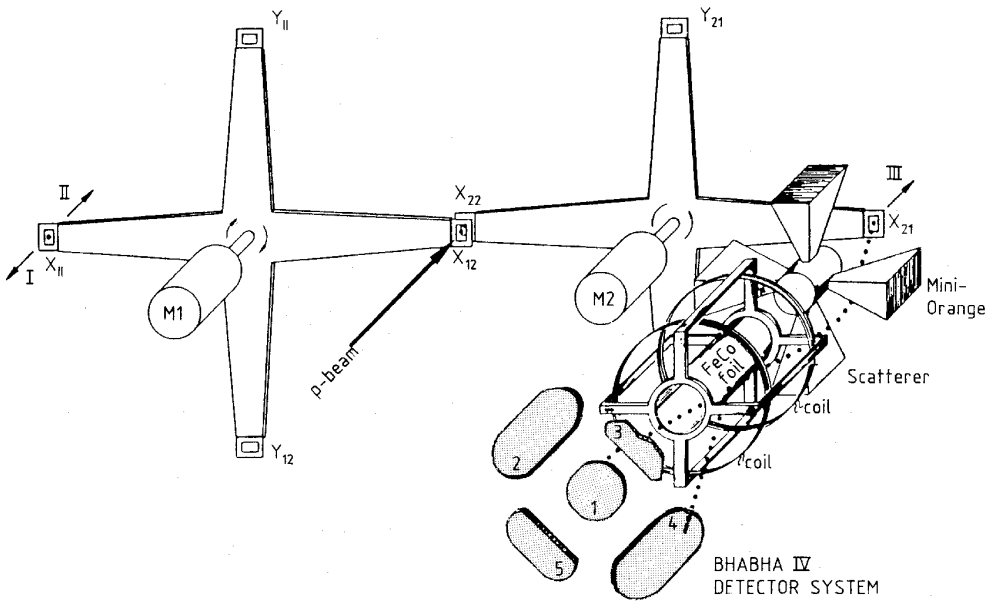

Figure 2.3: *Stereographical view of the Bhabha polarimeter used in the experiments by van Klinken and co-workers. The original figure appeared in reference [36].*

polarization value for Gamow-Teller transitions the measurement provided a lower limit on P_{Fermi} *of* $P_{\text{Fermi}} > 0.0984$ *(90% C.L.) [20, 35].*

The positron sources were produced periodically by a proton beam along the central axis of the arrangement. Two simultaneously produced short-lived sources are transported within less than a second to their measurement position in between two times two polarimeters; two at each side of the beam. In every polarimeter a Mini Orange (MO) system [53] is used to focus the positrons on the cylindrical shaped scattering foil of soft magnetic $Fe_{49}Co_{49}V_2$ *(FeCo). This cylindrical foil with was magnetized (target polarization 7.4%) by a pair of coils; the magnetization was reversed at a rate of 4 Hz. The Bhabha scattering events were detected by a set of 5 plastic detectors. The average sensitivity of the fourfold polarimeter was* $S \approx 4.3 \cdot 10^{-3}$ *(average asymmetry 0.058) which implies a FOM of maximal* 10^{-5}.

Note that in this arrangement every polarimeter is symmetric around the axis defined by the source and the polarimeter. This reduces possible sources

of instrumental asymmetry. By using four polarimeters the statistical power of the instrument is increased and the instrumental symmetry is even further improved. The Bhabha polarimeter can be turned into a Møller polarimeter by turning around the Mini Oranges and thus focussing electrons instead of positrons.

2.4.3 Polarimeters based on annihilation in flight

Annihilation in flight (AIF) of positrons by interaction with atomic electrons is a polarization sensitive process which depends on the relative orientation of the positron and electron spin. The AIF cross sections were first calculated by Page [54] and McMaster [55]. The method is used in a way similar to Møller and Bhabha scattering. However, AIF has one great advantage compared to these methods: the sensitivity to longitudinal and transverse polarization is comparable. In measurements of longitudinal polarized positrons AIF and Bhabha scattering can be used simultaneously with approximately equal analyzing power. The example hereafter illustrates this multiprocess aspect.

Corriveau et al. [37, 56] measured the longitudinal polarization of μ^+-decay positrons to verify the maximality of parity violation in muonic β-decay with significant improved accuracy as compared with older experiments [57, 58, 59, 60, 61] and a deviating[3] *result [62]. In their arrangement (figure 2.4) positive muons from π^+ decays are stopped in a low-Z target (1). The positrons from the decay have energies up to 52.8 MeV. They pass a timing counter (4) before entering the polarimeter with a scattering foil (8) of pure iron and a thickness of* 0.5 *mm. With an electron polarization in the target plane of 5.4% and a target angle of* 45° *relative to the average positron trajectory the effective longitudinal polarization amounts to 3.8%. Multiwire proportional chambers (5, 6 and 7) in combination with plastic ΔE detectors (17) were used to discriminate Bhabha pairs from annihilation photons. The asymmetry in the number of scattered particles under reversal of the target magnetization depends on the energy of the detected e^+ and e^- particles (in case of Bhabha scattering) or annihilation quanta (in case of AIF) (see section 3.7 and 3.8). The results for the longitudinal positron polarization $P_L = 0.951 \pm 0.075(\pm 0.068)$ (statistical error in parentheses) for annihilation in flight and $P_L = 1.099 \pm 0.091(\pm 0.084)$ for Bhabha scattering combine to $P_L = 1.01 \pm 0.064(\pm 0.053)$, a value fully consistent with the V-A*

[3] Remarkably, no explanation for the deviation was found in the literature.

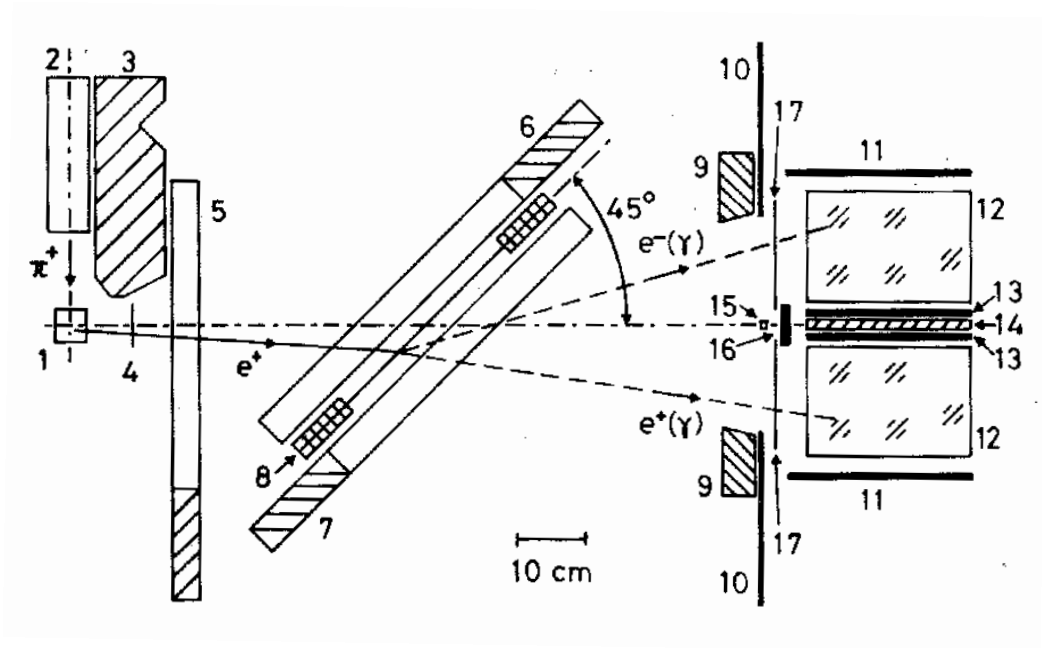

Figure 2.4: *AIF and Bhabha polarimeter used in the experiment of Corriveau and colleagues. The original figure appeared in reference [37].*

theory with implications as discussed by Burkard et al. [3].

Both the incorporation of more than one method in the polarimeter and the discrimination scheme to entangle Bhabha scattering and AIF are aspects which drew attention during the design of the polarimeter presented in chapter 1. At the PSI (Villigen/Switserland) a dedicated research program following this measurement encompasses transverse polarimetry of positrons from muonic decay [63, 64]. The broad field of basic experiments with muonic decay modes, on performance and in planning, can be found in a review by Fetscher and Gerber [65].

2.5 Polarimeters for high-energy physics

The quest for electron/positron and photon polarimetry at higher energies goes hand in hand with the increasing availability of polarized beams with energies far above 100 MeV. At these energies the polarimetry is mostly pur-

sued by Compton scattering of circular polarized laser photons with the beam particles or by Møller scattering with polarized target electrons. The physics underlying the methods is the same as for the low energy counterparts of the polarimeters. Which method is chosen and how the method is implemented depends among other things on the accelerator type and the beam structure and intensity.

A method to detect the polarization of high-energy photons, known as phototriplet production, is based on pair production in the field of a target electron [41, 42].

2.5.1 Compton polarimeters

Compton laser polarimeters have been developed for polarization detection at high-energy electron accelerators. While low-energy Compton polarimeters are used to measure the photon polarization, high-energy Compton polarimeters are used to determine the electron polarization. Instead of a polarized electron target with known polarization the polarimeters are based on the use of photons with a well defined circular polarization. The photons are produced by a laser equipped with a quarter wave plate to transform the initially linear polarization into a circular polarization. The energy of the photons is a around 2.5 eV (or 520 nm). A set of mirrors and lenses is used to transport the laser light, often over large distances, to the crossing point with the electron beam.

The polarization of the electrons is reflected in a change of either the countrate or the angular distribution of the scattered photons and electrons when the polarization of the photons is reversed. Either the scattered photons or the Compton backscattered electrons are observed. Examples of the two methods can be found at DESY [9] and at SLAC [66], observing photons and electrons, respectively.

2.5.2 Møller polarimeters and the Levchuk effect

Møller polarimeters are more easy to construct than Compton polarimeters. There are two basic versions: those with one and those with two detector arms, operated in, respectively, single and coincidence mode. The polarization of the first polarized high energy beam was measured by Cooper and colleagues at SLAC in 1975 [67] with a single-arm Møller polarimeter. An existing spectrometer was used to select the scattered electrons according

to their energy loss. Since then, dedicated single- or double-arm Møller polarimeters have been constructed at the synchrotron ELSA in Bonn [68], at the microtron MAMI in Mainz [7] and at the linear accelerator at MIT-Bates [8, 69].

Quite recently, Levchuk [70] suggested that absolute Møller polarimetry without the necessary precautions could lead to erroneous results. He considered the effects of the atomic motion of the target electrons on the Møller scattering process. The 'Levchuk effect' can be summarized as follows: The binding energy of the target electrons causes a spread in the angular distributions of the scattered electrons. This effect is largest when innershell K or L electrons are involved in the scattering. These electrons are unpolarized. The influence on the angular distribution when outershell polarized electrons are involved in the scattering is negligible. The overall result is a changing percentage of polarized electrons over the phasespace distribution. Some polarimeters are very sensitive to this effect due to their small phasespace acceptance. Recently, the effect was measured by Swartz and coworkers [66] by comparing polarization measurements from a Compton and a Møller polarimeter at SLAC. Feltham pointed out in a comment [71] that the atomic motion effect may modify the results obtained with the MIT-Bates polarimeter [69].

2.5.3 Photon polarimetry based on pair production

The azimuthal distribution of electrons and positrons produced in pair production by photons is asymmetric with respect to the direction of the linear photon polarization. Yang [72] and Berlin and Madansky [73] were the first to realize this. The theory and experimental possibilities are discussed by several authors [74, 75, 76]. The method was applied successfully by several groups [38, 39].

With increasing photon energy the opening angle of the produced pairs becomes smaller and smaller: $\theta \propto 1/E_\gamma$. This makes it difficult to apply the method at higher energies. However, Boldyshev and Peresun'ko [77] found an alternative to circumvent this difficulty. Pair production is not restricted to the field of nuclei. As is well known (see e.g. [78]), it occurs with a few percent probability in the field of the atomic electrons also. Instead of measuring the pair produced electron and positron the recoil electron can be detected. The recoils are emitted under a larger angle than the pair leptons and their energy is a few MeV which makes them easy to detect. The feasibility of the method

was demonstrated by a Japanese research group [41, 42].

Pair production is also sensitive to the circular polarization of photons. From the description of the theory by Olsen and Maximon [40] it becomes clear that the electron and positron have to be identified to be sensitive to the circular photon polarization. No publications in which the method is applied were found in the literature.

2.5.4 New developments

Two workshops on polarimeters preceding the SPIN96-conference [79] made clear that new polarimeter developments are triggered by achievements in high-energy physics. Besides the refinement and construction of 'classic' Møller and Compton polarimeters, new variations on existing apparatus are investigated. The interested reader should have a look at the conference book of abstracts [79].

Chapter 3

Polarization theory

In this chapter the theory for some of the processes introduced in chapter 2 is presented in detail. The following aspects are covered: First, the scattering *asymmetry coefficients* for Compton, Møller and Bhabha scattering and annihilation in flight. Second, the *polarization transfer* in Compton scattering as well as in bremsstrahlung and pair production. Third, the *depolarization* of a photon, electron or positron due to Compton, Møller and Bhabha scattering as well as bremsstrahlung.

By using Stokes parameters the theory is put into a form which makes it possible to follow the polarization development of an electromagnetic shower. The parameters are introduced using classical electromagnetism as an example. The results of this chapter are implemented in the GEANT code in chapter 4.

3.1 The Stokes parameters

The most general monochromatic homogeneous plane-wave for the electric field vector $\vec{E}$ satisfying Maxwell's equations in a source free, uniform and infinite medium is given by [80]

$$\vec{E}(\vec{x},t) = (a_1\vec{E}_1 + a_2\vec{E}_2)e^{i(\vec{k}\cdot\vec{x}-\omega t)}, \tag{3.1}$$

where $\vec{k}$ is the wave vector pointing in the direction of propagation. Its magnitude k is related to the speed v of the wave in the medium and to the frequency ω of the oscillation by $k = \omega/v$.

The real or complex unit vectors $\vec{E_1}$ and $\vec{E_2}$ are perpendicular to $\vec{k}$ (the wave is transverse as required by Maxwell's equations) and form the 'polarization basis'. For real vectors the basis is formed by two linear or plane polarization directions which are chosen to be orthogonal to each other for convenience (linear basis). For complex vectors the basis is elliptical. Usually the left and right circular polarization vectors are chosen in this case.

The polarization of the wave depends on the magnitude and relative phase of the complex coefficients a_1 and a_2 and the choice of basis. If, for example, a_1 and a_2 are in phase and the basis is linear then the polarization is linear. For a phase difference of 90°, the polarization is circular, and for all other cases the polarization is elliptical.

The four parameters introduced by Stokes in 1852 are quadratic in a_1 and a_2 and can be used to determine the polarization state of an electromagnetic wave by means of intensity measurements only [14, 80]. With the help of a linear polarizer and a quarter-wave plate (or an equivalent of these), the transverse and circular components of the electric field can be disentangled. By introducing an orthogonal right handed coordinate system in which the wave is travelling in the positive z-direction, the Stokes parameters can be defined as

I_0, the intensity of the wave.

P_1, the degree of linear polarization with respect to the x- and y-axis. If the intensities are I_x and I_y, $P_1 = (I_x - I_y)/I_0$.

P_2, the degree of linear polarization with respect to the axes oriented at 45° to the right of the previous x- and y-axis. The intensities are I_{45} and I_{135}, $P_2 = (I_{45} - I_{135})/I_0$.

P_3, the degree of circular polarization. If the intensities for left and right circular polarization are I_l and I_r, respectively, $P_3 = (I_l - I_r)/I_0$.

Expressed in terms of a_1 and a_2 and taking the linear basis $\{\vec{E_1},\vec{E_2}\}$ the Stokes parameters become

$$\begin{aligned} I_0 &= a_1^* a_1 + a_2^* a_2, \\ P_1 &= a_1^* a_1 - a_2^* a_2 / I_0, \\ P_2 &= a_1^* a_2 + a_2^* a_1 / I_0, \\ P_3 &= -i(a_1^* a_2 - a_2^* a_1)/I_0. \end{aligned} \tag{3.2}$$

In a compact way this is written as the Stokes vector $(I, \vec{P})$. The Stokes parameters are real and satisfy the relation: $P_1^2 + P_2^2 + P_3^2 = 1$. It should be kept in mind that their actual value depends on the chosen polarization basis. Originally, they were introduced in a classical background. The next step will be the introduction of the Stokes operators for the electromagnetic field.

3.2 Polarization of photons

The Maxwell equations can be written using a four vector $A^\mu = (\phi, \vec{A})$, where ϕ is a scalar potential and $\vec{A}$ a vector potential defined up to a gauge transformation [81, 82]. Since the electromagnetic field has only two independent components, two of the four components of A^μ are superfluous in describing the field. The two redundant components can be eliminated by making use of the gauge freedom. In the so called radiation or Coulomb gauge this is done by choosing $\phi = 0$ and $\mathrm{div}\vec{A} = 0$.

The quantization of the field in this gauge is straightforward [82] and leads to a vector field in terms of creation, $a^{(\lambda)\dagger}(k)$, and annihilation, $a^{(\lambda)}(k)$, operators

$$\vec{A}(x) = \int \frac{d^3k}{(2\pi)^3 2k_0} \sum_{\lambda=1}^{2} \vec{A}^{(\lambda)}(k)[a^{(\lambda)}(k)e^{-ikx} + a^{(\lambda)\dagger}(k)e^{ikx}], \tag{3.3}$$

where k is the four momentum satisfying $k^2 = 0$ or $k_0 = |\vec{k}|$. The gauge condition $\mathrm{div}\vec{A} = 0$ leads to $\vec{k} \cdot \vec{A}^{(\lambda)}(k) = 0$. The two polarization vectors $\vec{A}^{(\lambda)}(k)$ are perpendicular to $\vec{k}$ and will be chosen to be orthogonal to each other for convenience.

A precise understanding of equation 3.3 is not necessary in the present context. However, from the equation it can be seen that for a certain momentum k two independent orthogonal photon states can be created from the vacuum $|0\rangle$. An arbitrary photon state with momentum k is a linear combination of these two independent states. The polarized states $\phi_1 = a^{(1)\dagger}(k)|0\rangle$ and $\phi_2 = a^{(2)\dagger}(k)|0\rangle$ form a so called complete set in terms of which a general state can always be written as

$$\phi = a_1\phi_1 + a_2\phi_2, \tag{3.4}$$

where $|a_1|^2$ and $|a_2|^2$ are the relative probabilities of finding the photon in either one of the basis states (the states ϕ_1 and ϕ_2 are added coherently). A

single photon is always in a pure polarization state. Its Stokes parameters are given by 3.2.

The vector $\vec{P}$ can be considered as the polarization vector for the state. By choosing a coordinate system in the laboratory, the x, y and z components of $\vec{P}$ do not have a physical interpretation yet. Because the photon is massless its helicity is always ± 1 [83]. As a consequence the vector field $\vec{A}$ must always be perpendicular to the direction of motion of the photon. The physical interpretation of $\vec{P}$ follows in section 3.4.

3.3 Polarization of electrons

The quantum mechanical wave function for an electron can be found by solving the Dirac equation [5, 81]. The solutions are four-component wave functions; two independent solutions for an electron and two for a positron. If the solutions for the electron are ϕ_1 and ϕ_2 the general wave function ϕ for an electron can again be written as 3.4. In the rest frame of the electron the four-component solutions of the Dirac equation reduce to the two-component spinors. In this frame the polarization of an electron is defined as the expectation value of the Pauli spin operators

$$\sigma_x = \begin{pmatrix} 0 & 1 \\ 1 & 0 \end{pmatrix}, \sigma_y = \begin{pmatrix} 0 & -i \\ i & 0 \end{pmatrix}, \sigma_z = \begin{pmatrix} 1 & 0 \\ 0 & -1 \end{pmatrix}. \tag{3.5}$$

Thus the polarization vector $\vec{S}$ in the rest frame of the electron is given by

$$\begin{aligned} S_x = \langle\phi|\sigma_x|\phi\rangle &= (a_1^* \, a_2^*) \begin{pmatrix} 0 & 1 \\ 1 & 0 \end{pmatrix} \begin{pmatrix} a_1 \\ a_2 \end{pmatrix} = a_1^* a_2 + a_2^* a_1, \\ S_y = \langle\phi|\sigma_y|\phi\rangle &= (a_1^* \, a_2^*) \begin{pmatrix} 0 & -i \\ i & 0 \end{pmatrix} \begin{pmatrix} a_1 \\ a_2 \end{pmatrix} = -i(a_1^* a_2 - a_2^* a_1), \\ S_z = \langle\phi|\sigma_z|\phi\rangle &= (a_1^* \, a_2^*) \begin{pmatrix} 1 & 0 \\ 0 & -1 \end{pmatrix} \begin{pmatrix} a_1 \\ a_2 \end{pmatrix} = a_1^* a_1 - a_2^* a_2. \end{aligned} \tag{3.6}$$

Comparing this with the definition of the Stokes parameters it follows that $P_1 = S_z$, $P_2 = S_x$ and $P_3 = S_y$. If I is taken as

$$I = \langle\phi|I|\phi\rangle = (a_1^* \, a_2^*) \begin{pmatrix} 1 & 0 \\ 0 & 1 \end{pmatrix} \begin{pmatrix} a_1 \\ a_2 \end{pmatrix} = a_1^* a_1 + a_2^* a_2, \tag{3.7}$$

the Stokes parameters can be used to describe the polarization of an electron just as they are used to describe the polarization of a photon. However, for the electron the meaning of the x, y and z components of $\vec{P}$ is fixed by the choice of a basis in the laboratory frame because the polarization direction of an electron does not necessarily have a connection with the direction of motion of the electron.

3.4 Mixed states

Until now only pure states were considered, i.e. states for which there exists a definite direction in which the polarization is unity. To describe a partially polarized beam of electrons or photons the density matrix formalism is used (see for example [84]). In this formalism a beam of electrons or photons is represented by a 2×2 Hermitian matrix ρ with positive or zero eigenvalue and trace 1 (the state is normalized). For the pure state 3.4 the matrix is

$$\rho = \begin{pmatrix} a_1^* a_1 & a_2^* a_1 \\ a_1^* a_2 & a_2^* a_2 \end{pmatrix}, \tag{3.8}$$

which can be brought into the form

$$\rho = \begin{pmatrix} 1 & 0 \\ 0 & 0 \end{pmatrix}, \tag{3.9}$$

by a unitary transformation. A mixed state is obtained by an incoherent superposition of pure states. In this case ρ can be diagonalized but in general both diagonal matrix elements are nonzero. The resulting density matrix is an incoherent superposition of an unpolarized and a polarized state

$$\rho = \begin{pmatrix} \rho_a & 0 \\ 0 & \rho_b \end{pmatrix} = (1-p) \begin{pmatrix} 1/2 & 0 \\ 0 & 1/2 \end{pmatrix} + p \begin{pmatrix} 1 & 0 \\ 0 & 0 \end{pmatrix}, \tag{3.10}$$

where $p = \rho_a - \rho_b$ is the degree of polarization. This is to be compared with a pure state which is a coherent superposition of ϕ_1 and ϕ_2.

Another way of writing 3.8 [84] shows the connection with the polarization vector $\vec{S}$

$$\rho = \frac{1}{2}(I + \vec{S} \cdot \vec{\sigma}), \tag{3.11}$$

where I is given by 3.7, $\vec{S}$ by 3.6 and $\vec{\sigma}$ by 3.5. For a pure state $|\vec{S}| = 1$, while for a mixed state $|\vec{S}| = p < 1$, where p is the degree of polarization used in 3.10.

Likewise a beam can be described by a density matrix ρ, a polarization sensitive detector can be characterized by a density matrix ρ_{det}. The probability for the detector responding when placed in a beam is given by

$$W = \text{Tr}(\rho\rho_{\text{det}}), \tag{3.12}$$

or, using the Stokes vectors

$$W = \frac{1}{2}(1, \vec{S}_{\text{det}}) \begin{pmatrix} I \\ \vec{S} \end{pmatrix} = \frac{1}{2}(1, \vec{P}_{\text{det}}) \begin{pmatrix} I \\ \vec{P} \end{pmatrix}. \tag{3.13}$$

As mentioned, the values of the Stokes parameters depend on the polarization basis one has chosen. A change of basis is accompanied by a transformation of the parameters. If both the initial and final basis are orthogonal the transformation of the Stokes parameters is described by a rotation matrix M. For example, a rotation over an angle θ about the P_3-axis is given by (see the appendix of [15])

$$M = \begin{pmatrix} 1 & 0 & 0 & 0 \\ 0 & \cos\omega & \sin\omega & 0 \\ 0 & -\sin\omega & \cos\omega & 0 \\ 0 & 0 & 0 & 1 \end{pmatrix}, \tag{3.14}$$

where $\omega = \theta$ for electrons and $\omega = 2\theta$ for photons. For electrons the z-axis will be chosen as the direction of propagation. A rotation θ around this P_1 axis is given by

$$M = \begin{pmatrix} 1 & 0 & 0 & 0 \\ 0 & 1 & 0 & 0 \\ 0 & 0 & \cos\theta & \sin\theta \\ 0 & 0 & -\sin\theta & \cos\theta \end{pmatrix}. \tag{3.15}$$

Using the Stokes parameters, the effect of an electromagnetic interaction can be written as a 4×4 matrix, T, working on the Stokes vector 3.2. The resulting 4-vector gives the Stokes parameters of the final state:

$$\begin{pmatrix} I' \\ \vec{P}' \end{pmatrix} = T \begin{pmatrix} I \\ \vec{P} \end{pmatrix}. \tag{3.16}$$

Table 3.1: *Interpretation of components of the Stokes vector if the polarization basis for the photon is chosen as explained in the text.*

Stokes parameter	Photon	Electron
I	Intensity	Intensity
P_1	Plane polarization in the direction of $\vec{A}_1$ $(+1)$ and $\vec{A}_2$ (-1)	Spin in the z-direction (S_3)
P_2	Plane polarization in the basis 45° to the right of $\vec{A}_1$	Spin in the x-direction (S_1)
P_3	Left $(+1)$ and right (-1) circular polarization	Spin in the y-direction (S_2)

The probability of finding the beam in a state $(1, \vec{D})$ after the interaction is given by 3.13

$$W = \frac{1}{2}(1\,\vec{D})T\begin{pmatrix} I \\ \vec{P} \end{pmatrix}. \tag{3.17}$$

In the following sections reduced matrices will be presented. This means that the cross section for an unpolarized beam detected by a detector that is not sensitive to polarization is normalized to unity i.e., the upper left matrix element of T is equal to one.

An interaction makes it possible to define the physical meaning of the Stokes parameters for the photon. The components $\vec{A}_1$ and $\vec{A}_2$ of the vector field $\vec{A}$ are chosen perpendicular to and in the reaction plane, respectively. They form, together with the unit vector $\vec{n}$ in the direction of motion of the photon, a right handed coordinate system $(\vec{A}_1/|\vec{A}_1|, \vec{A}_2/|\vec{A}_2|, \vec{n})$. The directions of $\vec{A}_1$ and $\vec{A}_2$ are as required by the Maxwell equations. Relative to this basis the Stokes parameters for the photon can be interpretated as given in table 3.1. In the laboratory frame this basis will have a different orientation for every interaction. If the photon direction of motion is changed due to the interaction the basis for the outgoing and incoming photon will also have a different orientation as seen from the laboratory frame.

Summarizing: the parameters first introduced by Stokes describe the polarization of a beam of electrons and photons in a unified way and make it possible to incorporate interactions by means of matrices.

3.5 Compton scattering

3.5.1 Scattering asymmetry

The cross section for Compton scattering of a polarized photon (Stokes vector $\vec{P}$) by a polarized electron (polarization vector $\vec{S}$) is proportional to [1, 45, 46]

$$\begin{aligned}\frac{d\sigma}{d\Omega} &\propto (1+\cos^2\theta)+(k_0-k)(1-\cos\theta) \\ &\quad +P_1\sin^2\theta - P_3(1-\cos\theta)\vec{S}\cdot(\vec{k}_0\cos\theta+\vec{k}),\end{aligned} \tag{3.18}$$

where $\vec{k}_0 = k_0\vec{n}_0$ and $\vec{k} = k\vec{n}$ are the momentum vectors of the incoming and outgoing photon of momentum k_0 and k (in units of mc) in the directions given by the unit vectors $\vec{n}_0$ and $\vec{n}$, respectively, and where θ is the scattering angle between the incoming and outgoing photon in the laboratory system. The relation between k_0, k and θ is $k = k_0/(1+k_0(1-\cos\theta))$. The polarization insensitive part of 3.18 is the Klein-Nishina cross section.

The Compton scattering asymmetry ratio between photons that are linearly polarized in the direction $\vec{A}_1$ ($P_1 = 1$) to those polarized in the direction $\vec{A}_2$ ($P_1 = -1$) is

$$R_{\text{lin}} = \frac{{k_0}^2 + k^2}{{k_0}^2 + k^2 - 2k_0k\sin^2\theta}. \tag{3.19}$$

Figure 3.1a shows R_{lin} as a function of the scattering angle of the photon for various energies. The degree of linear polarization of the photons is measured by changing the position of the photon detector in such a way that the reaction plane turns over an angle of 90°.

The asymmetry ratio for left-circular ($P_3 = 1$) to right-circular ($P_3 = -1$) polarized photons scattered from electrons polarized in the direction of the momentum of the incoming photons ($S_3 = 1$), is given by

$$R_{\text{lr}} = \frac{(1+\cos^2\theta)+(1-\cos\theta)[(k_0-k)-(k_0+k)\cos\theta]}{(1+\cos^2\theta)+(1-\cos\theta)[(k_0-k)+(k_0+k)\cos\theta]}. \tag{3.20}$$

Figure 3.1b shows this ratio as a function of the scattering angle of the photon. The ratio of the cross section for left circular ($P_3 = 1$) polarized photons to the cross section for unpolarized ($P_3 = 0$) photons scattered off electrons polarized in the direction of the momentum ($S_3 = 1$) of the incoming photons is shown in 3.1c. In a polarimeter the circular polarization of the photons is measured by reversing the magnetization of the (iron) target ($\vec{S}$ in 3.18; see chapter 2).

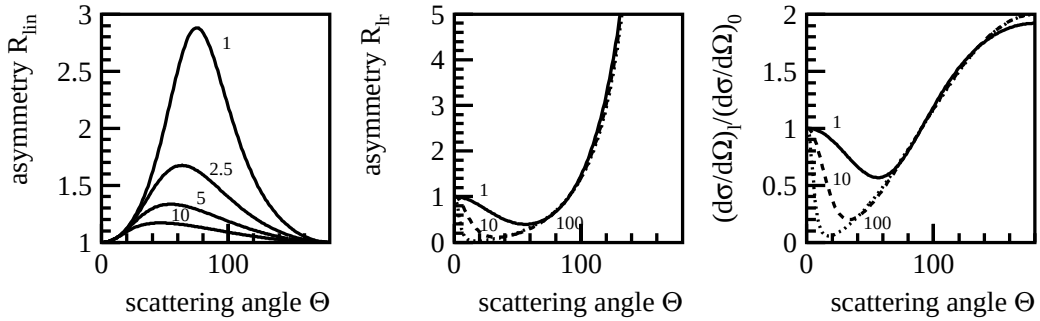

Figure 3.1: *a) Ratio of the intensities of Compton-scattered photons polarized perpendicular to the scattering plane and those polarized in the scattering plane. b) Ratio of left and right circular polarized photons Compton scattered from electrons polarized in the direction of the momentum of the incoming photons. c) Ratio of left polarized and unpolarized photons Compton scattered from electrons polarized in the direction of the momentum of the incoming photons. The curves are labeled by the photon energy in MeV.*

3.5.2 Depolarization

The reduced interaction matrix describing the polarization state of the photons after Compton scattering with unpolarized electrons is given by [15, 46, 85]

$$T_{\mathrm{CS}\gamma} = \begin{pmatrix} 1 & A & 0 & 0 \\ A & B & 0 & 0 \\ 0 & 0 & C & 0 \\ 0 & 0 & 0 & D \end{pmatrix}, \tag{3.21}$$

where

$$\begin{aligned} A &= \sin^2\theta/I, \\ B &= (1+\cos^2\theta)/I, \\ C &= 2\cos\theta/I, \\ D &= (2\cos\theta + (k_0-k)(1-\cos\theta)\cos\theta)/I, \\ I &= (1+\cos^2\theta) + (k_0-k)(1-\cos\theta). \end{aligned}$$

This matrix describes the depolarization of photons due to Compton scattering with unpolarized electrons. The polarization of the photon before and

after the scattering is given relative to reference frames as defined at the end of section 3.4. The matrix for Compton scattering with polarized electrons can be found in the literature [15, 46, 85]. It will not be used in this thesis.

3.5.3 Polarization transfer

The matrix describing the polarization transfer to the scattered electron can be deduced from [46] as[1]

$$T_{\mathrm{CSe}} = \begin{pmatrix} 1 & 0 & 0 & 0 \\ 0 & 0 & 0 & E \\ 0 & 0 & 0 & 0 \\ 0 & 0 & 0 & F \end{pmatrix}, \tag{3.22}$$

where

$$\begin{aligned} E &= ((\cos\theta - 1)((k_0 + k)\cos\theta + G(k\cos\theta - k_0)))/I, \\ F &= ((\cos\theta - 1)(1 + G)k\sin\theta)/I, \\ G &= (1 + \cos\theta)(k_0 + k)/(k_0 - k + 2). \end{aligned}$$

The matrix gives the polarization of the electron in the reference frame of the outgoing photon. The electron polarization is rotated from this reference frame to its own reference frame with the matrices 3.14 and 3.15.

A discussion on the use of Compton scattering to create beams of polarized electrons is presented by Tolhoek and Lipps [1, 45, 46].

3.6 Møller scattering

3.6.1 Scattering asymmetry

The cross section for polarized electrons scattered by polarized (target) electrons is

$$\frac{d\sigma}{d\Omega} = \frac{d\sigma_0}{d\Omega}(1 + \sum_{i,j=x,y,z} m_{ij} S_B^i S_T^j), \tag{3.23}$$

[1]This result is in agreement with the formulas found in the extensions made to the EGS4-code by Flöttmann [16].

where S_B^i (S_T^j) are the components of the beam (target) polarization vector in the rest frame of the electrons. $d\sigma_o/d\Omega$ is the cross section for unpolarized electron electron scattering and m_{ij} are the asymmetry coefficients. The following relations hold for an electron moving along the z-axis and the xz-plane being the scattering plane [48, 49, 86]

$$\begin{aligned}
\frac{d\sigma_0}{d\Omega} &= \frac{r_0^2}{4\gamma^2}\frac{m_0}{(\gamma^2-1)^2\sin^4\theta}, \\
m_0 &= \sin^2\theta(\gamma^2-1)^2(4+\sin^2\theta)+(2\gamma^2-1)^2(4-3\sin^2\theta), \\
m_{xx} &= -\sin^2\theta[\sin^2\theta(\gamma^4-1)+(2\gamma^2-1)]/m_0, \\
m_{yy} &= \sin^2\theta[\sin^2\theta(\gamma^2-1)^2-(4\gamma^2-3)]/m_0, \\
m_{zz} &= \sin^2\theta[\sin^2\theta(\gamma^4-1)-(2\gamma^2-1)(4\gamma^2-3)]/m_0, \\
m_{xz} &= m_{zx} = -\sin^2\theta\gamma(\gamma^2-1)\sin 2\theta/m_0, \\
m_{xy} &= m_{yx} = m_{yz} = m_{zy} = 0.
\end{aligned} \tag{3.24}$$

In these formulas θ and γ are the scattering angle and the total energy in units of mc^2 of the electron, respectively, both in the center-of-mass frame. In a fixed laboratory frame the scattering intensities are dependent on the polar angle ϕ around the beam axis. This angle does not show up in the formulas because the coefficients are defined relative to the scattering plane.

Figure 3.2 shows the asymmetry coefficients as a function of the laboratory energy and scattering angle. Numerical values for the asymmetry coefficients m_{ij} were given by Holzwarth [86].

3.6.2 Depolarization

To calculate the depolarization of an electron beam due to Møller scattering the Stokes interaction matrix will be used again. The incoming electron is moving along the z-axis, the xz-plane is the plane of scattering and the target

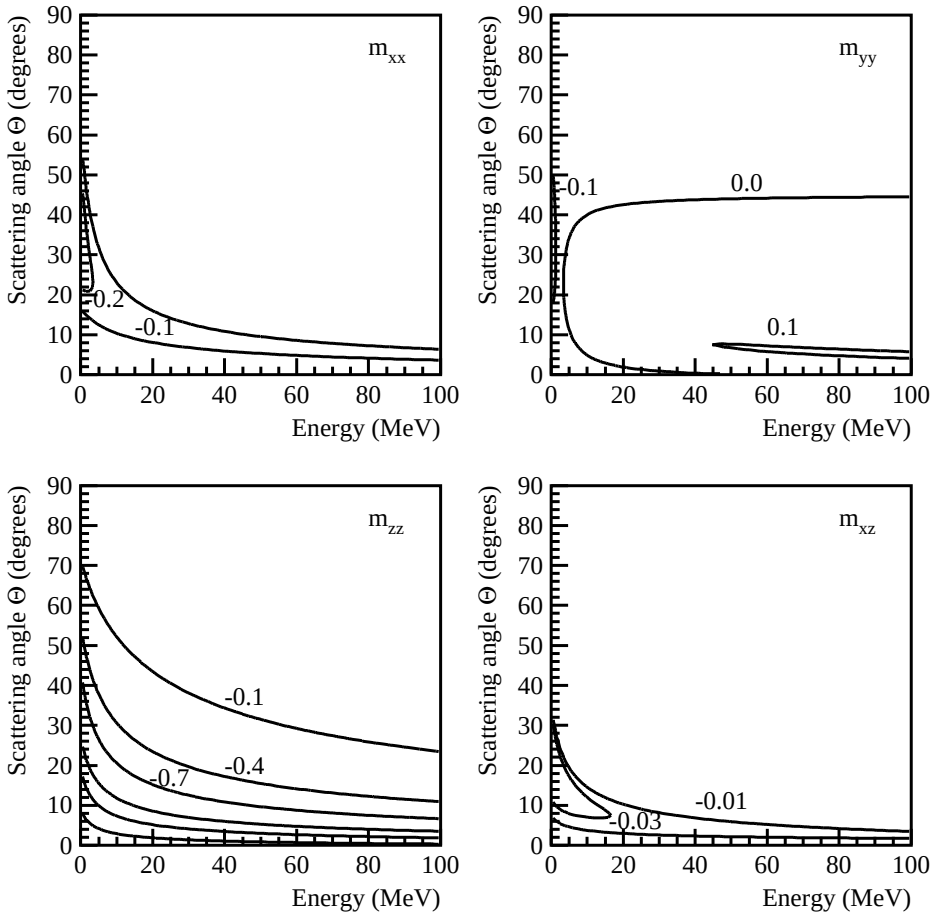

Figure 3.2: *Asymmetry coefficients for Møller scattering as a function of the laboratory kinetic energy and scattering angle of the electron. The curves represent various m_{ij}-values.*

electron is unpolarized. The reduced matrix is given by[2]

$$T_M = \begin{pmatrix} 1 & 0 & 0 & 0 \\ 0 & C & D & 0 \\ 0 & D & E & 0 \\ 0 & 0 & 0 & F \end{pmatrix}, \tag{3.25}$$

[2]McMaster [15] has given this matrix but with some errors. According to his matrix it is possible to obtain polarized electrons after Møller scattering from unpolarized electrons which is not possible. The matrix given here is calculated from matrix elements presented by Stehle [87]. Stehle deduced matrix elements for all combinations of possible incoming and outgoing polarization states.

where

$$\begin{aligned}
C &= 2\cos\theta(2\gamma^2-1)(2\gamma^2-1-\gamma^2\sin^2\theta)/I, \\
D &= 2\gamma(2\gamma^2-1)\sin\theta\cos^2\theta/I, \\
E &= 2\cos\theta(2\gamma^2-1)(2\gamma^2-1-\sin^2\theta)/I, \\
F &= 2[(2\gamma^2-1)^2-(2\gamma^4-1)\sin^2\theta]/I, \\
I &= \frac{1}{2}[(2\gamma^2-1)^2(4-3\sin^2\theta)+(\gamma^2-1)^2(\sin^4\theta+4\sin^2\theta)],
\end{aligned}$$

and where γ and θ are the electron energy in units of mc^2 and the scattering angle of the electron, respectively, both in the center-of-mass frame. The corresponding laboratory values γ' and θ' are:

$$\begin{aligned}
\gamma' &= 2\gamma^2-1, \\
\cos\theta &= \frac{2-(\gamma'+3)\sin^2\theta'}{2+(\gamma'-1)\sin^2\theta'}.
\end{aligned} \tag{3.26}$$

The relation between the solid angle $d\Omega$ and its laboratory equivalent $d\Omega'$ is

$$d\Omega = \frac{8(\gamma'+1)\cos\theta'}{[2+(\gamma'-1)\sin^2\theta']^2}d\Omega'. \tag{3.27}$$

The factor $\frac{1}{2}$ in the expression for I is due to the fact that the scattering and scattered electron are indistinguishable in Møller scattering [88]. In this way the highest-energy member of the scattered particles is associated with the original incoming electron. The polarization of the lowest-energy electron, interpreted as the original target electron, is not calculated.

The resulting polarization is given in the rest frame of the electron with has its z-axis parallel to the direction of motion of the electron in the center-of-mass frame. Rotation matrices can be applied to obtain the polarization in the rest frame of the electron with has its z-axis parallel to the direction of motion in the laboratory frame.

3.7 Bhabha scattering

3.7.1 Scattering asymmetry

The cross section for electron-positron scattering can also be written in the form 3.23. Replacing m_0 and m_{ij} by b_0 and b_{ij} to avoid confusion the asym-

metry coefficients b_{ij} become [86]

$$
\begin{aligned}
\frac{d\sigma_0}{d\Omega} &= \frac{r_0^2}{16\gamma^6}\frac{b_0}{(\gamma^2-1)^2\sin^4(\theta/2)}, \\
b_0 &= 2\gamma^2+7\gamma^4-14\gamma^6+9\gamma^8+2\gamma^2(-4+\gamma^2+3\gamma^4)\cos\theta + \\
&\quad (1+4\gamma^2-5\gamma^4-6\gamma^6+6\gamma^8)\cos^2\theta+2(\gamma^2-1)^3\cos^3\theta + \\
&\quad (\gamma^2-1)^4\cos^4\theta, \\
b_{xx} &= (\gamma^2-1)(\cos\theta-1)[3\gamma^4+\gamma^6+(-4\gamma^2+\gamma^4+\gamma^6)\cos\theta + \\
&\quad (1+\gamma^2-\gamma^4-\gamma^6)\cos^2\theta+(-1+\gamma^2+\gamma^4-\gamma^6)\cos^3\theta]/b_0, \\
b_{yy} &= (\gamma^2-1)(\cos\theta-1)[2\gamma^2+5\gamma^4-\gamma^6+(-6\gamma^2+7\gamma^4-\gamma^6)\cos\theta + \\
&\quad (1-\gamma^2-\gamma^4+\gamma^6)\cos^2\theta+(-1+3\gamma^2-3\gamma^4+\gamma^6)\cos^3\theta]/b_0, \\
b_{zz} &= (\gamma^2-1)[3\gamma^4-7\gamma^6+(-4\gamma^2+6\gamma^4)\cos\theta + \\
&\quad (1+5\gamma^2-10\gamma^4+6\gamma^6)\cos^2\theta + \\
&\quad (-2+2\gamma^4)\cos^3\theta+(1-\gamma^2-\gamma^4+\gamma^6)\cos^4\theta]/b_0, \\
b_{xz} &= b_{zx} = 2\gamma(\gamma^2-1)\sin\theta(\cos\theta-1)[\gamma^2+(-1+\gamma^4)\cos\theta \\
&\quad +(1-2\gamma^2+\gamma^4)\cos^2\theta]/b_0, \\
b_{xy} &= b_{yx} = b_{yz} = b_{zy} = 0.
\end{aligned}
$$

where γ and θ are again center of mass variables. Numerical values for the asymmetry coefficients for laboratory energies and scattering angles are shown in figure 3.3.

3.7.2 Depolarization

The matrices for the depolarization due to Bhabha scattering are calculated using the matrix elements given by Stehle [87]. For an unpolarized target electron the reduced matrix for the outgoing positron is

$$
T_B = \begin{pmatrix} 1 & 0 & 0 & 0 \\ 0 & D & E & 0 \\ 0 & E & F & 0 \\ 0 & 0 & 0 & C \end{pmatrix}, \tag{3.28}
$$

where

$$
I = B2^2 + (B1^2 + B4^2 + B6^2 + B7^2)/4,
$$

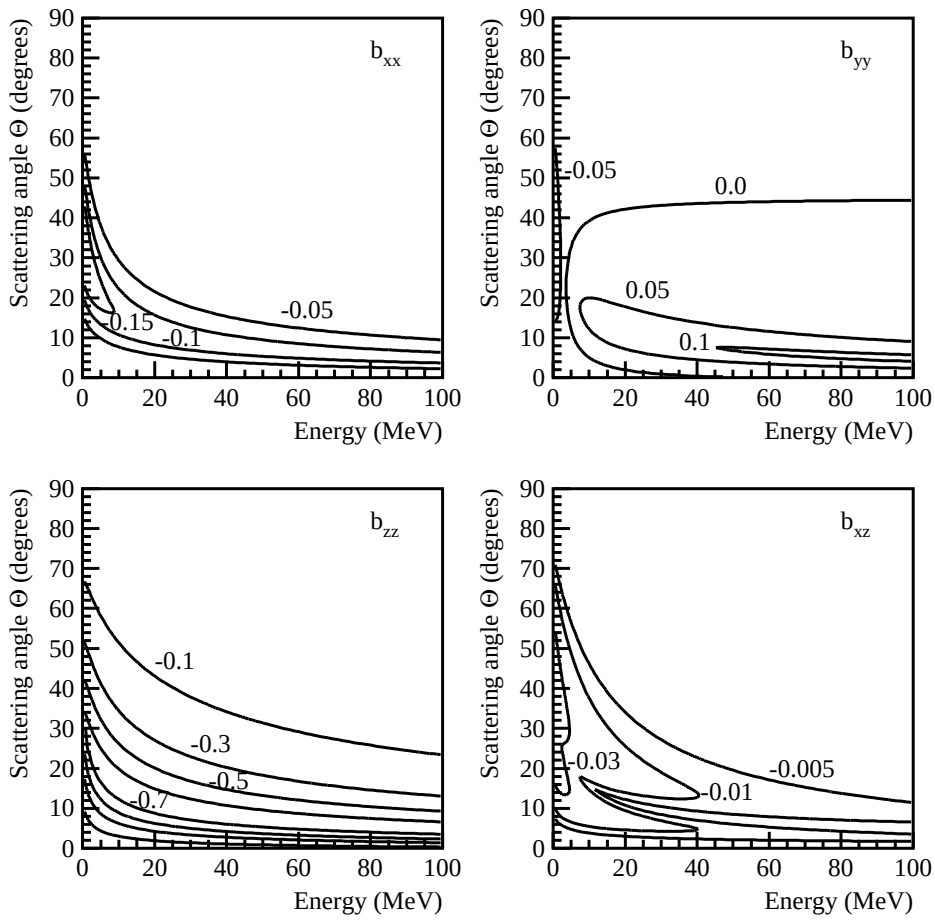

Figure 3.3: *Asymmetry coefficients for Bhabha scattering as a function of the laboratory kinetic energy and scattering angle of the positron.*

$$
\begin{aligned}
C &= [(B1B7 + B6B4)/2 + B2^2]/I, \\
D &= (B1^2 - B4^2 - B6^2 + B7^2)/4I, \\
E &= B2(B1 + B4 + B6 + B7)/2I, \\
F &= (B6B4 - B1B7)/2I,
\end{aligned}
$$

with [87]:

$$
\begin{aligned}
B1 &= -\cot^2(\theta/2)[1 + 2\beta^2\gamma^2\cos^2(\theta/2)], \\
B2 &= \gamma\cot(\theta/2)[1 - 2\beta^2\sin(\theta/2)],
\end{aligned}
$$

$$
\begin{aligned}
B4 &= [-1 + 2\beta^2\gamma^2 \sin^2(\theta/2)], \\
B6 &= -[1 + 2\beta^2\gamma^2 \cos^2(\theta/2)]/\gamma^2, \\
B7 &= -\beta^2(2\gamma^2 + 1) - \cot^2(\theta/2)[(2\gamma^2 - 1) + 2\beta^2 \sin^2(\theta/2)],
\end{aligned}
$$

and $\beta = (\gamma^2 - 1)/\gamma^2$. The variables γ and θ are given in the center-of-mass frame. A series of rotations has to be applied to obtain the polarization of the positron in the rest frame with the z-axis parallel to the direction of motion in the laboratory frame.

3.8 Annihilation in flight

3.8.1 Scattering asymmetry

The cross section for annihilation in flight can be written in the form 3.23 similar as has been done for Bhabha and Møller scattering. The asymmetry coefficients will be denoted by a_{ij}. Using the results of Page [54] leads to the following formulas

$$
\begin{aligned}
\frac{d\sigma_o}{d\Omega} &= \frac{r_0^2}{4\beta\gamma^2} \frac{a_0}{(1 - \beta^2 \cos^2\theta)^2}, \\
a_0 &= 1 - \beta^4 + 2\beta^2 \sin^2\theta - \beta^4 \sin^4\theta, \\
a_{xx} &= [-(1 - \beta^2)^2 + 2\beta^2 \sin^2\theta - \beta^4 \sin^4\theta]/a_0, \\
a_{yy} &= [-(1 - \beta^2)^2 - \beta^4 \sin^4\theta]/a_0, \\
a_{zz} &= [-(1 - \beta^4) + 2\beta^2 \sin^2\theta - \beta^2 \sin^4\theta(2 - \beta^2))/a_0, \\
a_{xz} &= a_{zx} = 0, \\
a_{xy} &= a_{yx} = a_{yz} = a_{zy} = 0.
\end{aligned}
\tag{3.29}
$$

In these equations $\beta^2 = (\gamma^2 - 1)/\gamma^2$. Both γ and the scattering angle θ of one of the photons are in the center-of-mass system. Numerical values are shown in figure 3.4 for kinetic energies and scattering angles in the laboratory. The fact that a_{xz} and a_{zx} are zero is due to a cancelation of terms depending on $P_B^x P_T^z$ and $P_B^z P_T^x$ when the polarization states of the outgoing particles are summed over. The asymmetry coefficients are the same as calculated by Corriveau [37].

The polarization transfer to the annihilation photons is left outside the scope of this thesis.

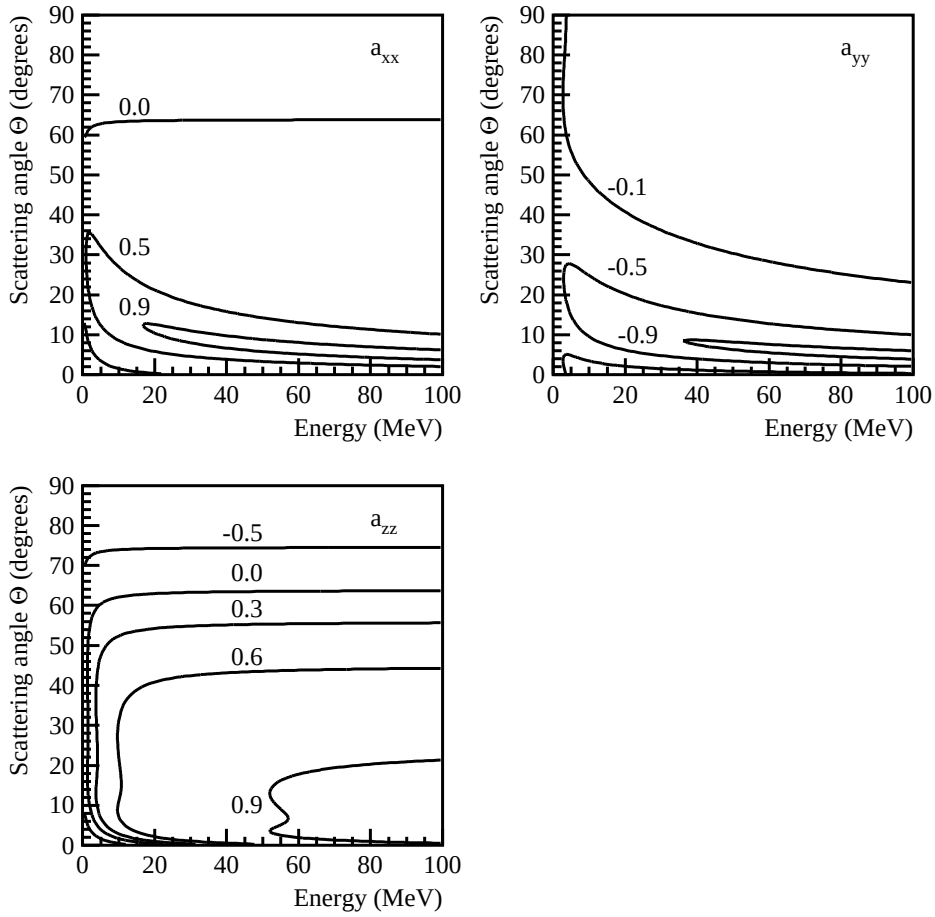

Figure 3.4: *Asymmetry coefficients for annihilation in flight as a function of the laboratory kinetic energy and scattering angle of the photon.*

3.9 Bremsstrahlung

The matrices 3.30, 3.31 and 3.33 presented in this section and the next one on pair production were previously calculated by Flöttmann [16]. The results given below are in agreement with his calculations.

3.9.1 Polarization transfer

The polarization transfer of an electron or positron to a photon due to bremsstrahlung was first calculated by Olsen and Maximon [89] taking into account Coulomb and screening effects. From their work the following transfer matrix can be deduced for the polarization vector of the photon

$$T_{\mathrm{brem},\gamma} = \begin{pmatrix} 1 & 0 & 0 & 0 \\ D & 0 & 0 & 0 \\ 0 & 0 & 0 & 0 \\ 0 & L & T & 0 \end{pmatrix}, \tag{3.30}$$

where

$$\begin{aligned}
I &= (\epsilon_1^2 + \epsilon_2^2)(3 + 2,) - 2\epsilon_1\epsilon_2(1 + 4u^2\xi^2,), \\
D &= 8\epsilon_1\epsilon_2 u^2\xi^2, /I, \\
T &= -4k\epsilon_2\xi(1 - 2\xi), u/I, \\
L &= k[(\epsilon_1 + \epsilon_2)(3 + 2,) - 2\epsilon_2(1 + 4u^2\xi^2,)]/I, \\
\epsilon_1 &= \text{total energy of the incoming electron/positron in units } mc^2, \\
\epsilon_2 &= \text{total energy of the outgoing electron/positron in units } mc^2, \\
\vec{p} &= \text{electron/positron initial momentum in units } mc, \\
\vec{k} &= \text{photon momentum in units } mc, \\
\vec{u} &= \text{component of } \vec{p} \text{ perpendicular to } \vec{k}, \\
u &= |\vec{u}|, \\
k &= \epsilon_1 - \epsilon_2 \text{ energy of the photon in units } mc^2, \\
\xi &= 1/(1 + u^2).
\end{aligned}$$

The polarization vector of the incoming electron/positron must be rotated into the frame defined by the scattering plane (xz-plane) and the direction of the outgoing photon (z-axis) with the rotation matrices 3.14 and 3.15 prior to applying 3.30. The resulting polarization vector of the bremsstrahlung photon is also given in this frame. , contains the Coulomb and screening effects

$$\begin{aligned}
, &= \ln(1/\delta) - 2 - f(Z) + \mathcal{F}(\delta/\xi), \\
\delta &= k/(2\epsilon_1\epsilon_2),
\end{aligned}$$

Table 3.2: *F for intermediate values of the screening factor* Δ *[92].*

Δ	$-\mathcal{F}(\delta/\xi)$	Δ	$-\mathcal{F}(\delta/\xi)$
0.5	0.0145	40.0	2.001
1.0	0.0490	45.0	2.114
2.0	0.1400	50.0	2.216
4.0	0.3312	60.0	2.393
8.0	0.6758	70.0	2.545
15.0	1.126	80.0	2.676
20.0	1.367	90.0	2.793
25.0	1.564	100.0	2.897
30.0	1.731	120.0	3.078
35.0	1.875		

where $f(Z)$ is the Coulomb correction term calculated by Davies, Bethe and Maximon [90]. An approximated version [91] which is accurate up to 4 digits for $a = \alpha Z$ up to 2/3 (Uranium) is

$$f(Z) = a^2[(1+a^2)^{-1} + 0.20206 - 0.0369a^2 + 0.0083a^4 - 0.002a^6].$$

The screening is included in $\mathcal{F}$. Whether or not screening is important depends on the value of $\Delta = 6Z^{\frac{1}{3}}\xi/(121\delta)$

$$\begin{aligned}
\mathcal{F}(\delta/\xi) &= \ln(111\delta/\xi Z^{\frac{1}{3}}) \text{ for } \Delta \geq 120 \text{ ; complete screening,} \\
\mathcal{F}(\delta/\xi) &= 0, \text{ for } \Delta \leq 0.5 \text{ ; no screening,} \\
\mathcal{F}(\delta/\xi) &= \text{ linear interpolations between values of table 3.2} \\
&\quad \text{for } 0.5 < \Delta < 120 \text{ ; intermediate screening.}
\end{aligned}$$

The use of matrix 3.30 is only valid under certain conditions. Olsen and Maximon state that the results are restricted to high-energy bremsstrahlung i.e., $\epsilon_1, \epsilon_2, k \gg 1$ and the angle (θ) under which the radiation is emitted needs to be small: $u = p\sin\theta \approx p\theta \sim 1$ (in units of mc). The first constraint means that the results fail near the high frequency limit of the bremsstrahlung spectrum where $\epsilon_2 \sim 1$. The error in calculating the total cross section obtained with these approximations is [92, 93] $(Z/137)^2(\ln\epsilon_1)/\epsilon_2$ which is around 1% at 10 MeV energy and Z=26. The region of applicability is discussed further in the next chapter.

3.9.2 Depolarization

The polarization vector for the outgoing electron/positron is not given by Olsen and Maximon. However, their results can be used to calculate the following transfer matrix

$$T_{\text{brem,e}} = \begin{pmatrix} 1 & 0 & 0 & 0 \\ 0 & G+H & F & 0 \\ 0 & E & G & 0 \\ 0 & 0 & 0 & G \end{pmatrix}, \tag{3.31}$$

where

$$\begin{aligned} E &= 4k\xi,\ \epsilon_1 u(2\xi - 1)/I, \\ F &= 4k\xi,\ \epsilon_2 u(1 - 2\xi)/I, \\ G &= 4\epsilon_1\epsilon_2[(1 + ,\ ) - 2u^2\xi^2,\ ]/I, \\ H &= k^2[1 + 8,\ (\xi - 0.5)^2]/I. \end{aligned} \tag{3.32}$$

Both the polarization vector of the incoming and outgoing electron/positron are given relative to the scattering plane (xz-plane) and the direction of the outgoing photon (z-axis). The rotation matrices 3.14 and 3.15 are used to transform the polarization vector from or to the electron or positron system.

3.10 Pair production

3.10.1 Polarization transfer

It follows from the work by Olsen and Maximon [89] that the polarization vector for an electron or positron after pair production, making approximations similar to the ones in the previous section, is

$$T_{\text{pair,e}} = \begin{pmatrix} 1 & D & 0 & 0 \\ 0 & 0 & 0 & L \\ 0 & 0 & 0 & T \\ 0 & 0 & 0 & 0 \end{pmatrix}, \tag{3.33}$$

where

$$D = 8\epsilon(\epsilon - k)u^2\xi^2,\ /I,$$

$$
\begin{aligned}
T &= -4k(\epsilon - k)\xi(1 - 2\xi),\ u/I, \\
L &= k[(2\epsilon - k)(3 + 2,\ ) + 2(k - \epsilon)(1 + 4u^2\xi^2,\ )]/I, \\
I &= [\epsilon^2 + (k - \epsilon)^2)](3 + 2,\ ) + 2\epsilon(k - \epsilon)(1 + 4u^2\xi^2,\ ).
\end{aligned}
$$

Here, ϵ is the energy of the observed electron or positron. The matrix 3.33 for pair production is the transpose of matrix 3.30 with ϵ_2 replaced by $-\epsilon_2$ ($k = \epsilon_1 + \epsilon_2$). This reflects the inverse nature of bremsstrahlung and pair production. The polarization vector of the electron or positron is given relative to the scattering plane (xz-plane) and the direction of the photon (z-axis). The rotation matrices 3.14 and 3.15 are again used to transform the polarization vector to the electron or positron system.

Chapter 4

Implementation of polarization in GEANT

In this chapter the implementation of the theory of chapter 3 in the GEANT-code is discussed. In addition to the polarization sensitive, depolarizing and polarization transferring processes, the effect of multiple scattering on the polarization vector of an electron or a positron is included. The effects of the extensions to the GEANT-code are shown for initially fully circularly polarized photons or for longitudinally polarized electrons in $Nd_2Fe_{14}B$ scattering material. The chapter starts with a short introduction to the GEANT-code.

4.1 The GEANT-code

GEANT [17] is an acronym of GEometry ANd Tracking. It is a widely used Monte Carlo code for simulation of both hadronic and electromagnetic interactions and showers. The first version of GEANT dates from 1974 and was developed at CERN for tracking of a few particles through a simple setup. Over the years several users have expanded the code, increasing the number of processes included and improving the accuracy with which they are simulated. In this thesis version 3.21 of GEANT is used. Because the processes in the polarimeter discussed are all electromagnetic, the hadronic interactions included in GEANT will not be discussed.

In GEANT particles are transported through a medium of different materials and fields, together called 'the setup' and to be specified by the user. The number and sort of particles to be tracked together with their initial

energy and spatial distribution form 'the event generator' which has to be specified by the user. The physics incorporated in the package and the 'electronic dice' take care of the transport of all relevant particles through the setup. During transport a particle loses energy, changes its direction and can create other particles. The way this is done can be influenced by the user by selecting the processes considered during tracking and by setting cutoffs. The cutoffs fall into two categories. The first category specifies the energy below which the particles are no longer tracked; if the energy of the particle falls below this cutoff it is stopped. These cutoffs can be set individually for photons and electrons and positrons. The second category gives thresholds below which energy losses of the particles are simulated as soft processes. This means that the secondary particles are not generated below this cutoff. This second category includes two processes: bremsstrahlung (cutoff BCUTE=Bremsstrahlung CUToff Electrons) and δ-ray production (cutoff DCUTE). The energy loss due to these soft processes is accounted for by increasing the value of the energy loss per unit of length with the proper amount. The setting of the cutoffs together with the selection of the considered processes has a considerable influence on the results obtained and the amount of CPU-time needed to do the calculations.

In GEANT the *total* cross section for the various relevant processes is used to select the process that will take place. *Differential* cross sections are used to calculate the kinematics once a certain process is selected. Appropriately chosen random number distributions select the processes and determine the final kinematics. Details and references can be found in the physics section of the GEANT manual [17]. No polarization sensitivity is included in the code[1].

4.2 Inclusion of the polarization shower in GEANT

The bookkeeping of the position and momentum of a particle and its descendants during tracking is incorporated in GEANT by using FORTRAN common-blocks. To be able to keep track of the polarization of a particle these common-blocks were expanded to include the Stokes parameters

[1]The only exception is the photon polarization after Čerenkov radiation. However, this type of radiation falls outside the scope of the polarimetry discussed in this thesis.

(P_1, P_2, P_3) of equation 3.2. The changes made to the data structures are given in appendix A. The code management package CMZ [94] was used to make all changes and extensions to the GEANT-code.

The position of particles and of elements of the setup is given relative to the so called 'Mother Reference System' (MRS) in GEANT. The polarization of a particle is defined relative to a righthanded reference frame moving with the particle: 'the particle basis'. The exact definition and the recipe of how to construct the particle bases from the MRS are given in appendix A. Besides the MRS and the particle basis a third coordinate system is used in calculating the polarization transfer. It is defined with respect to the scattering plane of the process considered and is therefore conveniently called 'the scattering basis'. Again, the exact definition is given in the appendix. To transform the polarization from one reference system to the other some rotation routines were added to the program library. The rotation matrices are given by equations 3.14 and 3.15.

With the polarization degree of freedom added to the electromagnetic shower, the next step is the incorporation of the polarization transfer during an electromagnetic interaction. Once the electronic dice has decided on the basis of the *total cross section* that a certain interaction will take place a FORTRAN-call is made to the appropriate GEANT subroutine to calculate the kinematics for the process. This is done by applying the Monte Carlo method to the *differential cross section.* **No changes** are made to the cross sections because the polarization effects on both the total and differential cross sections are small; at most a few percent. However, the subroutines are expanded to calculate the polarization transfer **given** the kinematics of the outgoing particle(s) as calculated in the subroutine and the polarization and kinematics of the incoming particle(s). The polarization transfer is calculated for unpolarized target electrons.

For the asymmetry calculation it is assumed that every target electron is polarized. The degree of target polarization is taken into account afterwards by multiplying the calculated asymmetry with appropriate degree of target polarization. The direction of the polarization of the target electrons is set by the user. Although single particles are tracked through the setup the polarization effects are calculated as if every particle represents a polarized beam by giving it the average polarization of the beam. The expansions made to the subroutines are basically FORTRAN-calls to additional subroutines containing the transfer matrices and asymmetries of chapter 3.

Also some extensions were made to the graphics part of GEANT: When

a track is drawn the polarization vector can be represented along with it.

In GEANT it is possible to switch on and off all the physics processes individually. In the next section this property is used to show the effects of the individual processes on the polarization of an initially fully longitudinally or, in photon terminology, circularly polarized beam of either electrons or photons.

4.3 Results of the implementation of polarization in GEANT

Before discussing the individual processes a few remarks are made on the setting of the kinematic cutoffs in GEANT. All particles (electrons, positrons and photons) are tracked until their kinetic energy falls below 10 keV in which case they are stopped. This is the lowest value possible in GEANT. At this threshold value the code uses cross section values which may be assumed accurate to within 10% or better (see the manual [17] for detailed information). The variable DCUTE, the δ-ray cutoff, was set at 100 keV. This means that the generated δ-electrons have at least 100 keV of kinetic energy. This value is higher than the allowed minimum of 10 keV because particles with less than 100 keV kinetic energy will fall below the detection threshold of the trigger detectors used in the experiments. Furthermore, electrons and positrons of lower energy will in most cases be stopped in the material in which they are generated and will not reach the detector at all. It will be clear that an unnecessary low cutoff value implies a waste of CPU-time for the tracking procedure. The cutoff for bremsstrahlung, BCUTE, was set at 1 MeV because, as will be explained later, the polarization transfer from the electron or positron to the photon is not reliable anymore below this energy.

The results shown in the following sections are for initially fully longitudinally polarized beams of electrons, positrons or photons incident on a perpendicularly magnetized $Nd_2Fe_{14}B$ layer. To illustrate the effects of an individual process it is selected by setting the appropriate data record in GEANT and switching all the other processes off. Only the effect of the **first** time that the initial particle scatters is shown in the figures. The particle polarization is always shown relative to the particle frame. The projection of the polarization in the initial beam direction is **not** included.

4.3.1 Multiple scattering

Multiple scattering is, together with continuous energy loss, a process that happens every time when an electron or positron moves from one point to another through, in the GEANT language, a 'sensitive medium'. It implies a series of Coulomb scatterings in which the number of scattering events depends on the path length between the points, the scattering material and the energy of the particle. In GEANT multiple scattering is either simulated by plural Coulomb scattering or by the Molière theory[2] when the number of scattering events in one step is more than 20. Whatever method is used, the result is that the momentum vector of the particle is rotated over an angle. When this angle is ϕ, the component of the polarization vector of the particle in the scattering plane is rotated over an angle θ given by [1][3]

$$\theta = \phi \frac{E_{\text{tot}} - 1}{E_{\text{tot}}}, \tag{4.1}$$

where E_{tot} is the total energy of the particle in units mc^2. From 4.1 it can be seen that for energies $E_{\text{tot}} \gg mc^2$ the polarization of a longitudinally polarized beam follows its momentum. At energies below 5 MeV the relatively slower rotation of the polarization vector becomes of practical significance. Figure 4.1 shows the average longitudinal polarization (relative to the particle frame) of an initially fully longitudinally polarized electron after one multiple scattering step as a function of the energy of the particles. The average scattering angle is also shown. The rotation of the polarization vector was implemented in GEANT by expanding the GMULTS subroutine.

4.3.2 Compton scattering

The theory needed to calculate the polarization transfer and asymmetry in Compton scattering is given in section 3.5. The GEANT subroutine GCOMP, which calculates the kinematics for Compton scattering using the Klein-Nishina formula, was modified to incorporate this theory. The longitudinal polarization transferred to a secondary electron and the depolarization of an initially fully polarized photon beam of 10 MeV are shown in figures 4.2a.

[2] It is also possible to do the simulation with a pure Gaussian distributed scattering angle. This option is not used in this thesis.

[3] For the gyromagnetic ratio the value of 2 is used.

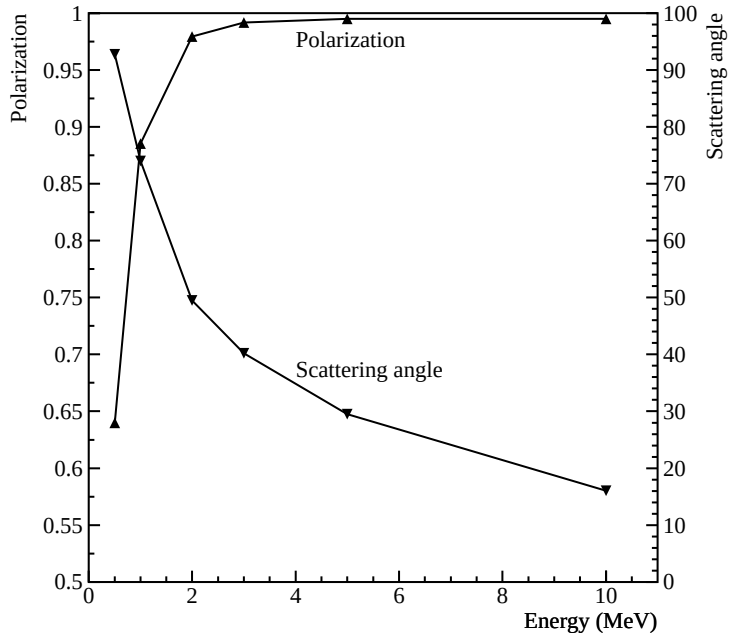

Figure 4.1: *Longitudinal polarization (relative to the particle frame) of an initially fully longitudinally polarized electron and the scattering angle as a function of the energy of the particle after one multiple scattering step. Each triangle is the average over 10000 primary multiple scattering events. The line is meant to guide the eye.*

The scattering asymmetry for the process (see section 3.5) for target electrons which are 100% polarized is shown in 4.2b. The weighted average of the data in this figure and similar figures at other energies is shown in figure 4.2c as a function of the initial photon energy.

4.3.3 Møller and Bhabha scattering

The GEANT subroutine GDRAY samples the energy of the δ electron for Møller and Bhabha scattering on the basis of the differential Møller and Bhabha cross sections. The angle is calculated from energy momentum conservation. The target electron at which the electron or positron scatters is assumed to be a free particle. The scattering is only explicitly calculated when the target electron obtains at least DCUTE=100 keV of kinetic en-

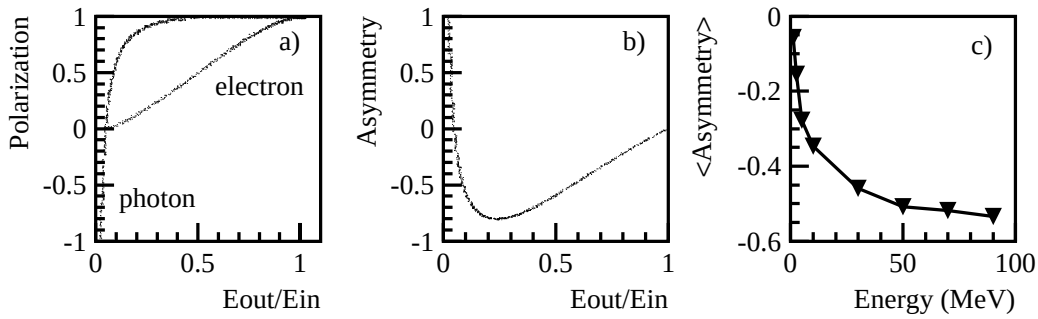

Figure 4.2: *a) The polarization of photons and electrons after Compton scattering of 10 MeV fully circularly polarized photons vs the fraction of transferred energy. b) The scattering asymmetry for Compton scattering of 10 MeV fully circularly polarized photons. c) The weighted average of the data in figure b and similar figures at other initial photon energies as a function of the initial photon energy. The line in is meant to guide the eye.*

ergy. As mentioned, the scattering process below this user determined cutoff is treated as a continuous process. The subroutine GDRAY was expanded with the formulas of 3.6 and 3.7 to handle the depolarization of the initial electron or positron and to calculate the scattering asymmetry for the kinematics as calculated in the routine. The polarization of the target electron after the scattering took place was set to zero. In the case of electron-electron scattering the particle with the highest energy is treated as the ongoing electron for which the depolarization is calculated. Figure 4.3a shows the polarization after one Møller scattering for electrons of 30 MeV as a function of the ratio of the final to the initial total energy of the particle. Figure 4.3b shows the scattering asymmetry. The weighted average of the data in figure b and similar figures at other energies is plotted in figure 4.3c as a function of energy of the initial electron. Figure 4.4 shows similar pictures for Bhabha scattering but for an initial positron energy of 10 MeV.

The weighted average values of the scattering asymmetry are sensitive to the setting of DCUTE because lowering DCUTE gives rise to a large increase in energy-asymmetric scatterings i.e., scatterings in which the electron loses almost no energy, with very low asymmetry values. This decreases the average value. To give an example: at DCUTE=100 keV the average asymmetry for Bhabha scattering at 1 MeV is -0.27 while at DCUTE=10 keV this value

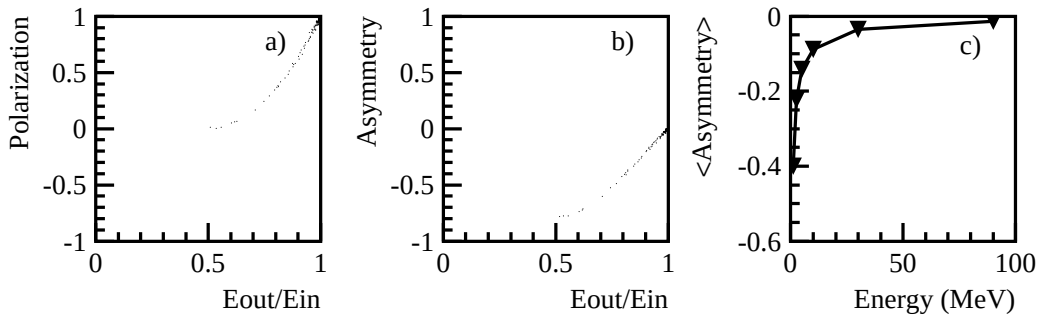

Figure 4.3: *a) Depolarization of an electron with 30 MeV kinetic energy due to Møller scattering as a function of the ratio of the final and initial electron energy. b) The scattering asymmetry for the process. c) The weighted average of the data in figure b and similar figures at other energies as a function of the initial kinetic energy of the electron. DCUTE was set at 100 keV. The line is meant to guide the eye.*

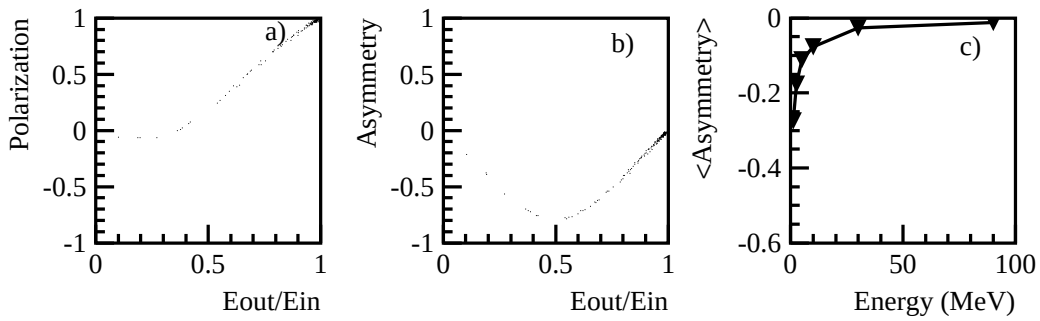

Figure 4.4: *Same as figure 4.3 but for Bhabha scattering of a positrons of 10 MeV.*

is -0.04. This also illustrates that the polarization sensitivity of an actual Møller/Bhabha polarimeter depends dramatically on the events accepted as being Møller or Bhabha scatterings. By rejecting the very energy-asymmetric but often occurring events, the weighted average asymmetry increases at the cost of a poorer countrate statistics.

4.3.4 Annihilation in flight and at rest

For the annihilation of a positron only the scattering asymmetry of the process as discussed in section 3.8 is implemented in GEANT. The polarization of the created photons is set to zero in all cases. Three GEANT routines were edited and extended: GANNI, GANNIR and GANNI2. The first of these three calculates the kinematics for two- and one-photon[4] annihilation in flight, while the other two handle annihilation at rest. Annihilation at rest occurs each time the kinetic energy of the positron falls below the tracking cutoff. The asymmetry is set to zero in this case. The formulas to calculate the asymmetry for annihilation in flight of section 3.8 were included in GANNI. Figure 4.5a shows the scattering asymmetry for a 10 MeV fully longitudinally polarized positrons annihilating in NdFe. The weighted average of the data in this figure and similar figures at different energies, is plotted as a function of the positron kinetic energy in figure 4.5b. The average asymmetry changes sign for an initial positron kinetic energy somewhere between 5 and 10 MeV. Again, the annihilation-polarization asymmetry of a polarimeter will depend on the events accepted as being due to annihilation in flight.

4.3.5 Bremsstrahlung

The theory to calculate the polarization transfer to photons from electrons or positrons as a result of bremsstrahlung was summarized in section 3.9 for the 'high-energy' case. The results were based on the calculations done by Olsen and Maximon [89]. This is one of the few published calculations on the polarization transfer of bremsstrahlung which can be used for the extreme relativistic ($\epsilon_1, \epsilon_2, k \gg 1$; units of mc^2) case with small scattering angles $\theta = O(1/\epsilon_1)$). However, there are several approaches to calculate bremsstrahlung without considering the transfer of polarization. The review by Koch and Motz [92] gives a nice overview including a discussion of the approximations made in the calculations. In a more recent article Seltzer and Berger [95] present bremsstrahlung cross sections based on a synthesis of various theoretical results.

In GEANT both the energy and the scattering angle of the bremsstrahlung photon are sampled in the subroutine GBREME. For the energy a

[4] If the electron is bound to a nucleus the annihilation process can result in a single photon

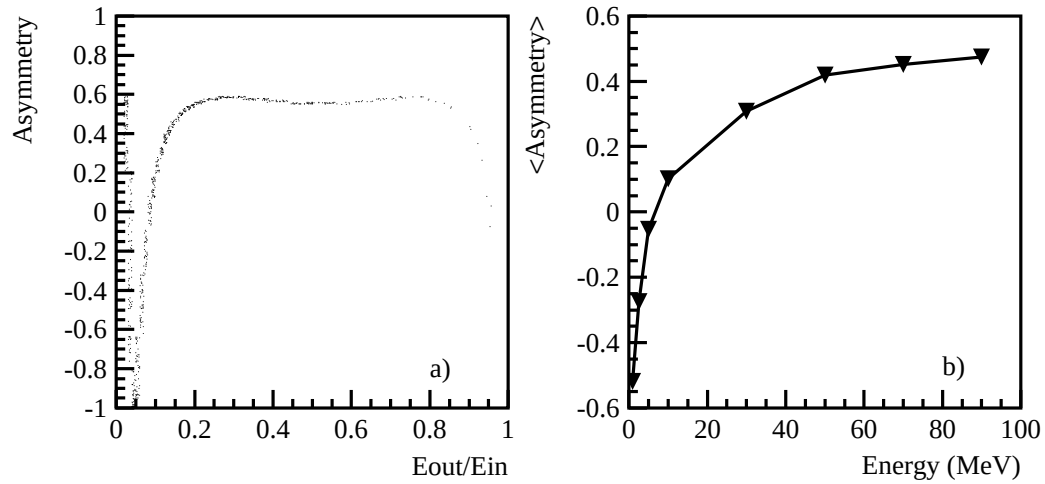

Figure 4.5: *a) The scattering asymmetry for annihilation in flight of a 10 MeV fully longitudinally polarized positron in NdFe as a function of the ratio of the energy of one of the photons and the initial total positron energy. b) The weighted average of the data in figure a and similar figures at other energies as a function of the initial positron kinetic energy. The line is meant to guide the eye.*

parametrization is used which is fitted to the results of Seltzer and Berger [95]. They found a good overall agreement between their calculated results and the available data. The parameterization used in GEANT reproduces their results with a maximum error of 10% below 50 MeV and less than 5% above 50 MeV [17]. The scattering angle of the photon is not completely determined if the energy of the photon and electron/positron after the scattering are known because bremsstrahlung is a three body process (electron or positron, photon and external field). The angle is sampled by using a parameterization of a cross section calculated by Tsai [96, 97], who took into account screening effects by using both elastic and inelastic atomic form factors. Such inelastic effects were ignored by Olsen and Maximon. For energies of a few MeV the parameterization becomes less accurate but at these energies bremstrahlung is not the dominant process. The electron energy is reduced with the energy transferred to the photon and its direction of motion is kept unchanged.

The formulas to calculate the energy and scattering angle of the pho-

ton used in GEANT are not restricted to the high-energy regime. Care should therefore be taken in calculating the polarization transfer with the high-energy results of Olsen and Maximon on the bases of the kinematics calculated in GEANT. Energies and scattering angles where the results of Olsen and Maximon can not be applied may become problematic. Figure 4.6 shows the polarization transfer to photons and the remaining polarization from 5 and 10 MeV longitudinally polarized electrons due to primary bremsstrahlung in NdFe. Most events fall in the region where the Olsen and Maximon theory may be applied. This region is defined as $\epsilon_2, k > 2$ and $\theta < 5/\epsilon_1$ (energy in units mc^2). The resulting polarization transfer shown in the figure is comparable with the transfer curves given in the paper by Olsen and Maximon. The events lie in a band and not on a single line because the scattering angle of the photon is not uniquely defined by the energies of the particles; the interaction is a three body process. The events outside the application range of the Olsen and Maximon calculations deviate clearly from the main branch, leading even to unphysical results with degrees of polarization larger than one. For incident electrons of 10 MeV the number of these events is already reduced considerably. At energies above 10 MeV their contribution becomes less and less.

In the routine GBREME the polarization of the electron and photon is set to zero if the incident energy is less than 5 MeV. Above this energy the same is done for all events with ϵ_2 or $k < 2$ and events with initial energies below 10 MeV and $\theta > 5/\epsilon_1$. Above 10 MeV the results at large scattering angles are accepted because they hardly deviate from the small-angle results. Because bremsstrahlung is a relatively unimportant process below 10 MeV the effects on the final results are expected to be small if a full Monte Carlo simulation with all processes included is performed.

4.3.6 Pair production

Bremsstrahlung and pair production are inverse processes. Once the results for bremsstrahlung are obtained the polarization transfer in pair production is easily obtained via a substitution rule (see section 3.10). Olsen and Maximon [89] calculated the polarization transfer in pair production using this rule. The results may be applied to high energies and small angles i.e., $k, \epsilon_1 = \epsilon, \epsilon_2 = k - \epsilon \gg 1$, $\theta_1 = O(1/\epsilon_1)$ and $\theta_2 = O(1/\epsilon_2)$ (units of mc^2), where ϵ_1, ϵ_2 and k are defined in section 3.9. As in the case of bremsstrahlung, there are several calculations for pair production without considering the polarization

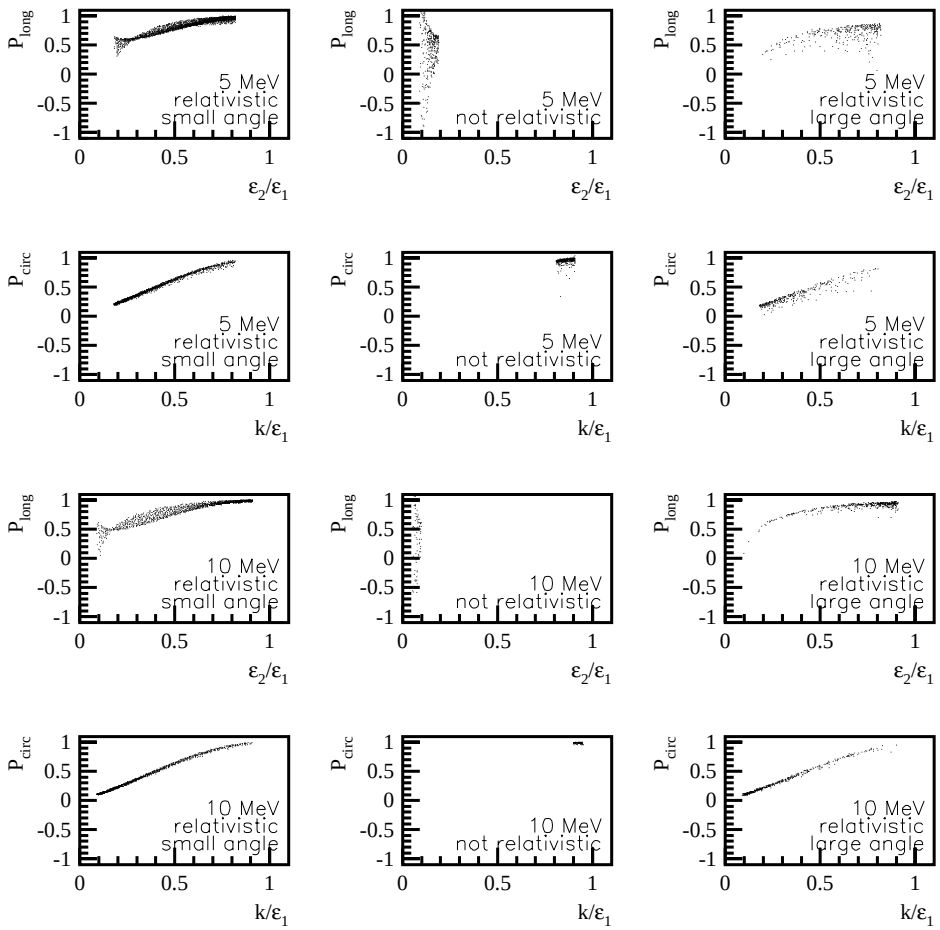

Figure 4.6: *Polarization transfer and depolarization in bremsstrahlung. The upper two rows are for a 5 MeV electron, the lower two rows for a 10 MeV electron. The left column shows events in the validity range (defined in the text) of the Olsen and Maximon theory. The second and third columns show the polarization transfer outside this range. BCUTE was set at 1 MeV.* P_{long} *is the longitudinal polarization of the electron and* P_{circ} *is the circular polarization of the photon. Both are given relative to the particle frame (see appendix A).*

transfer. Motz, Olsen and Koch [98] wrote a good review of pair production including the conditions of validity of the various formulas presented.

The subroutine GPAIRG handles pair production in GEANT. The energy of one of the particles (electron or positron) is sampled from the Coulomb corrected screened Bethe-Heitler differential cross section [17]. This cross section is subject to the same validity conditions as mentioned above. It is rather surprizing that it is nowhere checked in the GEANT code whether these conditions are fullfilled. However, below a photon energy of 2.1 MeV the electron energy is sampled from a uniform distribution over the interval $m \rightarrow k/2$. The scattering angles are sampled using a cross section of Tsai [96, 97].

Figure 4.7 shows the polarization transfer for a 5 MeV and a 50 MeV photon. Most of the events fall in a band which agrees with the results presented by Olsen and Maximon. Again, the band reflects the three-body behaviour. The validity region of the Olsen and Maximon results is defined as $\epsilon_{1,2} > 2$ and $\theta_{1,2} < 5/\epsilon_{1,2}$. For energies $\epsilon_{1,2} < 2$ the polarization transfer takes unphysical values larger then one sometimes, illustrating that the theory is not correct in this energy regime. For incident energies below 5 MeV the polarization of the electron and positron is set to zero. Above this energy this is also done for events with $\epsilon_{1,2} < 2$. The polarization transfer for scattering angles with $\theta_{1,2} > 5/\epsilon_{1,2}$ is not dramatically different from the results with smaller θ-values. Those results are accepted without setting the polarization transfer to zero. However, it may be necessary to remove these events at energies above 100 MeV, but this has not been checked.

4.4 Concluding remarks on using the extended version of GEANT

The examples shown in the previous section were for longitudinally polarized electrons and circularly polarized photons. The transfer matrices and asymmetries also include the effects of transverse and linear polarization. However, the effects of these components are in general smaller in magnitude and therefore they are not discussed in this chapter.

As may be clear from the previous sections, the validity of the implemented theory is sometimes restricted to specific energy regimes, and the polarization transfer is not calculated in every process. This should be kept in mind when using the extended version of GEANT.

The setting of the cutoffs can be critical in some geometries. For example

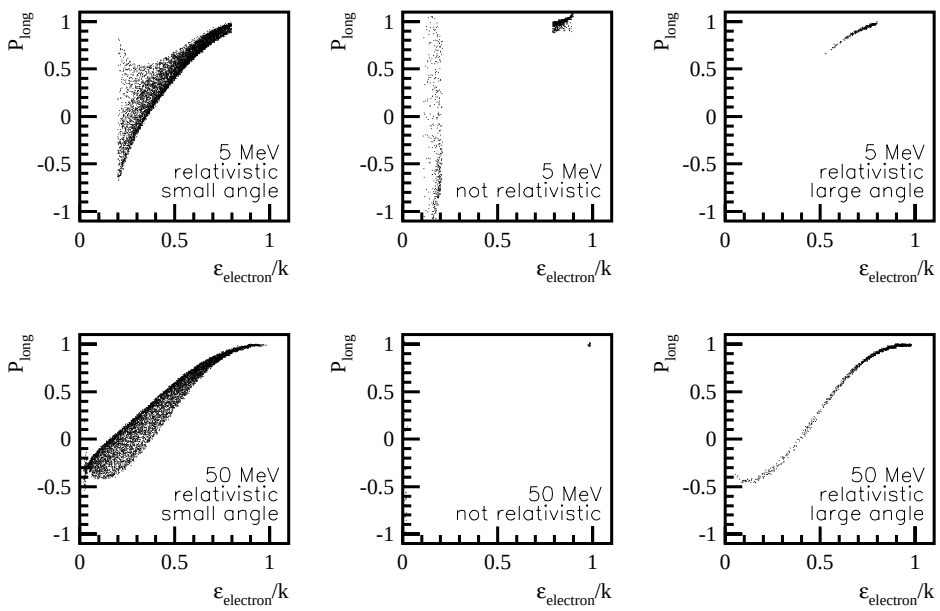

Figure 4.7: *Polarization transfer from a photon to an electron in pair production. The top row is for 5 MeV, the bottom row for 50 MeV photons. The figures show the effects of applying the results of Olsen and Maximon outside their validity region (see text). The meaning of* P_{long} *is explained in the caption of figure 4.6.*

a geometry with a thin target and a high threshold for δ-ray production (DCUTE) may lead to too large asymmetry values, because the events with low asymmetry values are not taken into account. In general, the cutoffs should be set at such a value that the polarization transfer and asymmetry is calculated for all the particles that will trigger the detectors in the setup.

It is not easy to estimate how accurate the polarization results are Simulations of 'polarized beam production experiments' where the polarization of the primary and secondary beam is measured may lead to a better insight in the accuracy of the calculated absolute results. However, the simulations can be used to obtain the optimal setting of a polarimeter setup without precise knowledge of the accuracy of the absolute asymmetry values.

Chapter 5

The $Nd_2Fe_{14}B$ scattering foil

As described in chapter 2, most electron and positron polarimeters have a scattering target or a scattering foil as a central component. In the polarimeter under discussion, a polarized target containing electrons with aligned spins is needed. The scattering material chosen is $Nd_2Fe_{14}B$, or in shorthand notation NdFe. With this hard magnetic material a novel scattering material is introduced in polarimetry. The percentage of aligned electrons in magnetized NdFe is estimated and its merits are compared with features of 'classical' soft magnetic materials. The final estimate for the NdFe layer used in the prototype polarimeter amounts to $P_t = 3.7\%$.

The discussion is not limited to the at present most widely used and industrialized $Nd_2Fe_{14}B$, but widened to the family of materials $R_2Fe_{14}B$, where R is a rare earth element in general.

5.1 Spin polarized scattering foils

The electron and photon polarimeter introduced in chapter 1 requires a scattering foil containing electrons with aligned spins. Nowadays, most polarimeters are equipped with the soft magnetic material $Fe_{49}Co_{49}V_2$ (FeCo). The properties of this material relevant to polarimetry are given in table 5.1 together with those of NdFe, the permanent magnetic material that forms the central part of the polarimeter investigated in this thesis. For comparison pure iron, the material used in first-generation polarimeters, is included in this table.

When using FeCo or pure iron an external field is used to saturate the

Table 5.1: *Properties of bulk materials used as scattering foils in polarimeters. P_t is the percentage of polarized electrons. The last column gives the minimum thickness commercially available. The P_t values for α-Fe and $Fe_{49}Co_{49}V_2$ are taken from the thesis of Wichers [35]. The P_t value for $Nd_2Fe_{14}B$ is calculated in this chapter.*

material	magnet type	magnetization direction	P_t	minimum thickness
α-Fe	soft	in foil plane	5%	≈ 5 μm
$Fe_{49}Co_{49}V_2$	soft	in foil plane	7.5%	≈ 5 μm
$Nd_2Fe_{14}B$	hard	perpendicular to foil	3.7%	1 mm

foil magnetization. Once magnetized in a certain direction a small holding field is necessary to maintain the magnetization. For FeCo the saturation and holding field are ≈ 30 A/cm and ≈ 3 A/cm [35], respectively. The use of a soft magnetic material has the advantage that the magnetization can be reversed by simply reversing the current in the magnetizing coils. In case of a hard magnetic material the magnetic layer itself has to be turned or a chessboard pattern with alternating orientation of the 'black and white' magnets has to be used. It is conceivable, depending on the energy of the incident electrons, positrons or photons, to place several NdFe layers behind each other, sandwiched between thin location sensitive detectors.

In soft magnetic materials the magnetization direction is parallel to the surface direction. For polarimetry of longitudinally (or circularly) polarized beams the magnets must be placed under an angle α with respect to the beam axis to achieve a magnetization component in the beam direction. This lowers P_t by a factor $\cos\alpha$, destroys the axial symmetry around the beamaxis and introduces a systematical asymmetry in the layout of the polarimeter. On the other hand, a thin layer of the hard magnetic material NdFe can be magnetized perpendicular to its surface preserving its polarization without external holding field. The great advantage of a layer of NdFe is that it can be placed perpendicularly to the incident beam and that it needs no external holding field. This geometry retains axial symmetry and utilizes the full magnetization of the scatterer. Unfortunately, these advantages have to be balanced against a lower target polarization.

In the next sections the percentage of polarized electrons in the NdFe target used in the present study is estimated as P_t=3.7%. This value is, unfortunately, lower than was hoped for at the start of the investigation.

The discussion below is not limited to $Nd_2Fe_{14}B$ but is widened to the family of materials $R_2Fe_{14}B$, where R is a rare earth ion. The following steps are taken to estimate the percentage of polarized electrons in those materials:

I The magnetic moments of R- and Fe-ions are combined and the contribution of the electron spins to this moment is calculated. This results in an estimate of the number of polarized electrons in $R_2Fe_{14}B$ single crystals[1] at a temperature of T=0 K. The boron atom B is needed for the metallurgy but does not contribute to the magnetic moment.

II The effect of a non-zero temperature on the magnetization of the single crystals is taken into account.

III The reduction of the target polarization due to the transition of $Nd_2Fe_{14}B$ single crystals to bulk material is estimated. The factors that play a role are the contaminations contained in the bulk material and the alignment of the magnetic grains which constitute the actual magnetic material.

5.2 Number of aligned electron spins in $R_2Fe_{14}B$

In the first step the magnetic moments of R- and Fe-ions are determined together with the contribution of the electron spins to this moment. Thereafter the two moments are combined and finally an estimate for the number of aligned electron spins in $R_2Fe_{14}B$ at T=0 K is obtained.

5.2.1 Magnetic moment of R-ions

The magnetic moment of R-ions is due to the combined spin and orbital angular momenta, $\vec{S}$ and $\vec{L}$, respectively. The total angular momentum, $\vec{J}$, is given by $\vec{J} = \vec{L} + \vec{S}$. The magnetic properties of rare earth ions are related to the electrons in the 4f shell which is gradually filled when going through the rare earth series from Ce to Lu. The way to couple $\vec{S}$ and $\vec{L}$ follows from the three Hund rules [100, 101]. The first of these Hund rules describes how to couple the electron spins in the atomic shell responsible for the spin moment. One should add the individual spins to the maximum allowed by

[1]Single crystals contain only $R_2Fe_{14}B$ crystals. A unit cell of the material contains four formula units $R_2Fe_{14}B$, i.e. $4 \times 17 = 68$ atoms [99].

the Pauli principle. The second rule gives the prescription for the coupling of the orbital angular momenta. They should be combined to the maximum L value allowed by the Pauli principle and the first rule. The third rule states that $J = |L - S|$ for shells that are less, and $J = L + S$ for shells that are more than half filled. This rule determines the angle between $\vec{L}$ and $\vec{S}$. The notation used in the literature to characterize the ion is ${}^{2S+1}L_J$. As an example of the application of Hund's rules Nd is taken. For Nd^{3+} the ground state level is the $4f^3$ state, i.e. there are three electrons in the $4f$-shell. With $l = 3$ there are $2(2l + 1) = 14$ possible states; two for every magnetic quantum number $m_l = -3, -2, -1, 0, 1, 2, 3$. The first Hund rule gives: $S = \frac{1}{2} + \frac{1}{2} + \frac{1}{2} = \frac{3}{2}$. The second rule: $L = 3 + 2 + 1 = 6$, and the third one $J = L - S = 6 - \frac{3}{2} = \frac{9}{2}$. So Nd^{3+} is in the ${}^4I_{9/2}$ state.

The magnetic moment $\vec{M}$ is given by

$$\vec{M} = -\frac{e}{2m}(\vec{L} + 2\vec{S}). \tag{5.1}$$

This moment is not parallel to $\vec{J}$ but precesses around it. The effective magnetic moment is given by the projection of $\vec{M}$ on $\vec{J}$. The projection of the spin magnetic moment $2\vec{S}(e/2m)$ on $\vec{J}$ is

$$|\vec{M}_S^{\text{eff}}| = 2\frac{e}{2m}|\vec{J} \cdot \vec{S}| = 2\mu_B|g - 1|\sqrt{J(J+1)} = 2\mu_B\sqrt{G}, \tag{5.2}$$

where $\vec{J} \cdot \vec{S} = \vec{L} \cdot \vec{S} + |\vec{S}|^2 = \frac{1}{2}(|\vec{J}|^2 - |\vec{L}|^2 + |\vec{S}|^2)$ is used. The Landé factor is $g = 1 + (J(J+1) - L(L+1) + S(S+1))/(2J(J+1))$. $G = (g-1)^2 J(J+1)$ is the de Gennes factor and $\mu_B = \hbar e/2m$. In the presence of an external or exchange field along the z-axis the effective spin magnetic moment along this quantization axis is $M_{S_z}^{\text{eff}} = 2\mu_B|g - 1|J$, with its direction being determined by the third Hund rule.

5.2.2 Magnetic moment of Fe-ions

The magnetic moment in iron is in essence due to the spin of the electrons in the $3d$ shell. The contribution of the orbital angular momentum amounts only to around 4% [100] and will be neglected. The magnetic moment is $2.2\mu_B$ for α-Fe. To estimate the magnetic moment of iron in $R_2Fe_{14}B$ the magnetization of $Y_2Fe_{14}B$ at 4 K (31.4 μ_B) can be used because yttrium[2] gives

[2] Y is often treated as a rare earth metal because of its similar electronic structure.

no contribution to the magnetic moment [102]. This gives 31.4/14=2.24 μ_B per iron atom which is slightly more than the free iron value. The fourteen iron magnetic moments are coupled collinearly [99].

The value of 2.24 μ_B for the iron magnetic moment is not used by everybody in the literature. Herbst [99] for example estimates the iron magnetic moment by taking an average over the magnetic moments of $R_2Fe_{14}B$ with R from the series La, Ce, Lu, Y and Th which ions do not contribute to the magnetic moment themselves. This yields 2.1 μ_B. The value of 2.24 μ_B was chosen here because the temperature effects, discussed later on, are also based on $Y_2Fe_{14}B$ measurements. Besides this, the measured saturation magnetization at T=4 K is well reproduced by using this value (see below). The P_t-values calculated below are 0.4% lower when a value of 2.1 μ_B is taken for the magnetic moment of the iron ion.

5.2.3 Coupling of the moments of R- and Fe-ions

The rare earth $4f$ and iron $3d$ spin magnetic moments are coupled antiparallel i.e., the iron rare earth interaction is antiferromagnetic [99]. This behaviour is explained by considering the rare earth $5d$ electrons. This band of electrons is almost empty and therefore almost totally above the Fermi level. The intra-atomic $4f$-$5d$ exchange interaction is ferromagnetic and leads to an induced $5d$ moment. The interaction of this induced moment with the iron $3d$ electrons, which are mostly below the Fermi level, is strongest with the minority $3d$ electrons. This is because the minority band is less filled than the majority band and therefore closest to the rare earth $5d$ band. This leads to an antiferromagnetic coupling between the (induced) rare earth $5d$ and iron $3d$ moment. Thus, the resulting $4f$-$3d$ coupling is antiferromagnetic.

To arrive at an estimate for the electron spin moment M_e (in units of μ_B) in a single crystal $R_2Fe_{14}B$, the effective total R spin moment in the magnetization direction is subtracted from the total iron spin moment i.e.,

$$M_e = 14 \times 2.24 - 2 \times 2|g-1|J. \tag{5.3}$$

If this spin moment is considered as being caused by the difference in occupation numbers for majority (up) and minority (down) spin electrons, the fraction of polarized electrons in single crystal $R_2Fe_{14}B$ is obtained as:

$$P_t = \frac{M_e}{N_e} \cdot 100\%, \tag{5.4}$$

where N_e is the total number of electrons in $Nd_2Fe_{14}B$. The results are given in table 5.2. The table also contains the calculated total magnetic moments $M_s(0K) = 14 \times 2.24 \pm 2 \times gJ$ where the sign is determined by the third Hund rule. These are to be compared with the measured values for the saturation magnetization (M_s) at 4 K. The good agreement between the calculated and measured values shows that the above treatment leads to reasonable estimates of the saturation magnetization M_s at T=4 K. Table 5.2 also contains values for $2(g-1)/g$, the fraction of the spin magnetic moment in the total rare earth magnetic moment, which will be used below.

5.3 Temperature effects

The next step is to estimate the polarization at 295 K. At this temperature the total magnetic moment of the rare earth component in $R_2Fe_{14}B$ can be estimated following the method described by Hirosawa et al. [102] using a two-sublattice model. In this model the iron atoms in a unit cell form a sublattice that behaves independently of the sublattice formed by the R-ions. The temperature dependence of the iron sublattice magnetization is taken identical with that of $Y_2Fe_{14}B$ (yttrium does not contribute to the magnetic moment itself). The magnetic moment of the R sublattice at 295 K is estimated as[3] $M_s(Y;295K) - M_s(R;295K)$, where $M_s(R;295K)$ is the magnetic moment of $R_2Fe_{14}B$ single crystals at 295 K.

Assuming that the fraction $2(g-1)/g$ of the spin magnetic moment in the rare earth component is independent of the temperature, the spin moment of $R_2Fe_{14}B$ single crystals at 295 K is:

$$M_e(295K) = M_s(Y;295K) - \frac{2(g-1)}{g}(M_s(Y;295K) - M_s(R;295K)). \quad (5.5)$$

Applying this with $M_s(Y;295K) = 27.8\mu_B$ [99] and using equation 5.4 leads around room temperature and in single crystals to target polarization values of up to and slightly beyond 5%, as given in detail on the bottom line of table 5.2.

Figure 5.1 shows the target polarization for single crystal materials as a function of the spin moment of the rare earth atom ($\sqrt{G}$) at 295 K. Because the rare earth and iron spin moments are antiparallel the target polarization

[3] Hirosawa et al. [102] argue that this magnetization can be approximated with a Brillouin function which implies that a two-sublattice model is a reasonable assumption.

Table 5.2: *Overview of relevant parameter values for $R_2Fe_{14}B$* **single crystals** *for a selection of rare earth ions. The values for the magnetic moment at saturation per formula unit $R_2Fe_{14}B$ (M_s) measured at 4 K and 295 K are taken from table IV in the review article by Herbst [99]. M_e is the contribution of the electron spin moment to the magnetic moment. All values for M_s and M_e are given in μ_B per formula unit. The intensity of magnetization I (in Tesla) and magnetization M per formula unit (in μ_B-units) are connected via $I = MN_A\rho\mu_B\mu_0/A$ where N_A is Avogadro's constant, ρ is the density, μ_B is the Bohr magneton, μ_0 is the permeability of free space and A is the atomic weight. The results are based on a magnetic moment of 2.24 μ_B per Fe-ion.*

	^{59}Pr	^{60}Nd	^{62}Sm	^{64}Gd	^{65}Tb	^{66}Dy	^{67}Ho	^{68}Er	^{69}Tm	^{70}Yb
J	4	9/2	5/2	7/2	6	15/2	8	15/2	6	7/2
L	5	6	5	0	3	5	6	6	5	3
S	1	3/2	5/2	7/2	3	5/2	2	3/2	1	1/2
g	0.80	0.73	0.29	2.00	1.50	1.33	1.25	1.20	1.17	1.14
$\sqrt{(G)}$	0.89	1.36	2.11	3.97	3.24	2.66	2.12	1.60	1.08	0.57
ρ(g/cm^3)	7.54	7.60	7.72	7.87	7.96	8.05	8.12	8.22	8.26	8.36
N_e	487	489	493	497	499	501	503	505	507	509
A	140.91	144.24	150.36	157.25	158.93	162.50	164.93	167.26	168.93	173.04
gJ	3.2	3.3	0.7	7.0	9.0	10.0	10.0	9.0	7.0	4.0
$2(g-1)/g$	-0.50	-0.75	-5.00	1.00	0.67	0.50	0.40	0.33	0.29	0.25
M_s at 0 K	37.8	37.9	32.8	17.4	13.4	11.4	11.4	13.4	17.4	23.4
M_e at 0 K	28.2	26.5	24.2	17.4	19.4	21.4	23.4	25.4	27.4	29.4
P_t 0 K (%)	5.8	5.4	4.9	3.5	3.9	4.3	4.6	5.0	5.4	5.8
M_s at 4 K	37.6	37.7	33.3	17.9	13.2	11.3	11.2	12.9	18.1	≈23
I_s at 4 K (T)	1.85	1.86	1.65	0.89	0.66	0.57	0.57	0.66	0.93	1.18
M_s at 295 K	31.9	32.5	30.2	17.5	14.0	14.0	15.9	17.7	22.6	≈23
I_s at 295 K (T)	1.57	1.60	1.49	0.87	0.70	0.71	0.81	0.90	1.16	1.18
M_e at 295 K	25.8	24.3	15.8	17.5	18.6	20.9	23.0	24.4	26.3	26.6
P_t at 295 K (%)	5.3	5.0	3.2	3.5	3.7	4.2	4.6	4.8	5.2	5.2

P_t decreases with an increasing effective spin magnetic moment $\sqrt{G}$ in the rare earth component.

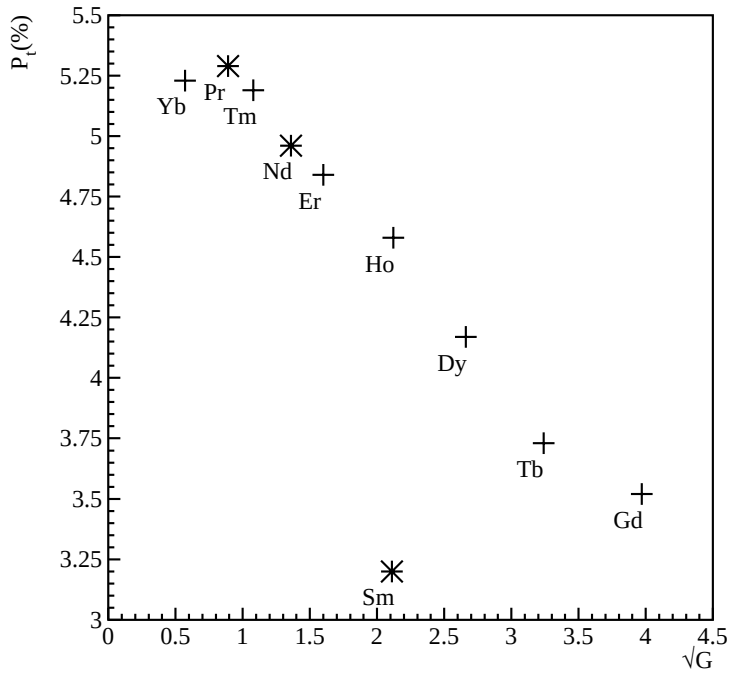

Figure 5.1: *Estimated percentage of polarized electrons (P_t) vs the de Gennes factor $\sqrt{G}$ (see text) for $R_2Fe_{14}B$ single crystals at 295 K. The P_t values form two bands as a result of the third Hund rule: One for Pr, Nd and Sm with $J = |L - S|$ and one for the other elements with $J = L + S$. The corresponding percentage of polarized electrons in a $R_2Fe_{14}B$ magnet is found by multiplying with the contamination factor and the misalignment factor (see 5.4).*

5.4 From single crystals to bulk material

The next step is to go from single crystals to bulk material. Rare earth magnetic materials can be made in several ways [99], but encountered mostly in two forms: 'melt-spun' and 'sintered' magnets. The NdFe magnets used in this thesis are sintered. They are made along the lines described by Sagawa

et al. [103] from induction melted ingots which are substantially enriched in Nd and B compared to $Nd_2Fe_{14}B$. The ingots are crushed, milled, and pulverized to powder with a particle size of ≈ 3 μm. The powder is then aligned in a magnetic field ($\approx$ 800 kA/m) and pressed perpendicularly to the alignment direction. The result is sintered at $\approx$ 1370 K in argon gas for one hour and cooled quickly. A post-sinter anneal finishes the procedure. During the process two phases, $Nd_{1+\epsilon}Fe_4B_4$ and an Nd-rich phase, are formed beside $Nd_2Fe_{14}B$. Presumably these two contaminating phases do not contribute to the magnetic polarization. Durst and Kronmüller [104] give volume fractions of 5% and 10% for the two phases, respectively, for a sintered NdFe magnet from the Vacuumschmelze GmbH, Hanau. The average angle of the $Nd_2Fe_{14}B$ grain anisotropy with the alignment axis for their magnets was 9.5°. The combination of the contamination factor and misalignment factor leads to $P_t = 0.85 \times \cos(9.5) P_t(295K) = 0.84 \times 5.0\% = 4.2\%$ for NdFe. However, this number can change depending on the values of the contamination and misalignment factor. They have to be determined for each magnetic material individually. The contamination factor can be found by measuring the saturation magnetization of the magnet and dividing it by the saturation magnetization of single crystal material: $I_s(measured)/I_s(295K)$, where $I_s(295K)$ is given in table 5.2. The misalignment factor is found by measuring the remanence magnetization of the magnet and dividing it by the saturation magnetization of the magnet: $I_r(measured)/I_s(measured)$. The next section explains how this is done for the NdFe magnetic material used in the polarimeter.

5.5 The $Nd_2Fe_{14}B$ magnet used in the polarimeter

The magnetic layer used in the prototype polarimeter was a disk with a diameter of 44 mm, made of premium quality NdFe according to the present state of art and obtained from Goudsmit[4] company. It was etched prior to magnetization from 1 mm to 0.5±0.05 mm thickness with good homogeneity apart form the outer edges which became slightly thinner. At a thickness of 0.5 mm the energy lost by minimum ionizing electrons in NdFe is approximately the same as in the 1.6 mm silicon of the four SSDs together used in the

[4]Goudsmit, Petunialaan 19, Waalre - Holland

polarimeter. After the etching process the disk was magnetized at Goudsmit using a magnetic field of 2000 kA/m (B $\approx$ 2.5 T). The resulting magnetic polarization at the workpoint[5] of the magnet was I_{wp} = 1.04 T. This was measured by placing the foil in a Helmholtz coil while integrating the current from the coil [101, 105]. From the obtained flux and the dimensions of the disk the magnetization at the workpoint was calculated.

A measurement to obtain the contamination and alignment factor was done at Philips Natuurkunde Laboratory using a vibrating sample magnetometer (VSM) of Oxford instruments. In a VSM [100], the magnet is vibrating in an external magnetic field. In coils positioned around the vibrating magnet a voltage is induced which is compared with the signal obtained from a calibration magnet. The measurement gives directly the magnetization I of the magnet. The magnetization curve of the vibrating sample was obtained by varying the external field in small steps from 0 T to 9 T (saturation) via 0 T (remanence) to -2 T and back to 0 T again.

The dimensions of the VSM were too small for handling the diameter of 44 mm of the magnet used in the polarimeter. However, a measurement could be done with a smaller disk of equivalent NdFe material with a diameter of 10 mm and a thickness of 4 mm. The saturation and remanence magnetization measured for this material were I_s = 1.28 T and I_r = 1.19 T, respectively. This means a contamination factor of 0.80 and a misalignment factor of 0.93 or an average misalignment angle of 21.7°. If the contamination and misalignment factor are taken into account the final electron polarization for the NdFe target is $P_t = 0.74 \times 5.0\% = 3.7\%$. The quality of the magnet for application in a polarimeter is less than the magnet discussed in the article by Durst and Kronmüller [104] (see above). This underlines the fact that those numbers depend on the actual quality of the NdFe material used for the magnet.

The resulting polarization of 3.7% for the NdFe magnet is low compared to the 6.5% effective polarization when using a soft FeCo magnet placed under an angle of 30° to the beam axis. This number is also below the 4

[5]Each permanent magnet can be characterized by a so-called workpoint. At both ends of a permanent magnet free magnetic poles are induced which give rise to a magnetic field in a direction opposite to the magnetization direction [100, 101]. This demagnetizing field H_d is proportional to the magnetization: $\vec{H}_d = -N_d\vec{M}$, where N_d is the demagnetizing factor. The sum of the magnetization and the demagnetization determine the magnetization of the magnet which depends on the size and shape of the magnet. However, for the percentage of polarized electrons in the target the shape of the magnet is of no influence.

to 5% expected when this investigation was started. However, the absence of magnetizing coils and the axial symmetry when using NdFe were considerations for investigating NdFe for the first time as a scattering foil in a polarimeter. NdFe magnets of the best quality available today [106] reach remanence values of $I_r = 1.35$ T which gives a target electron polarization of $P_t = 4.2\%$. If the quality of the NdFe magnets is further improved it might well be possible to come closer to the maximum possible value of $P_t = 5\%$. The use of $R_2Fe_{14}B$ magnets with rare earth ions different from Nd might also be worthwhile considering.

Chapter 6

The NdFe polarimeter: tests and simulations

This chapter presents test experiments with one basic layer of the polarimeter introduced in chapter 1. The properties of the silicon strip detectors are reviewed after an introduction on what is tested with the prototype polarimeter. The experiments with the polarimeter, their results and Monte Carlo simulations of the experiments are covered in the main part of the text.

In an experiment with β-rays from a ^{106}Ru/Rh source with a convenient half-life of one year and an endpoint energy of 3.5 MeV no polarization sensitivity was found. From a Monte Carlo simulation of this experiment with the extended GEANT code of chapter 4 it became clear that a background of scattering events insensitive to polarization decreased the sensitivity of the layer to below the detection limit.

The prototype layer was also tested with ^{12}N and ^{12}B sources. Both sources have a half-life below 21 ms and endpoint energies above 10 MeV. They were produced online with a Van de Graaff accelerator. The experiments performed with the sources suffered from background radiation from the production process. An extraction of a scattering asymmetry turned out to be impossible in the off-line analysis. However, simulations with electrons and photons with energies from 10 MeV to 90 MeV predict a detectable scattering asymmetry. The background effects which decreased the sensitivity of the layer at energies below 5 MeV are reduced considerable at these higher energies. The simulations are discussed at the end of this chapter.

Table 6.1: *Sources used to test the basic polarimeter layer. The ^{12}N and ^{12}B sources were produced using the Van de Graaff facility of the IKF-Frankfurt. The experiments with the $^{106}Ru/Rh$ source were done at the KVI.*

source	decay	endpoint energy	half-life	production
^{106}Ru/Rh	β^-	3.54 MeV	1.020 year	-
^{12}B	β^-	13.4 MeV	20.3 ms	^{11}B(d,p) at 4.5 MeV
^{12}N	β^+	16.4 MeV	11.0 ms	^{10}B(^{3}He,n) at 3 MeV

6.1 What is tested: an introduction

The basic polarimeter layer consists of the $Nd_2Fe_{14}B$ magnet of section 5.5 sandwiched between four Silicon Strip Detectors (SSDs), two on either side of the magnet. The SSDs will be discussed in detail in the next section.

For test purposes a mono-energetic beam of fully polarized electrons with an energy between 10 and 100 MeV would have been ideal. However, such beams are not readily available. Instead of a mono-energetic beam part of a β-ray continuum from nuclear β-decay, preselected in energy by a Mini-Orange (MO) filter [53], was used [107]. However, convenient nuclear β-ray spectra do never extend to very high energies. In case of ^{106}Ru/Rh the energy is 3.54 MeV with a half-life of one year. There are continua with higher endpoint energies: 13.4 MeV in case of ^{12}B and 16.4 MeV in case of ^{12}N, but they have shorter half-lifes, 20.3 ms and 11.0 ms, respectively, and have to be produced on-line at a production-site. Nuclear β-rays do have two significant advantages: they are in essence fully longitudinally polarized with a degree of polarization given by $|P| = v/c$, and they are relatively easy to obtain. Table 6.1 gives an overview of the sources used for the experiments. The experiments with the ^{106}Ru/Rh source were performed at the KVI while those with the on-line produced ^{12}B and ^{12}N sources were done at the Institut für Kernphysik in Frankfurt (IKF-Frankfurt). As a consequence of using electrons, the prototype polarimeter is tested as a Møller polarimeter. No experiments with photons were done. The setup of the experiments is shown in figures 6.4 and 6.9 and will be discussed later on.

As already explained in chapter 1 the SSDs detect the Møller scattering events on the basis of the number of electrons which traverses them. The two SSDs between the source and the NdFe layer have to detect one particle while the two behind the layer have to detect the two Møller electrons emerging

from the NdFe target. An event with these characteristics will be labeled as 1122-event. The measurement of a scattering asymmetry requires the comparison of runs with opposite polarization of the scattering target electrons together with a normalization of the number of 1122-events in both cases. The opposite polarization is achieved by turning the NdFe layer upside down periodically. The normalization is done with the particles that traverse the NdFe layer without Møller scattering, so that before and after the NdFe layer only one particle crosses the SSDs. These normalization events are labeled as 1111-events. Details of the procedure are given in section 6.3.3.

6.2 The Silicon Strip Detectors

Only four years after the invention of the transistor in 1947 [108] it was already shown that a reversely biased p-n junction could serve as a charged particle detector when irradiated with α particles [109]. Later the junctions were also used for detecting electrons which are much less ionizing.

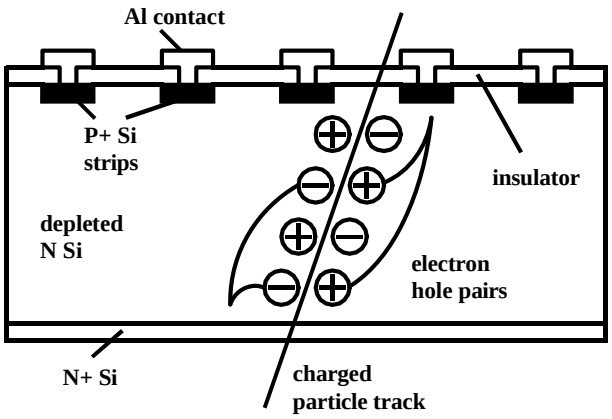

Figure 6.1: *Charged particle crossing a silicon strip detector.*

An SSD is a reverse biased p-n diode. The principle of an SSD will be explained with the help of figure 6.1. An ionizing charged particle traversing the diode creates electron-hole pairs in the depletion zone of the detector, the energy required to generate an electron-hole pair in silicon being approximately 3.6 eV. More than 99% of the created electrons and holes are contained within a cylinder along the beam path with a radius of 0.1 μm

Table 6.2: *Properties of the SSDs used in the polarimeter.*

material	<111> n-type silicon
resistivity	4 kΩcm
active area	48$\times$48 mm^2
thickness	400 μm
strip pitch	1.5 mm
number of strips	32
bias voltage	90-100 V, maximum 120 V
leakage current	typical 2 nA per strip at 100 V [111]

[110]. Under influence of the electric field the electrons and holes drift towards the n-side and the p-strip electrodes, respectively, giving a change in the induced surface charges. This leads to a short current pulse on the electrodes which is the input signal to the amplifiers connected to the electrodes. The amount of charge to be detected is $\approx$ 16 fC per μm silicon for a minimum ionizing electron with typical SSD thicknesses ranging from 250 to 400 μm. There is no signal amplification in the silicon detector layer. On their way to the electrodes, the charge clouds broaden by diffusion, the amount of broadening depending on the thickness of the detector. A discussion of this and other effects that limit the spatial resolution can be found in a review by Schwarz [110] on the use of SSDs in experiments with high energy colliders. A minimum ionizing electron will create around 40,000 electron-hole pairs while losing $\approx$120 keV of energy in a layer of 400 μm silicon.

6.2.1 SSDs used in the experiments

Table 6.2 summarizes the properties of the four SSDs used in the polarimeter [111]. The detectors were made at DIMES (Delft Institute of Microelectronics and Submicrotechnology)[112]. They have 32 strips of 1.5 mm, a low leakage current, <4 nA/cm^2, and a good homogeneity of the leakage over the strips. The detectors are operated at a bias voltage of 90 V to 100 V.

The performance of an SSD is largely determined by the electronics connected to the detector. Because the charge to be detected is only a few pC a low-noise preamplifier with a high gain is needed. The maximum count rate is not determined by the SSD charge collection time (5 to 10 ns) but by the

shaping time of this preamplifier (usually 1 to 5 μs).

The 128 silicon strips are read out using AMPLEX chips [113]. Such a chip contains 16 channels, each consisting of a charge amplifier, a shaping amplifier, a track-and-hold stage and a multiplexer stage. One silicon detector requires two AMPLEX chips and is mounted together with these chips and some peripheral electronics on one detector board. The detector boards were made in collaboration with E.M. Schooneveld at the Delft University of Technology (TUD) [111].

The AMPLEX chip is based on the so called 'continuous time filtering technique' [113], i.e. the current coming from the strip is permanently sensed and amplified. A track-and-hold circuit stores the output signal of the amplifier if a (properly timed) **external** hold signal is applied. As a consequence the detectors are **not self triggering**. Figure 6.2 shows the signal at the output of the shaper amplifier. The hold signal has to be applied at the maximum of this pulse to get the maximum signal. When a particle traverses a strip it takes $\approx$700 ns to reach this maximum in pulseheight. The total duration of the shaper output pulse is 4-5 μs. Figure 6.2 also shows the effect of an increased leakage current on the shape of the output signal. After the hold signal is applied the 16 parallel 'stored' signals per AMPLEX can be multiplexed to the output where they appear, one after another, as 16 positive DC voltage levels. For every external trigger, all the strips, including those that were not hit, are read out. The signals to control the AMPLEX chips are provided by an interface unit which will be discussed in the next section.

The SSDs are mounted in a disk-like housing box of 16 mm thickness. The walls of the box are made of 2 mm aluminium. Square holes of 60×60 mm^2 serve as entrance windows. To protect the silicon layers the entrance windows are covered with 12 μm thick mylar foils. Each housing contains besides peripheral electronics two silicon detectors with their strips perpendicular to each other. The distance between the silicon layers is 2 mm. They are centered around the middle of the box.

6.2.2 Data acquisition for the SSDs

The interface unit needed for the readout of the SSDs is a dedicated NIM module. The unit communicates with a LeCroy 4300B FERA charge analog to digital converter (ADC) in combination with a LeCroy 4302 FERA dual port memory module (MEM) which are used to convert and store the SSD

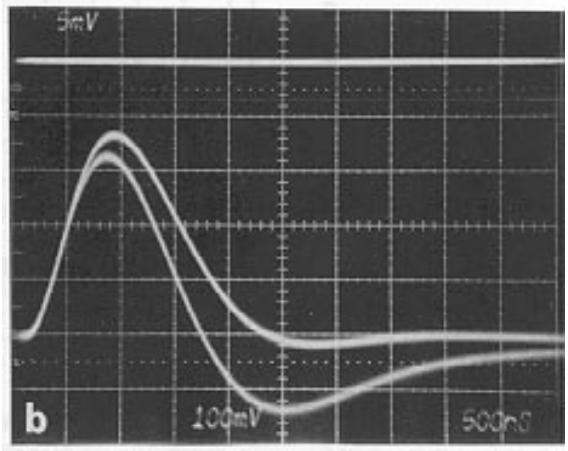

Figure 6.2: *Signals at the output of the shaper amplifier. The signals peak 700 ns after a current pulse at the amplifier input (a hardly visible small block pulse totally left). The upper trace is for* $I_{\mathrm{leak}} = 10$ *nA, the lower trace for* $I_{\mathrm{leak}} = 400$ *nA. The figure is taken from reference [113].*

data, respectively. The readout scheme is shown in figure 6.3. The NIM module has been made according to a design of E.M. Schooneveld at the Technical University of Delft [112].

After receiving an **external** trigger signal (A in figure 6.3), the control unit generates a track-and-hold signal (B). The time between the trigger-in and the track-and-hold signal-out can be adjusted from 100 ns to 1.5 μs, in view of the delay caused by the cables connecting the controller with the detector. Next, the unit generates a first clock pulse (C1) which multiplexes the first outputs of the eight AMPLEX chips to the common outputs (C2a). An 8-fold inverter/offset unit [112] turns the positive dc-levels into negative signals (C2b) so that they can be handled by the FERA charge ADC. The offset regulation was included to remove the relatively large offset in the dc-levels of the SSD signals. The offset regulation appeared to drift over a period of hours. This walk was taken into account during the data analysis (see section 6.3.3). The clock pulse is followed by an ADC gate (C3) with a setting of the width between 5 and 160 ns which allows the full use of the dynamic range of the ADC. The gate has an adjustable delay between 40 ns

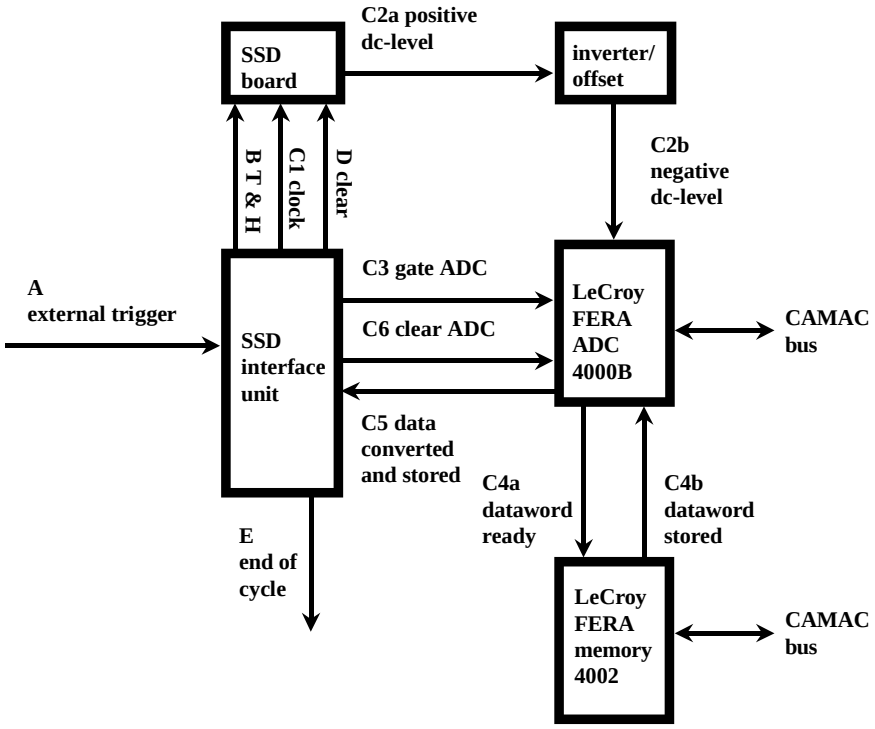

Figure 6.3: *Electronics setup for the readout of the SSDs.*

and 1 μs. After the gate, the eight analog input signals together with the eight free inputs of the ADC are converted to 16-bits digital words. They are, one after another, stored in the memory module via the ECL output of the ADC (C4a and C4b sixteen times). When the last word is stored, the ADC generates a 'pass signal' which is used as the 'data converted and stored' signal (C5) for the interface unit. It in turn generates a clear signal (C6) for the ADC. After sixteen cycles (C) the AMPLEX chips are cleared (D) and an end-of-cycle signal (E) is generated. Then the unit is ready for the next trigger. The end-of-cycle signal can be used to generate a look-at-me (LAM) signal in the CAMAC crate via one of the other CAMAC modules in the setup.

The readout scheme can be expanded to include more than 4 detector boards (8 AMPLEX chips) by using all the inputs of the ADC (maximum 8 boards) and by using more than one ADC if necessary. In the last case a LeCroy 4301 FERA driver is needed to control the storage of the digital

data from the different ADC's in the memory module. The 'data converted and stored' signal will then be the 'pass signal' from the last ADC read out.

The total readout cycle takes ≈230 μs per FERA ADC unit, not including the time needed for reading out the memory module.

6.3 Experiments with the ^{106}Ru/Rh source

6.3.1 Setup for the ^{106}Ru/Rh experiment

The setup used for the experiment with the ^{106}Ru/Rh source is shown in figure 6.4. The NdFe target was mounted in a 13 mm thick NE102 plastic scintillator (not shown) with a 40 mm diameter hole in it. This detector served as an active target-holder and was included in the setup to normalize the data of a run. The normalization allows a comparison between different runs (see section 6.3.4). It also served as an anti-coincidence detector for the main event trigger (see section 6.3.2). The scintillator was connected to a THORN EMI 9814B photomultiplier tube.

The distance between the second SSD as seen from the source and the NdFe foil was 20 mm and that between the NdFe foil and the third SSD 8 mm. An NE102 plastic scintillator detector was placed 1 cm behind the last SSD. It had a thickness of 13 mm and a diameter of 40 mm and was connected to an XP2020 Philips photomultiplier tube via a lightguide of 70 cm length and 45 mm diameter. The resolution of the plastic detectors was 13% at 1 MeV. The distance between the source and the NdFe target was 30 cm with the Mini Orange (MO) halfway in between them. The field in the central part of the MO gap was around 0.2 T. The MO transmitted the upper half of the ^{106}Ru/Rh spectrum. One-day measurements with this arrangement proceeded continuously during three weeks. The NdFe target was turned upside down in between these runs. To check upon the absence of instrumental asymmetries measurements were performed with a polarization insensitive Cu-foil.

6.3.2 Data acquisition for the ^{106}Ru/Rh experiment

The electronics to read out the plastic detectors and to define an event trigger is shown in figure 6.5 for the measurement with the ^{106}Ru/Rh source. The analog signals from the two plastic detectors are connected to the inputs

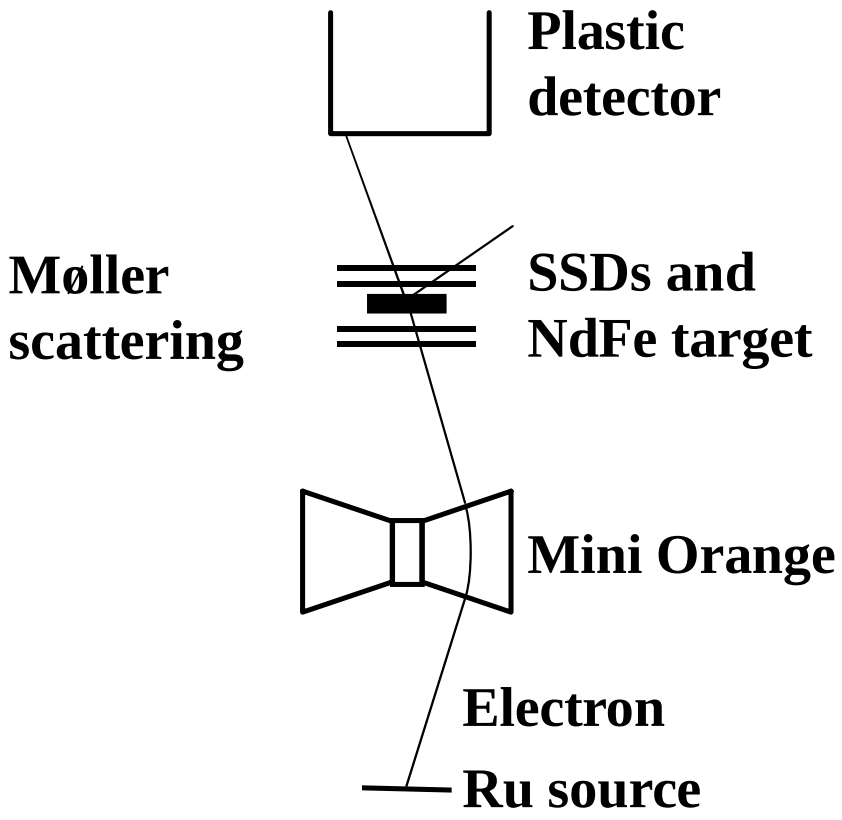

Figure 6.4: *Setup of the experiments with the $^{106}Ru/Rh$ source. The target detector is not shown in the figure.*

of two channels of an EG&G-ESN CF8000 constant fraction discriminator (CF). The logic output signals of the CFs are the inputs of a LeCroy 4508 programmable lookup unit (PLU) in continuous mode while the logic-OR of the signals is used to strobe the PLU. Two 'plastic event' triggers were defined by programming the PLU. Trigger I was defined as a hit in the plastic detector behind the polarimeter and no-hit in the plastic target holder. Trigger II was defined as a hit in the plastic target holder irrespective of the presence of a hit in the plastic detector behind the polarimeter. To get a countrate that could be handled by the standard CAMAC readout, triggers I and II were downscaled by a factor of 10 and 400, respectively, leading to a ratio of around 2:1 for trigger I and II events. In case of a downscaled trigger the

SSDs were read out followed by a readout of the CAMAC crate. In all other cases the PLU was cleared by hardware and made ready for the next plastic event.

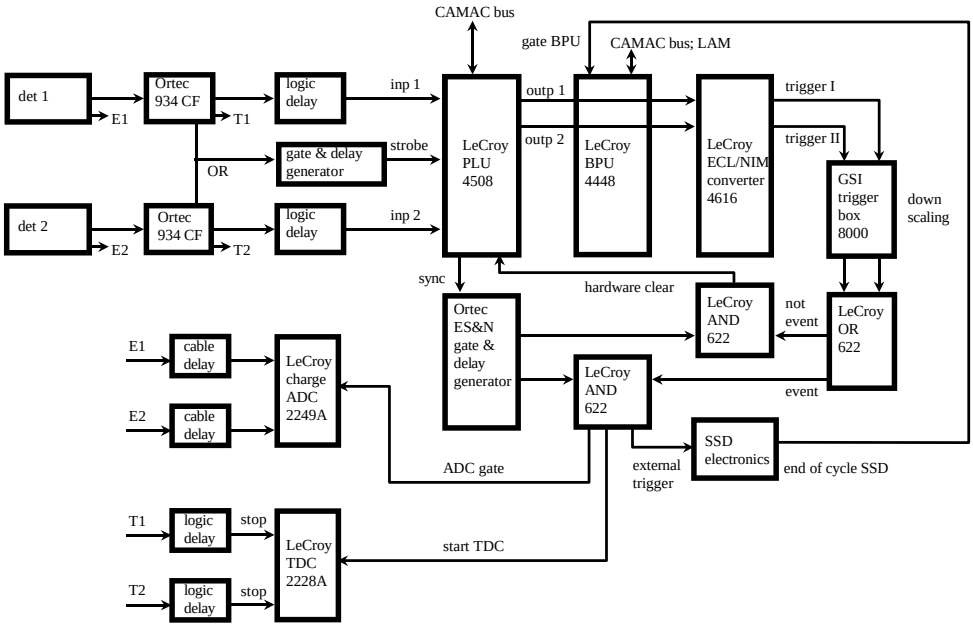

Figure 6.5: *Electronics setup used for the experiments with the* $^{106}Ru/Rh$ *source.*

The standard KVI data acquisition system was used to read out the CAMAC crate. It consisted of a modification of a standard ELN-PASCAL program [114] running on a rtVAX. The data were, via an ethernet connection, written to DAT-tape in PAX format [115] at a rate of around 40 Hz. The data flow was monitored with a small FORTRAN code which created a global section in computer memory and used HBOOK routines [116] to create and fill the histograms in this section. The CERN Physics Analysis Workstation package (PAW) [117] was used to inspect the histograms.

6.3.3 Data analysis: procedure

During data analysis events are classified into groups according to their track multiplicities in the four SSD-layers. The track multiplicity for one SSD is defined as the number of strips firing (as defined below) minus the number

of neighbour-strips firing. For example, when three neighboring strips fire the track multiplicity is $3 - 2 = 1$. In general, it is assumed that the firing of neighboring strips results from one particle traversing the SSD. The track multiplicity is determined for each of the four SSDs. The events are classified according to their track multiplicity in the four SSDs. To give an example: a '1122 event' has track multiplicity 1 for the first and second SSD layer and 2 for the third and fourth layer. For each event class the energy deposited in the plastic detectors is stored in a separate histogram.

The above analysis proceeds in two steps. In the first step 'raw' energy spectra are constructed for each individual silicon strip and for both plastic detectors. At the same time the strip data are corrected for walk in the inverter/offset unit by monitoring the position of the offset-peak figure (6.6a) in the strip spectra. Because each time all the strips are read out while only a few contain a particle signal, the number of 'offset-events' outnumber the number of 'particle-events' per strip; $\approx 10^2$ times for central strips and $\approx 10^3$ times for peripheral ones. By taking the average of the first 1000 events of a run, disregarding the under- and overflow events, i.e. events outside the dynamic range of the ADC, the position (X) and width (σ) of the offset-peak at the beginning of the run is determined. The error due to taking into account particle-events instead of offset-events in determining this start position is negligible because the particle-event contribution to these 1000 events is below 1%. After this initialization an event in the interval $[X - 4 * \sigma, X + 4 * \sigma]$ is considered as an offset-event and it is used together with the previous 999 offset-events to determine the new value for X and σ. In this way the last 1000 offset-events are used to calculate X and σ for the next event. The width of the interval was not very critical as long as it was not below $2*\sigma$ or above $6*\sigma$. The dynamical X value is used to correct the spectra for inverter/offset walk by shifting the spectra such that the offset-peak is at the same position during the whole run. An example of a raw- and walk-corrected spectrum is shown in figures 6.6a and b, respectively. The timescale of the walk (hours) is much larger than the time it takes to collect 1000 offset-events (seconds) making the described correction procedure possible.

Before going to the second step in the data analysis the offset-corrected spectra are calibrated to make an inter strip comparison possible. The raw plastic spectra are also calibrated to allow for a comparison between different runs. None of the calibrations is absolute i.e., no attempt is made to set the energy scales. For the offset-corrected spectra a fit is made to the offset-peak and the particle-peak. This is done by using the fit routines in PAW.

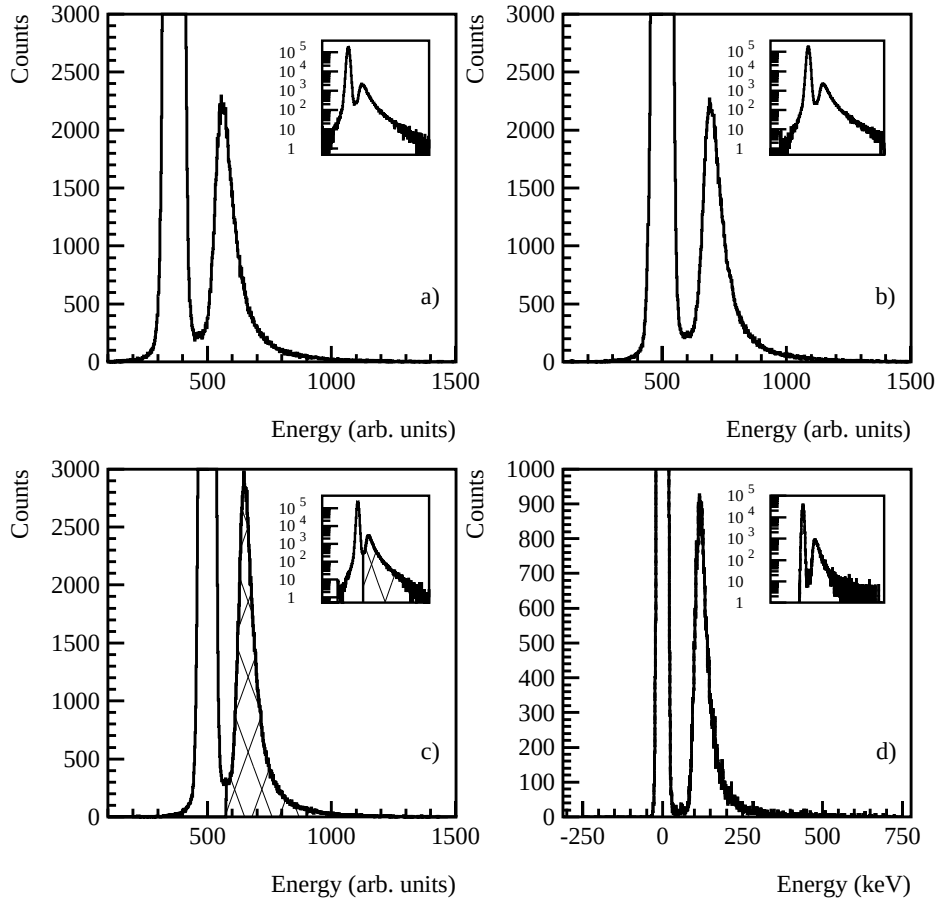

Figure 6.6: *Silicon strip data: a) raw spectrum, b) walk-corrected spectrum, c) calibrated spectrum and d) simulated spectrum (see section 6.4.2). In each picture the large peak on the left is the offset-peak. It is followed on the right by a smaller particle-peak. If the energy falls in the hatched region (from channel 575 to channel 2000, in figure c) the strip has fired. The spectra are for a central strip of the first SSD as seen from the* $^{106}Ru/Rh$ *source. Insets present the same data on a log-scale.*

Although the particle-peak follows a Landau distribution the maximum can be found in a satisfactory way by fitting a Gaussian to the data if the fit interval is chosen not too wide. Thus to both peaks a Gaussian is fitted in an interval around the peak maximum. The two peak positions are used

to calibrate the 128 strip spectra. The particle-peak is chosen at the same position for each strip. Thus, the change in dE/dx when the particle traverses the detector is not expressed in the position of the particle-peak anymore.

The plastic spectra are calibrated in a different way. A Gaussian fit to the pedestal, i.e. the zero point of the ADC, gives one point while the endpoint of the spectrum gives the second point needed for the calibration. The endpoint of a spectrum is defined as the point for which the area under the spectrum starting above the pedestal up till the endpoint contains 99% of the total area under the spectrum (including overflows).

With the calibration parameters as input in the second step of the analysis, the different event types are sorted and the calibrated histograms are produced.

A strip is considered to fire if the signal falls in the hatched region shown in figure 6.6c. The point where the region starts is located at the same position in all calibrated strip spectra. The hatched region includes signals from both single and multiple particles traversing the strip. The hatched area is not subdivided into areas belonging to single and multiple electrons traversing the strip because there is no clear evidence for two or multiple particle-peaks in the spectra. If they are present they are not distinguishable from the high energy tail of the single particle-peak.

6.3.4 Results for the ^{106}Ru/Rh experiment

Figure 6.7 shows energy spectra for the plastic detector behind the polarimeter for three track multiplicity combinations: a) without track multiplicity selection, b) with track multiplicity 1111 and c) with track multiplicity 1122. The data for these spectra have been accumulated in approximately one day, using the β^--rays from the ^{106}Ru/Rh-source. The bump to the right of the low energy peak in the spectrum is due to the presence of the Mini Orange (MO) in the setup. Without a MO no such bump would be visible. The effect of the MO is seen even better in the figure b where the SSDs are used to remove the low energy peak by selecting 1111-events. The low energy peak itself shows up when track multiplicity 0000 is selected (spectrum not shown here) and is probably caused by γ rays from the source or by bremsstrahlung. The 1122-events in figure c are due to events with two tracks behind the NdFe target. Among them are the Møller scattering events in the NdFe target which determine the polarization sensitivity. However, besides these events of interest all possible other scattering events leading to the detection

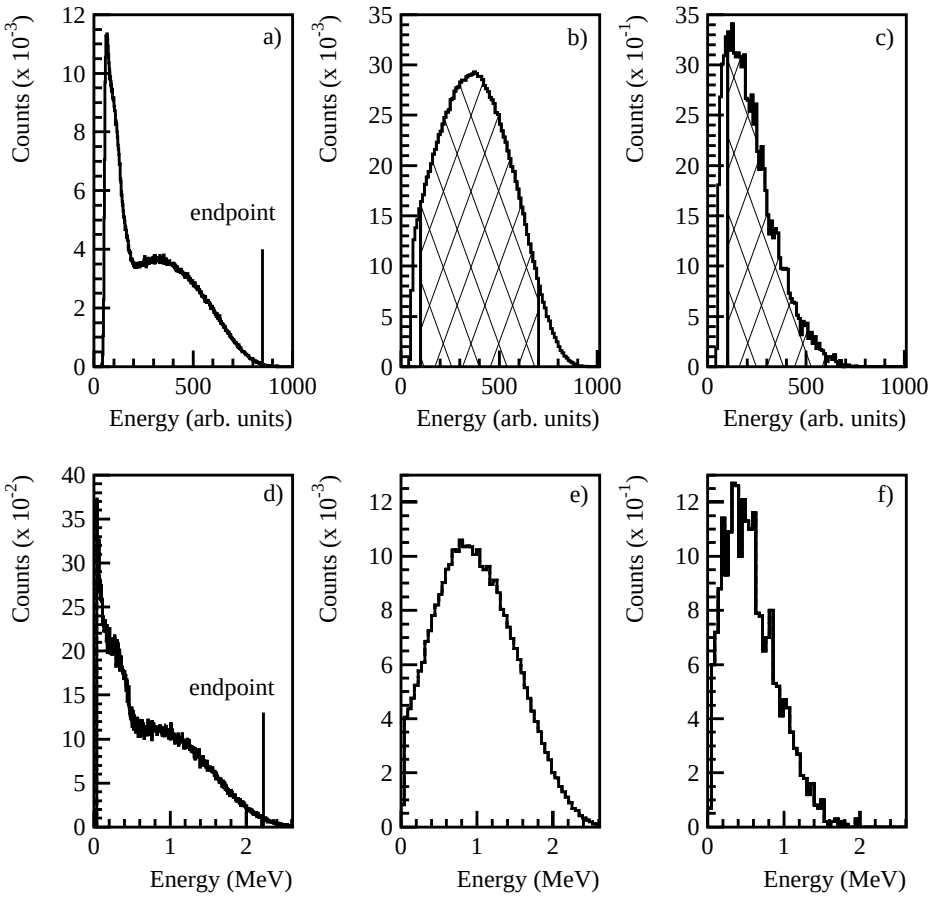

Figure 6.7: *Calibrated energy spectra for the plastic detector behind the polarimeter layer a) without track multiplicity selection, b) with track multiplicity 1111 and c) track multiplicity 1122. The figure d), e) and f) show similar spectra resulting from a Monte Carlo simulation of the experiment (see section 6.4.2). The hatched areas from channel 100 to channel 700 in the figures b and c are used to normalize the number of 1122-events as is explained in the text. The spectra are the result of a single run.*

of a second electron behind the target and random 1122-events are contributing to this spectrum. The size of this polarization insensitive background is estimated in section 6.4.2 where a Monte Carlo simulation of the experiment is discussed.

To be able to compare the number of 1122-events in runs with different orientations of the NdFe magnet the data must be normalized. This normalization must be **insensitive** to the orientation of the magnet and **sensitive** to every non-polarization-dependent effect which influences the countrate of 1122-events. These non-polarization-dependent effects include for example drifting of the SSDs or variations in computer deadtime. Originally, the target detector and trigger II were included in the setup for normalization purposes. However, this normalization was abandoned when it appeared that the effect of the magnetic field of the NdFe magnet on the spectrum of this detector was considerable. A second drawback is that the trigger II is not sensitive to possible changes in the detection efficiencies of the SSDs behind the NdFe target and the plastic scintillator detector behind the SSDs. Such a change in trigger efficiency might influence the 1122-event countrate.

As an alternative the 1111-events have been used to normalize the data. However, 1111-events are partly polarization sensitive themselves: These events result from electrons which pass the NdFe layer without generating a SSD **detectable** secondary electron. Møller scattering events of which the second electron was either not detected in both SSDs or stopped in the target cause such events. This can happen for example when the incident electron transfers little energy to the target electron. The polarization asymmetry for such energy asymmetric scattering events is much lower than for symmetric scattering events (figure 3.2) However, the cross section is much higher, making the overall effect not directly clear[1]. In appendix B the macroscopic cross section for Møller scattering is used to calculate the percentage of electrons which cross the NdFe target without having a Møller interaction in which the target electron obtains more than 100 keV kinetic energy. This is the case for 79% of the electrons which enter the target with 3 MeV kinetic energy and even more for electrons which enter with less energy. Part of these 79% electrons might still have a Møller interaction in which the target electron obtains less than 100 keV and contribute to the scattering asymmetry. The overall scattering asymmetry for 1111-events is estimated below where the Monte Carlo simulation of the experiment is discussed.

The number of normalized 1122-events is calculated by summation of the number of 1122-events between the gates given in figure 6.7c divided by the number 1111-events between similar gates in figure 6.7b. The use of an

[1]In the polarimeter described in the thesis of Wichers [35, 36] these events contributed to the sensitivity of the apparatus.

interval instead of the full spectrum content makes the division less sensitive to the cutoffs of the spectra at the low and high energy side. The statistical counting error is used as the error on the summed numbers. Figure 6.8a shows the normalized 1122-events for the runs with the NdFe target. The convention is such that for an up-run the magnetic polarization vector is pointing away from the ^{106}Ru/Rh source. Because β^--rays have helicity -1 (spin opposite to the momentum) and the magnetic polarization vector is opposite to the target spin direction, the Møller asymmetry should lead to a higher down- than up-countrate. The horizontal line fit to the up- and down-group of runs is shown in the figures. The fits give equal up- and down-countrates within the statistical errors i.e., **no Møller scattering asymmetry is observed** in the experiments with the ^{106}Ru/Rh source.

The results of an analogous analysis of four runs with a Cu-foil of 0.5 mm are shown in figure 6.8b. Because the Cu-foil and NdFe-foil have different properties, the number of normalized 1122-events are not exactly equal. As expected for Cu, no asymmetry is found. This absence of asymmetry shows that the calibration plus normalization procedure is sufficiently precise to allow a comparison of runs separated by several days from each other.

The absence of an asymmetry in the measurements with the NdFe target could be caused by the polarization insensitive background in the number of 1122-events. However, there is no obvious way to make an estimate of this background from the experiments discussed so far. A measurement without a foil resulted after analysis in 5.31 ± 0.06 normalized 1122-events. A comparison between results with and without a foil is not straightforward because the NdFe-layer also stops low energetic electrons which crossed the first two SSDs. When no foil is present, these low energetic electrons could contribute to the number of 1122-events.

The overlap between the measurement without a foil and the results from the Cu-measurements must be accidental. In order to obtain a better insight in the various interaction mechanisms and background effects a Monte Carlo simulation of the polarimeter layer has been performed as described in the next section.

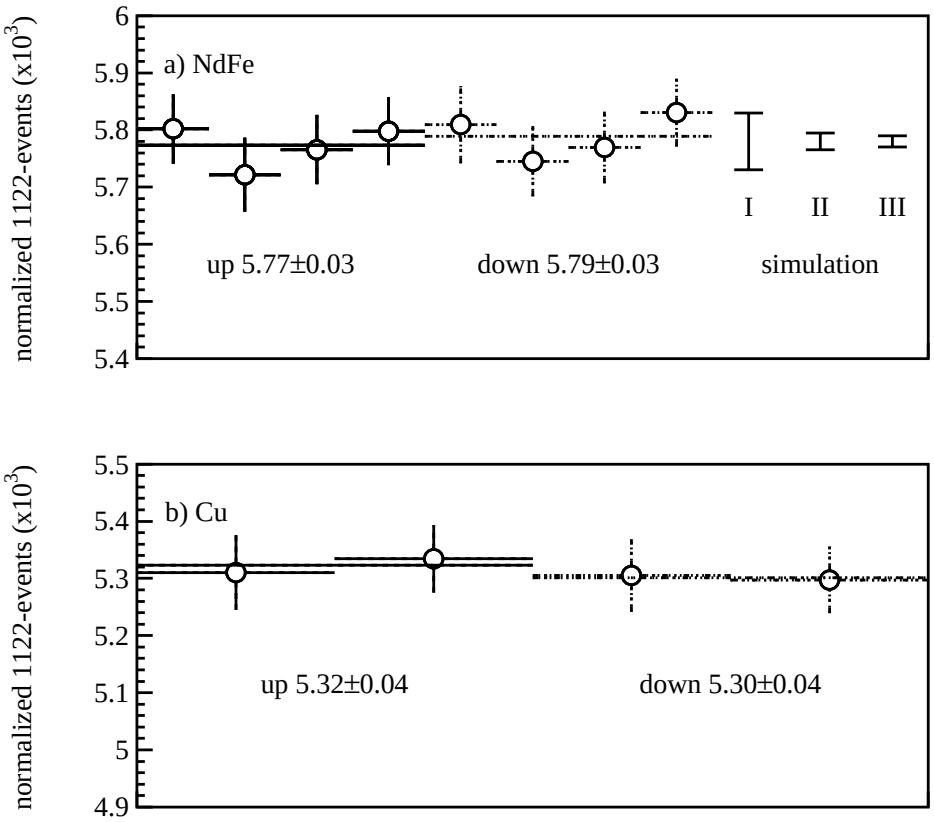

Figure 6.8: *Normalized 1122-events for runs with a) a NdFe target and b) a Cu target. Each point represents a run. Bar III in figure a is the expected difference in normalized 1122-events for up- and down-runs on the basis of a simulation of the experiment (see section 6.4.2). Bar I and II are also results from the simulation. Their meaning is explained in section 6.4.2. The lines are results of horizontal line fits to the data points.*

6.4 Simulation of the ^{106}Ru/Rh experiment

6.4.1 Monte Carlo data

The extended version of GEANT discussed in chapter 4 was used to simulate the ^{106}Ru/Rh experiment. All relevant parts of the geometry of the setup

were included in the simulation. The 'Monte Carlo ^{106}Ru/Rh source' consisted for 79% of a β-spectrum with an endpoint energy of 3.54 MeV, for 11% of a β-spectrum with an endpoint energy of 3.03 MeV in combination with a γ-ray of 512 keV and for 10% of a β-spectrum with an endpoint energy of 2.41 MeV with γ-rays of 512 keV and 622 keV. The magnetic field in one gap of the MO was mapped and served as a model for the simulated field. The magnetic field of the NdFe target layer was not included in the simulation.

Monte Carlo data were generated by tracking particles through the setup. The data were written to tape with the same event structure and trigger conditions as the data of the experiments. The additional information concerning the type of process taking place and the associated polarization asymmetry where stored along with the data. The energy lost in the plastic detectors was smeared with a Gaussian distributed random number to account for the resolution of these detectors (13% at 1 MeV). To the 'energy signals' of the strips an offset-peak was added to simulate the offset-peak in the measured data.

To increase the statistics of the simulated data the input spectrum was cut into two pieces for separate simulation. A high-energy part with the particles having the highest probability to create an event trigger I, and a remaining part containing the low-energy particles of the spectrum. Afterwards the two parts were added to each other with the appropriate weighting factors. In this way not all the low-energy particles (which are mostly stopped without creating a trigger I) are simulated explicitly.

6.4.2 Results of the simulation

The Monte Carlo data were analyzed in the same way as the real data. Figure 6.6d shows the spectrum of one of the strip detectors. The comparison with the real data makes clear that the offset- and particle-peak are better separated in the simulation. The simulated spectra for the plastic detector behind the polarimeter are shown in figure 6.7d-f. The number of particles in the low-energy peak is underestimated and the number of particles in the high-energy tail is overestimated. The simulation gives $(6.1 \pm 0.1) \cdot 10^{-3}$ normalized 1122-events which is somewhat more than the measured value of $(5.78 \pm 0.02) \cdot 10^{-3}$. However this is not surprising considering the above mentioned differences between the measured and simulated spectra. The calibration procedure as presented in section 6.3.3 was used to scale the energy axis of the simulated spectra to the x-axis of the measured spectra.

Table 6.3: *Scattering asymmetry and percentage of misidentified 1122- and 1111-events. The numbers result from a Monte Carlo simulation of the $^{106}Ru/Rh$ experiment. A target polarization of 100% is assumed.*

event class		scattering asymmetry	contribution to event class
1122	total	-0.08	100%
	single Møller	-0.27	24%
	target related	-0.23	34%
1111	total	-0.03	100%
	single Møller	-0.15	18%
	target related	-0.13	27%

This provides an indirect energy calibration for the measured spectra. The differences between the simulated and measured spectra are probably due to an inexact simulation of the MO field: The transmission of the MO was smoothed by modeling its field on the basis of a crude field mapping. The small MO dimensions did not allow an accurate mapping.

The extra information stored with each simulated event provides the scattering asymmetry of the polarimeter and the percentage of misidentified events. The results are summarized in table 6.3

The overall scattering asymmetry for 1122-events is $A = -0.08$. Only 24% of the total number of 1122-events result from single Møller scattering in the NdFe target. The scattering asymmetry for those single Møller 1122-events is -0.27. Of the events identified as 1122-events 34% interacted in the target while the remaining 1122-events where not related to the NdFe target. The asymmetry of these 34% NdFe target related events is -0.23. Thus the effect of background not related to the NdFe target is considerable. Assuming an NdFe target polarization of 3.7%, a polarization of 100% for the β-decay electrons and $5.78 \cdot 10^{-3}$ normalized 1122-events for an unpolarized target, the difference in the number of normalized 1122-events for up- and down-runs is reduced from $2 \times 0.23 \times 0.037 \times 5.78 \cdot 10^{-3} = 0.10 \times 10^{-3}$ for target related events to $0.03 \cdot 10^{-3}$ when the events not related to the target are included. This large reduction of the effect is illustrated in figure 6.8 by the bars I and II.

The effect is even further reduced when the scattering asymmetry of the

1111-events used for the normalization is considered. The overall scattering asymmetry for 1111-events is $A_n = -0.03$. About 18% of these events are due to a single Møller scattering in the NdFe target. These single Møller 1111-events have a scattering asymmetry of -0.15. Around 27% of the 1111-events interacted in the NdFe-target resulting in an asymmetry of -0.13.

Assuming the same numbers as above the expected difference in normalized 1122-events for the measurement is

$$\frac{2|A - A_n|}{1 - A_n^2} \times 0.037 \times 5.78 \cdot 10^{-3} = 0.02 \cdot 10^{-3}. \tag{6.1}$$

Bar III in figure 6.8 shows the expected effect: it happens to be exactly equal to the separation measured in the experiments. However, the statistical error on the up- and down-values does not allow the conclusion that a scattering asymmetry is observed.

It should be kept in mind that the simulations depend on the settings of the cutoffs: The tracking of electrons and photons was stopped when the kinetic energy was below 10 keV. Below 100 keV bremsstrahlung and δ-ray production were treated as continuous processes i.e., no electrons and photons were generated below 100 keV. The last cutoff influences in particular the number of events with one Møller interaction in the NdFe target. The influence on the overall scattering asymmetry is less since electrons with energies below 100 keV have only a negligible chance to escape from the 0.5 mm NdFe target and to give a signal in both SSDs behind the target.

From the simulations it can be concluded that the contribution of polarization insensitive processes to the events identified as 1122-events reduces the scattering asymmetry below the detection limit of the polarimeter for electrons with energies below 3.5 MeV. Therefore, the proposed polarimeter is not suited for these low energies. The next section focuses on the performance of the polarimeter at energies above 5 MeV.

6.5 Experiments with the ^{12}N and ^{12}B sources

6.5.1 Setup for the ^{12}N and ^{12}B experiments

Figure 6.9 shows the setup used for the experiments with the ^{12}B and ^{12}N sources which is in principle similar to the setup used for the ^{106}Ru/Rh source. A block of nine phoswich detectors [118] was mounted behind the last SSD

at a distance of 12 cm. Each phoswich detector consists of a 1 mm thick NE102 plastic layer functioning as a ΔE detector heatpressed on 50 mm thick NE115 plastic for full energy (E) information if the electrons are stopped in this part of the detector. The signal from such a phoswich detector has a fast and a slow component coming from the NE102 and NE115, respectively. By splitting this signal into two and feeding each signal into a separate charge-to-digital converter with different integrating times the two components can be disentangled. The detectors were originally used in heavy ion experiments to identify light-charged-particles on the basis of ΔE vs E information. For the present experiment the phoswiches served to discriminate electrons from the photon background. The detectors have a surface area of 6.4×6.4 cm^2. The Mini Orange (MO) used in the setup was constructed of exceptionally strong magnets reaching magnetic fields of up to 0.4 T in the central parts of the MO-gaps. The MO selects the upper half of the β-ray spectrum. It was placed halfway between the production-target and the NdFe target, the distance between the two targets, boron and NdFe, being 26 cm. In order to invert the target polarization the NdFe target was mounted in a holder that could be turned upside down from outside the vacuum vessel which contained the setup. Furthermore, the target could be rotated around its normal to average over the remaining inhomogenities in the target thickness. The distance between the NdFe layer and the first SSD on either side was 2 cm.

For the production of the ^{12}N and ^{12}B sources the 7.5 MeV Van de Graaff machine of the IKF-Frankfurt was used. For the measurements two weeks of beamtime were made available. The layout of the beamline around the site of the setup is shown in figure 6.10. The Van de Graaff machine delivers a DC beam. The beamdump was located approximately one meter behind the setup.

During the first week the ^{10}B(^{3}He,n)^{12}N reaction [119, 120] was employed with a ^{3}He beam of 3 MeV. However, the experiment encountered several difficulties. In the beginning the protons from the competing (^{3}He,p) reaction channel were causing problems. These protons were able to penetrate the MO filter and gave rise to large signals in the first SSD. Furthermore, unexpected problems in the electronic system of the SSDs arose due to the 40 m separation between the detector boards and the interface electronics. Finally, during the last two days in the weekend, the Van de Graaff ran out of ^{3}He-gas. As a consequence almost no data could be taken. During the second week most of the problems were solved. This time the ^{11}B(d,p)^{12}B

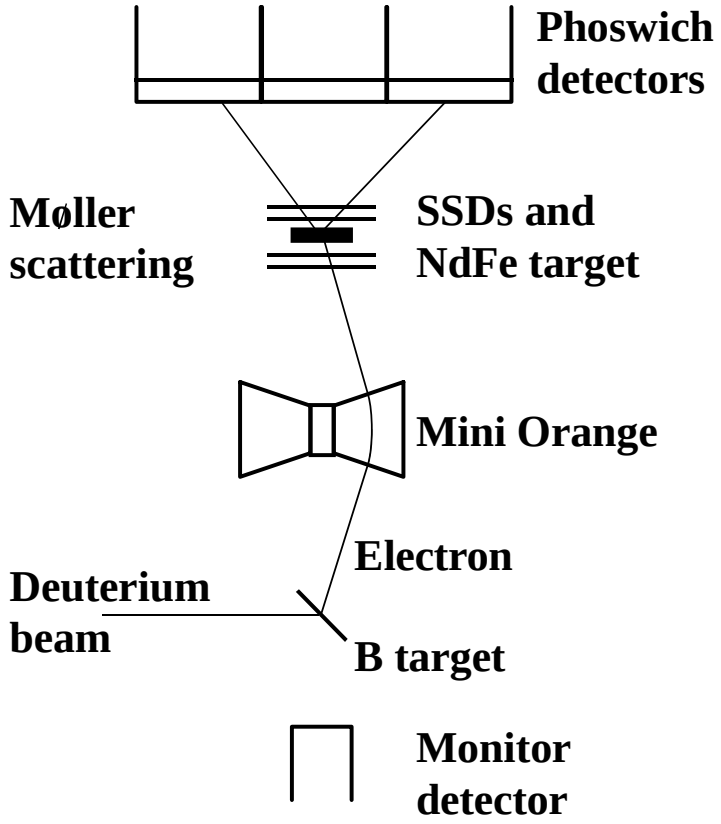

Figure 6.9: *Setup of the experiments with the on-line produced sources.*

[119, 120] reaction with a beam energy of 4.5 MeV was employed because the cross section for this reaction is considerably higher ($\approx 250\times$) than for the reaction leading to ^{12}N making the source-production easier. Part of the time a beamkicker was used to produce a pulsed beam. The measurement was done while the beam was deflected away. The beamkicker had to be installed just in front of the setup because this was the only available location. Deflecting the beam therefore led to a large radiation background.

6.5.2 Data acquisition for the ^{12}N and ^{12}B experiments

The data acquisition setup for the experiments with the ^{12}N and ^{12}B sources was similar to the one discussed in section 6.3.2 except that the number of

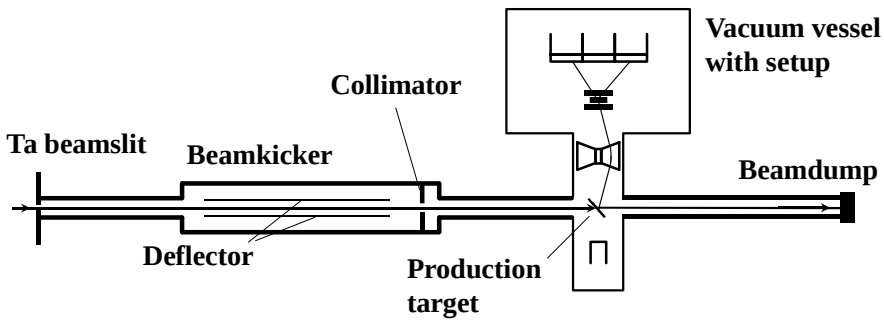

Figure 6.10: *Layout of the beamline around the location of the experiment at the IKF-Frankfurt. Some local shielding (not shown) was placed around the beamslit, collimator and beamdump.*

detectors was increased from two to ten. Furthermore, each phoswich detector needed two separate ADC channels to disentangle the fast and slow signal from the detector. The triggers defined by programming the PLU were: i) exclusive coincidences in the phoswiches; no downscaling, ii) exclusive singles in the phoswiches; downscaling 2^{12} and iii) monitor detector; downscaling 2^{16} before the PLU and 2^2 after the PLU.

The rtVAX which handled the data acquisition from the CAMAC crate, was included in the computer network of the IKF-Frankfurt.

6.5.3 Results for the ^{12}N and ^{12}B experiments

Applying the data analysis scheme outlined in section 6.3.3 to the data taken in Frankfurt was not without difficulty. The signals from the strips resulted in spectra in which the particle-peak and the offset-peak are hard to separate as can be seen in figure 6.11. This effect can be explained as follows: Part of the trigger events from the phoswich detectors must have been random events due to the background of photons and neutrons connected with the production of the sources, beamslits, beamdump, etc. Therefore, the sampling of the signals from the SSDs (figure 6.2) occurred at a random moment. Combined with the high intensity of electrons incident on the SSDs this resulted in the spectrum shape shown in figure 6.11. Furthermore, a high intensity of particles on the SSDs causes an increased leakage current in these detectors which influences the signal at the output of the shaper amplifier in the way shown in figure 6.2.

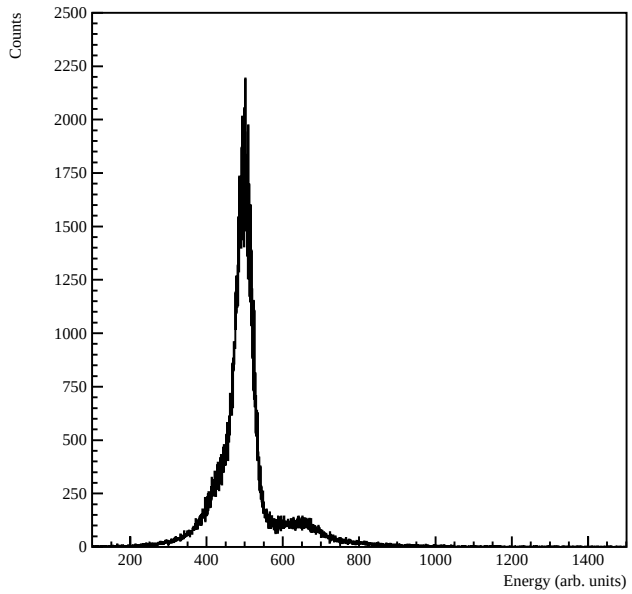

Figure 6.11: *Energy spectrum of one strip for the experiment with the online produced* ^{12}B *source.*

Both the pulsed- and DC-beam experiments suffered from these background effects. The background problems were underestimated during the planning of the experiment and the available beamtime was too short to overcome them. A pulsed beam with the beamkicker installed at a position in the beam guiding system far away from the experimental setup, might have prevented these problems. However, such a layout was not available during the tests with the polarimeter layer.

Due to the noise in the data a scattering asymmetry could not be extracted from them. Also no simulation of the experiments was performed. Instead, the response of the detector layer was extracted from a simulation with mono-energetic electrons and photons with energies above 10 MeV.

6.6 Simulations of the polarimeter above 10 MeV

The setup for the 'high energy' simulations consisted of an NdFe target of 1 mm with SSDs on both sides at 2 cm distance and with a $10 \times 10 \times 12.5$ cm^3 plastic detector as trigger detector 1 cm behind the SSDs. The setup did not include a target detector and a Mini Orange. Simulations were performed for beams of mono-energetic electrons and photons from 10 to 90 MeV in steps of 20 MeV. At each energy 100000 particles were tracked through the polarimeter. The diameter of the beamspot on the polarimeter was 1 cm and focused in the center of the first SSD. The scattering events were classified according to their event class in the same way as before.

Figure 6.12a shows the scattering asymmetry resulting from the simulation for 1111- and 1122-events for initially fully longitudinally polarized electrons with an estimated error in the scattering asymmetry of 0.05 at all energies. The percentage of events detected as 1122-events varied between 0.8% and 1.7% with increasing electron energy while the percentage of 1111-events lie in the range from 83% to 94%. Around 98% of all 1122-events was related to one or more interaction(s) in the NdFe-target with an asymmetry close to the asymmetry shown in figure 6.12a. Thus, at these energies the non-target related background is considerably reduced compared to the simulation with the ^{106}Ru/Rh-source at lower energies. This is partly due to the increased target thickness, 1 mm instead of 0.5 mm with the same SSD-thickness, and partly as a result of the increased electron energy which reduces the straggling of the electrons.

Figure 6.12a allows the conclusion that the 1111-events can be used for normalization purposes because their scattering asymmetry is negligible.

The scattering asymmetry of the polarimeter for initially fully circularly polarized photons is based on detecting Compton events. They appear as 0011-events with an asymmetry as shown in figure 6.12b. The percentage of 0011-events varies from 1.2% to 1.9% for the energies between 10 and 90 MeV. The non NdFe target related background to these events varies from 9% to 16%. The target related 0011-events have a scattering asymmetry close to the asymmetry shown in figure 6.12b.

The figure of merit (FOM) as defined in equation 2.4 of the polarimeter is shown in figure 6.13. A NdFe target polarization of 3.7% is assumed. The error bars are based on statistical counting errors for the number of detected

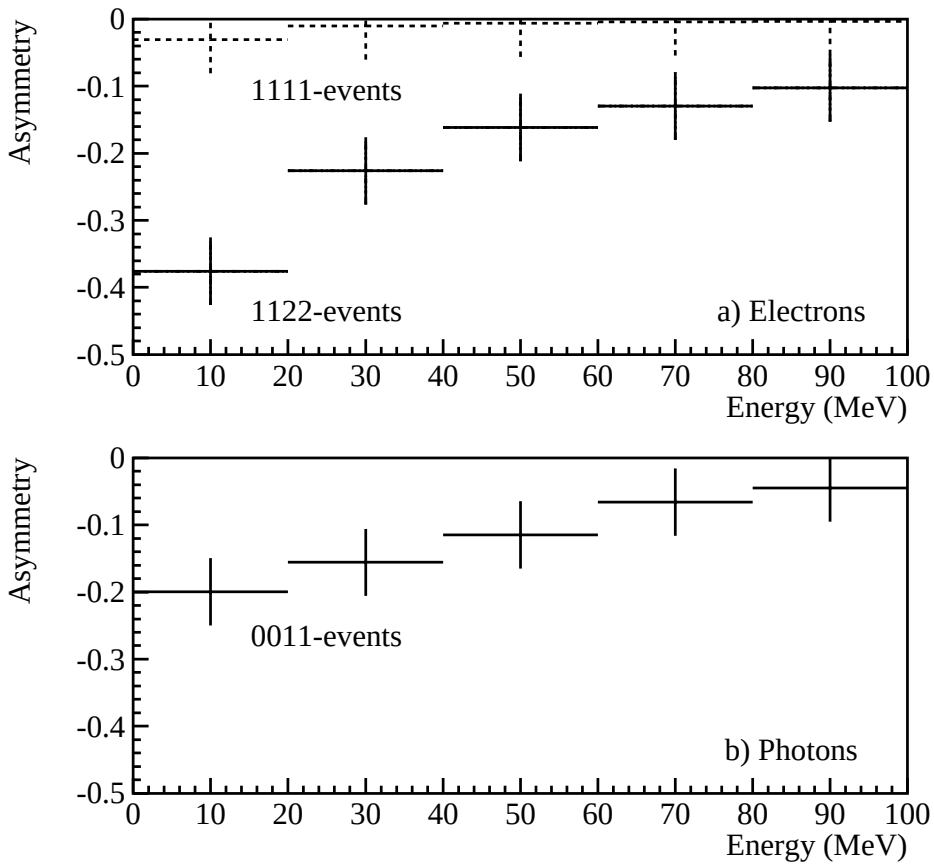

Figure 6.12: *Scattering asymmetry for the polarimeter layer resulting from a simulation with a) fully longitudinally polarized electrons and b) fully circularly polarized photons. A target polarization of 100% is assumed. The horizontal errorbars have no meaning.*

events, on an error of ± 0.05 in the asymmetry and on a 5% error in the estimated target polarization.

The depolarization of the particles after passing through the polarimeter is below 10%. This allows it to put several layers behind each other to increase the detector efficiency. The FOM values of 10^{-6} to 10^{-7} could then be increased to around 10^{-5}. With such a FOM the polarimeter will become a tool to basic studies in physics. The simulations demonstrate that the polarimeter concept is valuable when the incident particles have more than

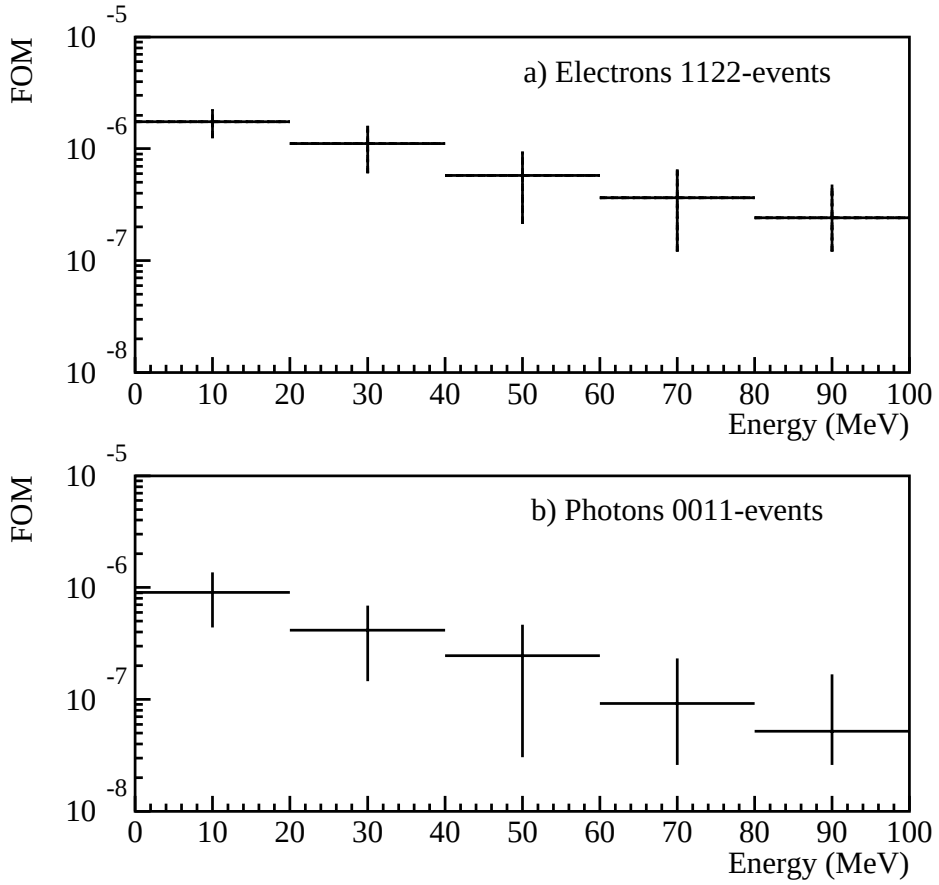

Figure 6.13: *Figure of merit for the polarimeter layer resulting from a simulation with a) fully longitudinally polarized electrons and b) fully circularly polarized photons. A NdFe target polarization of 3.7% is assumed. The horizontal errorbars have no meaning.*

10 MeV energy. Further experiments are desirable and justified on the bases of these simulations.

6.7 Summary of the results

The experiments with the ^{106}Ru/Rh source do not allow the conclusion that a scattering asymmetry is observed. The experimental result is not statis-

tical significant. The GEANT simulation of the experiment reproduces the observed effect and gives an explanation for the lack of asymmetry: A background of scattering processes not related to the NdFe target contributes considerable to the 1122-events. This background effect reduces the sensitivity of the polarimeter layer. The overall conclusion from the experiments with the ^{106}Ru/Rh source is that the layer can not be used as a polarimeter for electrons with energies below 3.5 MeV.

The experiments at energies above 10 MeV with positrons from a ^{12}N source and electrons from a ^{12}B source encountered several experimental difficulties. The production of the sources with a Van de Graaff accelerator was accompanied by a large radiation background which introduced too much noise in the data to allow an extraction of a scattering asymmetry.

A Monte Carlo simulation of the polarimeter with polarized electrons and photons with energies from 10 MeV to 90 MeV shows that the polarimeter concept is worth considering at these energies. The figure of merit for a single NdFe layer (target polarization 3.7%) sandwiched between four SSDs is 10^{-6} to 10^{-7} for both electrons and photons.

Chapter 7

Conclusions and outlook

In this last chapter the main conclusions from this thesis are summarized and the objectives as stated in the first chapter are reconsidered. The discussion is divided into conclusions regarding the $Nd_2Fe_{14}B$ target, the polarimeter concept, and recommendations for future experiments.

7.1 The $Nd_2Fe_{14}B$ target

The proposal of using $Nd_2Fe_{14}B$ (NdFe) as carrier of polarized target electrons is central to the polarimeter under consideration. One of the objectives was to test this material on its merits with respect to polarization sensitivity. In chapter 5 the polarization for rare earth $R_2Fe_{14}B$ magnets was estimated on the basis of a model that took into consideration the magnetic moments of the ions in the magnet and their coupling. The resulting 3.7% target polarization for the magnet used in the polarimeter is low compared to the percentage of target polarization possible with soft magnetic materials. It is also less than the 4 to 5% that were expected on the basis of single crystal values at the start of the project. Unfortunately, the actual structure of bulk material reduces the electron polarization to 3.7%. For future experiments a careful selection of the magnets, with a remanence magnetization as close as possible to 1.6 T, is of primary importance to improve as much as feasible on this percentage. $Pr_2Fe_{14}B$ magnets deserve full attention when its metallurgy can be refined to produce bulk material of sufficient quality.

Chapter 6 describes the test of the basic polarimeter layer with β^--rays for the purpose of measuring the target polarization and demonstrating the

polarization sensitivity of the layer. In experiments with a ^{106}Ru/Rh source no scattering asymmetry was found. Later Monte Carlo simulations, adapted to include polarization phenomena, showed that the background of non-polarization sensitive scattering processes made an observation of the scattering asymmetry practically impossible at these low β-ray energies. Consequently, the target polarization could not be deduced from the measurements.

7.2 The polarimeter concept

The polarimeter concept is based on three main ingredients: 1) The use of permanent magnets magnetized perpendicular to their surface to allow the construction of an axially symmetric polarimeter. 2) The use of thin silicon strip detectors (SSDs) to identify the scattering processes occurring in the magnets. 3) The use of several polarimeter layers behind each other to increase the efficiency of the polarimeter. This also opens the way to polarimetry of the secondary particles created in the polarimeter. The first ingredient is more or less a premise to the third one.

The test of thin silicon strip detectors (SSDs) as identifiers of the scattering processes in the magnetic layers formed the second objective of this thesis. Feasibility studies were performed by using one NdFe layer sandwiched between four SSDs as a Møller polarimeter. As mentioned in the previous section the identification of Møller scattering events was poor at the energies offered by the ^{106}Ru/Rh source. Around 65% the 1122-events, which should signal Møller interactions in the NdFe target, were not related to an interaction in the target and contributed to a polarization insensitive background. The conclusion from the experiments and the Monte Carlo simulation of it is that at energies below 3.5 MeV the discrimination scheme is not working effectively.

The data from experiments with on-line produced ^{12}B (13 MeV β^-) and ^{12}N (16 MeV β^+) sources were hampered by experimental problems: the background resulting from the production of the sources did not allow the extraction of a scattering asymmetry. However, Monte Carlo simulations of the basic layer as a polarimeter for electrons and photons with energies from 10 MeV to 90 MeV showed that the non-target related background is reduced considerably at energies above 10 MeV: for electrons to around 2% and for photons to below 16%. The use of a thicker NdFe target (1 mm instead of 0.5 mm) at these energies was beneficial for this background reduction. The

conclusion is that event-recognition is in principle possible at these higher energies.

The simulations give information on the capabilities of a basic layer as part of a multi-layered polarimeter. The scattering asymmetry varies from -0.4 to -0.1 for electrons and -0.2 to -0.05 for photons when the energy increases from 10 MeV to 90 MeV. The detection efficiency for the events of interest was 1 to 2%. The figure of merit of the basic layer was 10^{-6} to 10^{-7} for both electrons and photons. The depolarization of an initially polarized beam is small. Taken together, these considerations allow the conclusion that the use of multiple layers is in principle possible: the multi-layered polarimeter becomes promising at energies between 10 and 100 MeV; feasibility test in this regime may be rewarding for future experiments on test of fundamental laws of physics.

7.3 The way to go

The project started in the second half of 1992 with an orientation on new items like suitable SSDs, high-quality NdFe and simulation tools which might include polarization features. At that time, the appropriate way to demonstrate the feasibility of the polarimeter seemed to be a 'quick test' with a single layer of the proposed polarimeter. Now, in the first quarter of 1997, it is clear that things were more complicated than anticipated. It turned out that computer simulations were necessary to explain the results. Looking back with the present knowledge, the program to perform these simulations should have been developed before the experiments were done even when the amount of work connected with this development is considered.

From the simulations it is clear that future experiments must be done at energies above 10 MeV. If ^{12}B- or ^{12}N-sources would be used again, a pulsed beam is necessary with data accumulation in between the beampulses. There should be no background from the beam during this period. However, an experiment with mono-energetic polarized electrons at a suitable electron-LINAC site is preferable. Another possibility is the use of β-decay electrons or positrons from muons.

At the time the SSDs for the experiments were developed there were no reliable self-triggering SSDs available. At present, these self-triggering strip-detectors can be obtained. Their application is desirable for several reasons. First, the efficiency of the polarimeter will be increased by including events

of interest which were not detected by the trigger detector. Second, the strip signals themselves can provide the readout trigger. This allows an on-line selection of data of interest. This reduces the amount of data to be stored and allows, in principle, a higher countrate. Third, the normalization of the data can be based on the strips in front of the NdFe scattering target, making the calibration polarization insensitive.

Finally, a remark on using the present prototype polarimeter layer in an experiment in which polarized electrons or photons with an energy of 10 MeV to 90 MeV are emitted. The relation between the number of particles on the polarimeter (N_{inc}) and the accuracy in the measured beam polarization (ΔP_b) follows from equation 2.3 and 2.4

$$N_{inc} = \frac{1}{(\Delta P_b)^2 \cdot \mathrm{FOM}}, \tag{7.1}$$

where FOM is the figure of merit of the polarimeter. The number of particles needed to arrive at an accuracy of $\Delta P_b = 0.05$ is $1/(0.05^2 \times 5 \cdot 10^{-7}) = 8 \cdot 10^8$, where for the FOM the results from the simulations discussed in section 6.6 are used. If the data acquisition of the polarimeter could be improved to handle a maximum eventrate of 1 kHz, it would take approximately 10 days to arrive at the desired accuracy. If multiple polarimeter layers are used together this time can be reduced. This would open the way for experiments with an eventrate below 1 kHz to be completed in a reasonable amount of time. The FOM can be increased further by incorporating polarimetry of the secondary particles of the electromagnetic shower into the polarimeter. The development of the polarimeter into this direction will take some time, manpower and investments. As always, some research remains to be done!

Appendix A

GEANT extensions and basis definitions

A.1 Data structures for polarization

In order to keep track of the polarization of a particle the data structures JSTAK and JKINE were modified. In JSTAK the information on the particles created during tracking can be stored. Normally it is a LIFO (Last In First Out) stack and the stored information of the secondary particle is lost as soon as the particle is taken from the stack for transportation. The data structure JKINE is more permanent. It contains the kinematics of a particle and the vertex to which this kinematics is connected. The information is kept until all the particles in the event are tracked. The initial kinematics of the event is also stored in this structure. Figure A.1 and A.2 show the modified data structures JSTAK and JKINE, respectively.

Storing the secondaries in JSTAK or JKINE is done by making a call to the subroutine GSKING which in turn calls the subroutine GSSTAK which handles the actual storing of the information. The initial kinematics of the event is stored in JKINE via the subroutine GSKINE. Besides the subroutines GSKING, GSSTAK and GSKINE, the routines GSVERT, GFKINE, GLUND, GPKINE, GLTRAC GTREVE and GPCXYZ were modified to handle the polarization information. The subroutines GSKINE and GFKINE have an extra 3-dimensional vector (REAL) inserted on the input line after the momentum vector. It represents the polarization of the particle in the particle frame.

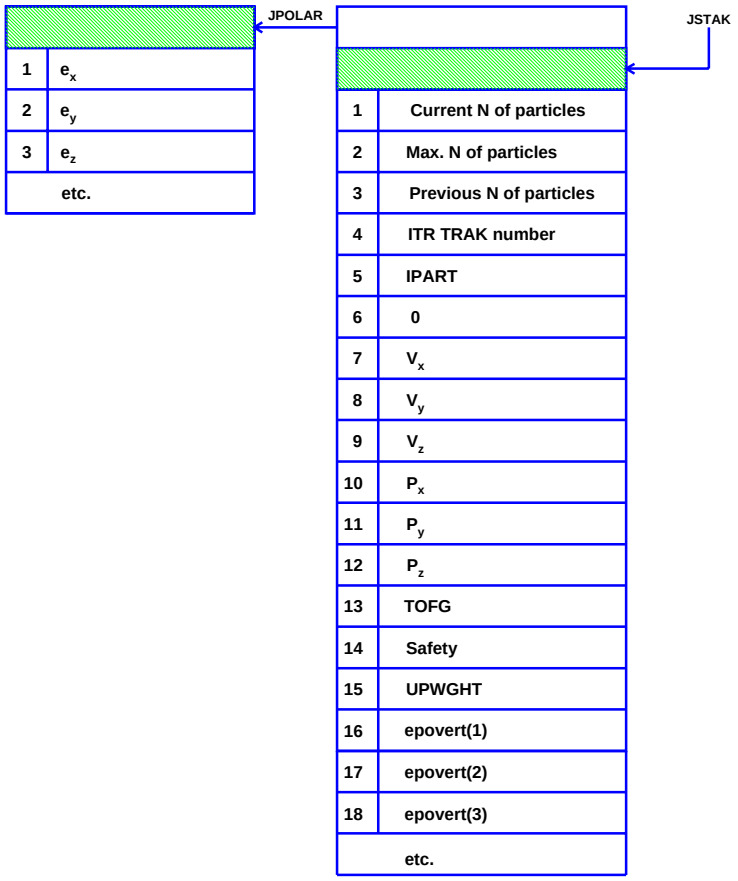

Figure A.1: *Modified data structure JSTAK.*

The polarization vector of a particle is available via additional common blocks: To GCKINE, the COMMON block with the kinematics of the current track, was added: COMMON/GCKIN1/EPOVERT(3) were EPOVERT is the polarization of the particle in the particle frame at the origin vertex. To GCKING, the COMMON block with the kinematics of the generated secondaries, was added: COMMON/GCKIN4/GPOL(3,MXGKIN) were GPOL is the polarization vector of Ith particle in the particle frame. And to GCTRAK, the COMMON block with the track parameters at the end of a tracking step, was added: COMMON/GCTEPO/EPOLA(3) were EPOLA is the polarization vector at the end of the current tracking step relative to the particle basis.

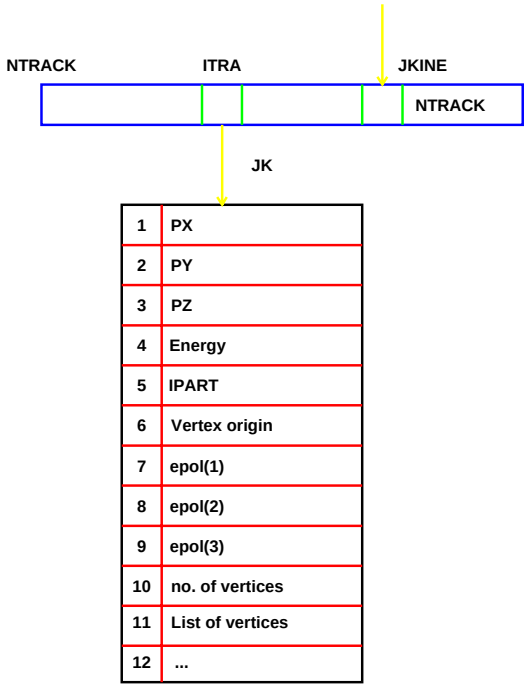

Figure A.2: *Modified data structure JKINE.*

The graphics routines were modified to make a drawing of the polarization vector along the track possible. The data structure JXYZ contains the data used to display tracks. The modified structure of JXYZ is shown in figure A.3. The routines GDPART, GDTRAK, GDXYZ, GKXYZ, GSXYZ and GPJXYZ were also changed for this purpose.

A.2 The particle basis

Definition of the particle basis (x_p,y_p,z_p) relative to the Mother Reference System (MRS) (X,Y,Z) of GEANT

- z_p is in the direction of the particles motion $(v1, v2, v3)$ (the vector is normalized),
- x_p-axis is parallel to XZ-plane, and
- Y-axis is parallel to $y_p z_p$ plane.

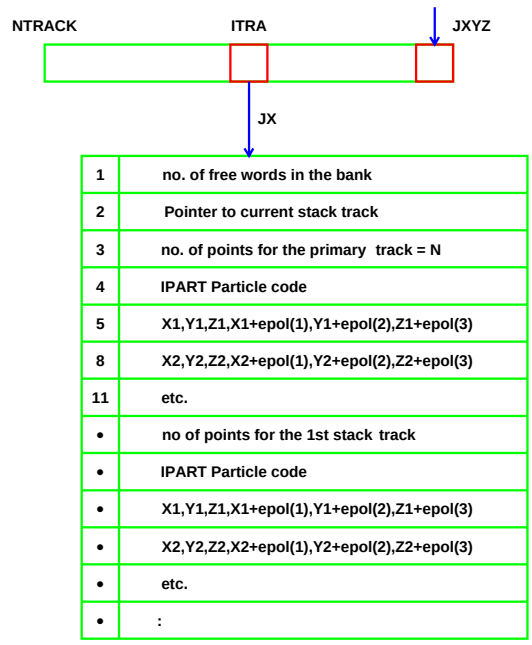

Figure A.3: *Modified data structures JXYZ.*

The particle basis is found starting from the MRS by rotating it over an angle ϕ around Y-axis in the XZ-plane followed by a rotation around the x_p-axis over θ out of the XZ-plane, where ϕ and θ are defined as

$$\begin{aligned}
\sin\phi &= \frac{v1}{\sqrt{v1^2+v3^2}}, \\
\cos\phi &= \frac{v3}{\sqrt{v1^2+v3^2}}, \\
\sin\theta &= \frac{v2}{\sqrt{v1^2+v2^2+v3^2}}, \\
\cos\theta &= \frac{\sqrt{v1^2+v3^2}}{\sqrt{v1^2+v2^2+v3^2}}.
\end{aligned}$$

The particle basis is

$$\begin{aligned}
x_p &= (\cos\phi, 0, -\sin\phi), \\
y_p &= (-\sin\phi\sin\theta, \cos\theta, -\cos\phi\sin\theta), \\
z_p &= (v1, v2, v3).
\end{aligned}$$

Table A.1: *Frame in which the polarization or asymmetry is calculated.*

process	polarization	calculated in frame of
Compton scattering	asymmetry	incoming photon
	photon in	incoming photon
	photon out	outgoing photon
	electron out	incoming photon
Møller/Bhabha scattering	asymmetry	incoming electron/positron
	electron/positron in	incoming electron/positron
	electron/positron out	outgoing electron/positron
positron annihilation	asymmetry	incoming positron
bremsstrahlung	electron in/out	outgoing photon
	photon out	outgoing photon
pair creation	photon in	incoming photon
	electron/positron out	incoming photon

If the particle moves along the Y-axis $\phi = 0$ and $\theta = 90$ degrees. A rotation is positive if it points from x to y, y to z or z to x.

A.3 The scattering basis

The scattering basis (x_{sc},y_{sc},z_{sc}) is defined as

- The $x_{sc}z_{sc}$-plane is the scattering plane of the process.
- The z_{sc}-axis is in the direction of the incoming particle.
- The basis vectors are unit vectors and form a right handed coordinate system.

Before and after the calculation of the polarization transfer or scattering asymmetry, the polarization of the particles is given relative to the coordinate system as given in table A.1. The rotation matrices 3.14 and 3.15 are used to go from the particle basis to the scattering basis and vice versa.

Appendix B

The macroscopic cross-section for Møller scattering

The differential cross section for Møller scattering is given by [88]

$$\frac{d\sigma}{dw} = \frac{2\pi r_0^2 m}{\beta^2(E-m)}\left(\frac{1}{w^2} + \frac{1}{(1-w)^2} + (\frac{\gamma-1}{\gamma})^2 - \frac{2\gamma-1}{\gamma^2}\frac{1}{w(1-w)}\right), \quad \text{(B.1)}$$

where $w = T/(E-m)$, T is the kinetic energy of one of the electrons after the scattering and E is the initial total energy. The value of w can be confined to $0 < w < 1/2$ because in Møller scattering the electrons are indistinguishable. The total cross section is found by integration over w

$$\begin{aligned} \sigma &= \int_{w=x}^{w=1/2} \frac{d\sigma}{dw} dw \qquad \text{(B.2)} \\ &= \frac{2\pi r_0^2 m}{\beta^2(E-m)}\left(\frac{1}{x} - \frac{1}{1-x} + (\frac{\gamma-1}{\gamma})^2(\frac{1}{2}-x) - \frac{2\gamma-1}{\gamma^2}\log(\frac{1-x}{x})\right). \end{aligned}$$

where $x = T_c/(E-m)$ and T_c is the kinetic energy cutoff for generating a δ-electron. For $T_c \to 0$ the integral diverges. The macroscopic cross-section Σ is:

$$\Sigma = \frac{N_{Av}\rho N_e \sigma}{A}, \quad \text{(B.3)}$$

where N_{Av} is Avogadro's constant, ρ is the density, A the atomic weight and N_e the number of electrons. For $T_c = 100$ keV this cross section is given for NdFe in figure B.1. Above 10 MeV the cross section is ≈ 5.2 cm^{-1}. The

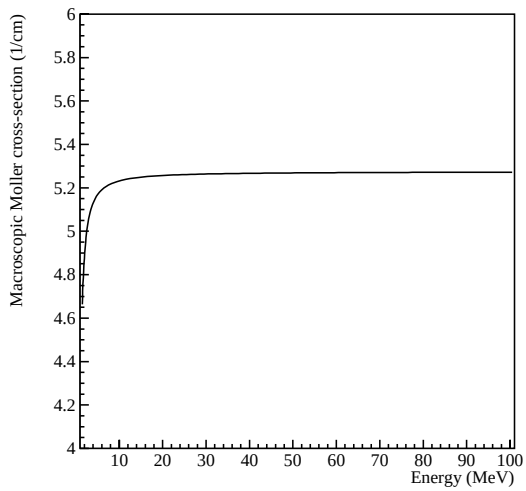

Figure B.1: *The macroscopic Møller cross-section in $Nd_2Fe_{14}B$ for a kinetic energy cutoff of 100 keV.*

probability of travelling through a distance d in NdFe without scattering is

$$P(d) = e^{-\Sigma d}. \tag{B.4}$$

This gives $P(0.5mm) = 0.77$ i.e., 77% of the electrons do not undergo a Møller interaction in which the secondary electron obtains at least 100 keV kinetic energy.

Bibliography

[1] H.A. Tolhoek. Electron polarization, theory and experiment. *Reviews of Modern Physics*, 28:277–298, 1956.

[2] R.L. Garwin et al. Space properties of the π Meson. *Physical Review*, 108(6):1589–1593, 1957.

[3] H. Burkard et al. Muon Decay: Measurement of the positron polarization and implications for the spectrum shape parameter π, V-A and T-invariance. *Physics Letters*, 150B:242–246, 1985.

[4] J. van Klinken. Some measurements on depolarization and scattering of electrons in thick absorbers. *Nuclear Physics*, 75:161, 1966.

[5] J. Kessler. *Polarized Electrons*. Springer Series on Atoms and Plasmas. Springer Verlag, Berlin Heidelberg, 2nd edition, 1985.

[6] J. Sromicki et al. Study of time reversal violation in β decay of polarized ^{8}Li. *Physical Review C*, 53:932–955, 1996.

[7] B. Wagner et al. A Møller polarimeter for CW and pulsed intermediate energy electron beams. *Nuclear Instruments and Methods*, A294:541–548, 1990.

[8] J. Arrington et al. A variable Møller polarimeter at the MIT-Bates Linear Accelerator Center. *Nuclear Instruments and Methods*, A311:39–48, 1992.

[9] D.P. Barber et al. The HERA polarimeter and the first observation of electron spin polarization at HERA. *Nuclear Instruments and Methods*, A329:79–111, 1993.

[10] N. Kalantar-Nayestanaki. *Plans for bremsstrahlung experiments at AGOR.* In 'Workshop on NN bremsstrahlung and polarization observables', Internal Report KVI 180i, Groningen, 1992.

[11] V. Herrmann. *Private Communication.*

[12] Several authors. *International workshop: Large experiments at low energy hadron machines.* PSI, Villigen, 1994.

[13] R. Prieels et al. *PSI-Proposal R-97-06.* PSI, Villigen, 1997.

[14] W.H. McMaster. Polarization and the Stokes parameters. *American Journal of Physics*, 22(6):351–362, 1954.

[15] W.H. McMaster. Matrix representation of polarization. *Reviews of Modern Physics*, 33(1):8–29, 1961.

[16] K. Flöttmann. *Investigations toward the development of polarized and unpolarized high intensity positron sources for linear colliders.* PhD thesis, Universität Hamburg, 1993.

[17] M. Goossens. *GEANT - Detector Description and Simulation Tool.* CERN Program Library Long Writeup W5013, Geneva, 1993.

[18] H.W. den Bok et al. A GEANT extension for polarized neutron-proton scattering. *Computer Physics Communications*, 74:375–380, 1993.

[19] J. van Klinken. Double scattering of electrons. *Nuclear Physics*, 75:161–188, 1966.

[20] V.A. Wichers et al. Bounds on Right-Handed Currents from Nuclear Beta Decay. *Physical Review Letters*, 58(18):1821–1824, 1987.

[21] A.S. Carnoy et al. Limits on Nonstandard Weak Currents from the Positron Decays of ^{14}O and ^{10}C. *Physical Review Letters*, 65:3249–3252, 1990.

[22] A.S. Carnoy et al. Limits on Nonstandard Weak Currents from the Polarization of ^{14}O and ^{10}C Decay Positrons. *Physical Review C*, 43:2825–2834, 1991.

[23] H. Frauenfelder and R.M. Steffen. *The helicity of β-particles.* Page 1431-1452 in [78].

[24] K.W. McVoy and F.J. Dyson. Longitudinal polarization of bremsstrahlung and pair production at relativistic energies. *Physical Review*, 106:1360–1361, 1957.

[25] T.J. Gay et al. Extrapolation procedures in Mott electron polarimetry. *Review of Scientific Instruments*, 63:114–130, 1992.

[26] T.J. Gay and F.B. Dunning. Mott electron polarimetry. *Review of Scientific Instruments*, 63:1635–1651, 1992.

[27] T.J. Gay. Electron polarimetry. *Experimental Methods in the Physical Sciences*, 29A:231–252, 1995.

[28] G. Gerber et al. Precision measurement of positron polarization in ^{68}Ga decay based on the use of a new positron polarimeter. *Physical Review D*, 15(5):1189–1193, 1977.

[29] M. Skalsey et al. New method for precision positron polarimetry: first results and future applications. *Physical Review*, 49:708–711, 1982.

[30] M. Skalsey et al. Longitudinal polarization of positrons in ^{22}Na decay. *Physical Review C*, 32:1014–1025, 1985.

[31] N. Severijns et al. Bounds on right-handed currents from a relative β-polarization measurement with polarized ^{107}In. *Nuclear Physics A*, 553:827c–830c, 1993.

[32] M. Allet et al. Search for right-handed weak currents in the β-asymmetry-polarization correlation from ^{12}N decay. *Physics Letters B*, 383:139–144, 1996.

[33] H. Schopper. Measurement of circular polarization of γ-rays. *Nuclear Instruments*, 3:158–176, 1958.

[34] L.W. Fagg and S.S. Hanna. Polarization measurements on nuclear gamma rays. *Reviews of Modern Physics*, 31:711–758, 1959.

[35] V.A. Wichers. *Mirror symmetry and positron handedness in beta decay.* PhD thesis, University of Groningen, 1988.

[36] J. van Klinken et al. A fourfold Bhabha/Møller polarimeter for positrons/electrons. *Nuclear Instruments and Methods*, A286:202–213, 1990.

[37] F. Corriveau et al. Measurement of the positron longitudinal polarization in muon decay. *Physical Review D*, 24(7):2004–2007, 1981.

[38] G. Barbiellini et al. Measurement of the polarization of the Frascati 1-GeV electron synchrotron γ-ray beam from a diamond crystal radiator. *Physical Review*, 9:396–399, 1962.

[39] M. Kobayashi et al. Polarization Measurements of Coherent Bremsstrahlung from a Single Crystal of Silicon. *Journal of the Physical Society of Japan*, 35:1569–1578, 1973.

[40] H. Olsen and L.C. Maximon. Pair Production as an Analyser of Circular Polarization of γ Rays from Neutral Particle Decays. *Nuovo Cimento*, 24(1):186–189, 1962.

[41] I. Endo et al. Detection of recoil electrons in triplet photoproduction. *Nuclear Instruments and Methods*, 208:144–146, 1989.

[42] Y. Iwata et al. New polarimeter for high energy gamma-rays. *Nuclear Instruments and Methods*, 336:146–149, 1993.

[43] L.A. Page and M. Heinberg. Measurement of the longitudinal polarization of positrons emitted by Sodium-22. *Physical Review*, 106:1220–1224, 1957.

[44] L. Dick et al. A novel efficient method for measuring the polarization of positrons. *Physics Letters*, 3:326–329, 1963.

[45] F.W. Lipps and H.A. Tolhoek. Polarization phenomena of electrons and photons. I. *Physica*, 20:85–98, 1954.

[46] F.W. Lipps and H.A. Tolhoek. Polarization phenomena of electrons and photons. II. *Physica*, 20:395–405, 1954.

[47] S.B. Gunst and L.A. Page. Compton scattering of 2.62-MeV gamma rays by polarized electrons. *Physical Review*, 92:970–973, 1953.

[48] A.M. Bincer. Scattering of longitudinally polarized fermions. *Physical Review*, 107(5):1434–1438, 1957.

[49] G.W. Ford and C.J. Mullin. Scattering of polarized Dirac particles on electrons. *Physical Review*, 108:477–481, 1957.

[50] H. Frauenfelder and A. Rossi. *Determination of the polarization of electrons and photons.* Page 214-274 in [121].

[51] L.A. Page. Electron and positron polarization. *Reviews of Modern Physics*, 31:759–781, 1959.

[52] H. Frauenfelder. Parity and Electron Polarization: Møller Scattering. *Physical Review*, 107:643–644, 1957.

[53] J. van Klinken et al. Mini Orange spectrometers for in- and off-beam observation of conversion electrons. *Nuclear Instruments and Methods*, 130:427–441, 1975.

[54] L.A. Page. Polarization effects in the two-quantum annihilation of positrons. *Physical Review*, 106(3):394–397, 1957.

[55] McMaster. Polarization Phenomena for Positron Annihilation-in-Flight. *Nuovo Cimento*, 17:395–414, 1960.

[56] H. Mahler. *Messung der longitudinal-polarisation der positronen aus der zerfall positiver myonen.* PhD thesis, Eidgenössishen Technischen Hochschule Zürich, 1980.

[57] P.C. Macq et al. Helicity of the electron and positron in muon decay. *Physical Review*, 112:2061–2071, 1958.

[58] A. Buhler et al. A measurement of the e^+ polarisation in muon decay: the e^+ annihilation method. *Physics Letters*, 7:368–371, 1963.

[59] S. Bloom et al. Measurement, by bremsstrahlung transmission of the polarisation of e^+ from $\mu^+ \rightarrow e^+ + \nu_e + \bar{\nu}_\mu$. *Physics Letters*, 8:87–89, 1964.

[60] J. Duclos et al. Measurement of the e^+ polarisation in muon decay by means of Bhabha scattering. *Physics Letters*, 9:62–65, 1964.

[61] D.M. Schwartz. Helicity of electrons μ^- decay. *Physical Review*, 162:1306–1319, 1967.

[62] L. Dick et al. Mesure de la polarisation des positrons emis dans les desintegration de Na^{22}, B^8 et μ^+. *Physics Letters*, 7:150–153, 1963.

[63] F. Corriveau et al. Does the positron from muon decay have transverse polarization? *Physics Letters*, 129B:260–264, 1983.

[64] H. Burkard et al. Muon decay: measurement of the transverse positron polarization and general analysis. *Physics Letters*, 160B:343–348, 1985.

[65] W. Fetscher and H.J. Gerber. *Precision measurements in Muon and Tau decays published.* In [122].

[66] M. Swartz et al. Observation of target electron momentum effects in single-arm Møller polarimetry. *Nuclear Instruments and Methods*, A363:526–537, 1995.

[67] P.S. Cooper et al. Polarized electron-electron scattering at GeV energies. *Physical Review Letters*, 34:1589–1592, 1975.

[68] W. Brefeld et al. Measurement of the polarization degree of accelerated polarized electrons at the 2.5 GeV synchrotron in Bonn for energies between 0.85 and 2 GeV. *Nuclear Instruments and Methods*, 228:228–235, 1985.

[69] K.B. Beard et al. Measurement of the polarization of a pulsed electron beam with a Møller polarimeter in the coincidence mode. *Nuclear Instruments and Methods*, A361:46–52, 1995.

[70] L.G. Levchuk. The intra-atomic motion of bound electrons as a possible source of the systematic error in electron beam polarization measurements by means of a Møller polarimeter. *Nuclear Instruments and Methods*, A345:496–499, 1994.

[71] A. Feltham. Comments on "Measurement of the polarization of a pulsed electron beam with a Møller polarimeter in the coincidence mode". *Nuclear Instruments and Methods*, A370:644–645, 1996.

[72] C.N. Yang. Possible experimental determination of whether the neutral meson is scalar or pseudoscalar. *Physical Review*, 77:722–723, 1950.

[73] T.H. Berlin and L. Madansky. On the detection of γ-ray polarization by pair production. *Physical Review*, 78:623, 1950.

[74] G.C. Wick. Detection of gamma-ray polarization by pair production. *Physical Review*, 81:467–468, 1951.

[75] L.C. Maximon and Haakon Olsen. Measurement of linear photon polarization by pair production. *Physical Review*, 126:310–319, 1962.

[76] S.R. Kel'ner. Dependence of the azimuthal asymmetry of pair production plane on the photon polarization. *Soviet Journal of Nuclear Physics*, 10:349–351, 1970.

[77] V.F. Boldyshev and Yu.P. Perensun'ko. Electron-positron pair photoproduction on electrons and analysis of proton beam polarization. *Soviet Journal of Nuclear Physics*, 14:576–578, 1972.

[78] K. Siegbahn. *Alpha-, Beta-, Gamma-ray spectroscopy.* North-Holland Publishing Company, Amsterdam, 1965.

[79] Several authors. *Spin 96 Book of abstracts.* Vrije Universiteit Amsterdam, 1996.

[80] J.D. Jackson. *Classical Electrodynamics.* John Wiley & Sons, Inc., New York, 2nd edition, 1975.

[81] A. Messiah. *Quantum Mechanics Vol. II.* North Holland Publishing Company, Amsterdam, 3rd edition, 1965.

[82] L.H. Ryder. *Quantum Field Theory.* Cambridge University Press, Cambridge, 1st edition, 1985.

[83] E.P. Wigner. Relativistic invariance and quantum phenomena. *Reviews of Modern Physics*, 29:255–269, 1957.

[84] M.E. Rose. *Relativistic Electron theory.* John Wiley & Sons, Inc., USA, 1st edition, 1961.

[85] U. Fano. Remarks on the classical and quantum-mechanical treatment of partial polarization. *Journal of the Optical Society of America*, 39(10):859–863, 1949.

[86] G. Holzwarth. Polarization effects in electron-electron and positron-electron scattering. *Zeitschrift für Physik*, 191:354–359, 1966.

[87] P. Stehle. Calculation of electron-electron scattering. *Physical Review*, 110(6):1458–1460, 1958.

[88] J.M. Jauch and F. Rohrlich. *The theory of photons and electrons.* Springer-Verlag, New York, 2nd edition, 1975.

[89] H. Olsen and L.C. Maximon. Photon and electron polarization in high-energy bremsstrahlung and pair production with screening. *Physical Review*, 114:887–904, 1959.

[90] H. Davies, H.A. Bethe and L.C. Maximon. Theory of Bremsstrahlung and Pair Production. II. Integral Cross Section for Pair Production. *Physical Review*, 93(4):788–795, 1954.

[91] W.R. Nelson et al. *The EGS4 code system.* Stanford University, 1985.

[92] H.W. Koch and J.W. Motz. Bremsstrahlung cross-section formulas and related data. *Review Mod. Phys.*, 31(4):920–955, 1959.

[93] H.A. Bethe and L.C. Maximon. Theory of bremsstrahlung and pair production. I. differential cross section. *Phys. Review*, 93(4):768–784, 1954.

[94] Several authors. *A Source Code Management System - CMZ - User's Guide & Reference Manual.* CERN Program Library Office, Geneva, 1989.

[95] S.M. Seltzer and M.J. Berger. Bremsstrahlung spectra from electron interactions with screened atomic nuclei and orbital electrons. *Nuclear Instruments and Methods*, B12:95–134, 1985.

[96] Y.S. Tsai. Pair Production and Bremsstrahlung of Charged Leptons. *Reviews of Modern Physics*, 46(4):815–851, 1974.

[97] Y.S. Tsai. Erratum: Pair Production and Bremsstrahlung of Charged Leptons. *Reviews of Modern Physics*, 49(2):421–423, 1977.

[98] J.W. Motz, H.A. Olsen and H.W. Koch. Pair Production by Photons. *Reviews of Modern Physics*, 41(4):581–639, 1969.

[99] J.F. Herbst. $R_2Fe_{14}B$ materials: intrinsic properties and technological aspects. *Reviews of Modern Physics*, 63(4):819–898, 1991.

[100] S. Chikazuma. *Magnetism.* John Wiley & Sons, Inc., New York, 2nd edition, 1965.

[101] D. Jiles. *Introduction to Magnetism and Magnetic Materials.* Chapman and Hall, London, 1st edition, 1991.

[102] S. Hirosawa et al. Magnetization and magnetic anisotropy of $R_2Fe_{14}B$ measured on single crystals. *Journal of Applied Physics*, 59(3):873–879, 1986.

[103] M. Sagawa et al. New material for permanent magnets on a base of Nd and Fe. *Journal of Applied Physics*, 55:2083–2087, 1984.

[104] K.D. Durst and H. Kronmüller. Determination of intrinsic magnetic material parameters of $Nd_2Fe_{14}B$ from magnetic measurements of sintered $Nd_{15}Fe_{77}B_8$. *Journal of Magnetism and Magnetic Materials*, 59:86–94, 1986.

[105] E. Steingroever and S. Siebert. *Magnetische Messungen mit de Helmholtzspule und der Potentialspule*, 1994. Ausgabe Magnet-Physik Dr. Steingroever GmbH.

[106] J.M.D. Coey. Applying Permanent Magnets. *Europhysics News*, 27:186–188, 1996.

[107] J.M. Hoogduin et al. Calibration of electron and positron polarimeters at 10 to 15 MeV. *Nuclear Instruments and Methods*, A379:176–178, 1996.

[108] J. Bardeen and W.H. Brattain. The Transistor, A Semi-Conductor Triode. *Physical Review*, 74:230–231, 1948.

[109] K.G. McKay. Electron-Hole Production in Germanium by Alpha-Particles. *Physical Review*, 84:829–832, 1951.

[110] A.S. Schwarz. Heavy flavour physics at colliders with silicon strip vertex detectors. *Physics Reports*, 238:1–133, 1994.

[111] E.M. Schooneveld et al. A silicon strip readout system for a new electromagnetic polarimeter. *Nuclear Instruments and Methods*, A348:461–464, 1994.

[112] E.M. Schooneveld. *Report of the Silicon Strip Detector readout system used in the NdFe polarimeter.* Stratech report TUDSIR9401, Technische Universiteit Delft, 1994.

[113] E. Beuville et al. AMPLEX, A low-noise, low-power analog CMOS signal processor for multielement silicon particle detectors. *Nuclear Instruments and Methods*, A288:157–167, 1990.

[114] F. Zwarts. *EDAQ - An ELN based data acquisition system.* Groningen, 1991.

[115] F. Zwarts. *PAX - The KVI data reduction program.* Groningen, 1991.

[116] R. Brun and M. Goossens. *HBOOK - Statistical Analysis and Histogramming.* CERN Program Library Long Writeup Y205, Geneva, 1993.

[117] R. Brun et al. *PAW - Physics Analysis Workstation.* CERN Program Library Long Writeup Q121, Geneva, 1989.

[118] H.K.W. Leegte et al. Calibration of phoswich detectors. *Nuclear Instruments and Methods*, A313:26–30, 1992.

[119] R.W. Peterson and N.W. Glass. Some ^{12}N and ^{12}B beta-decay measurements. *Physical Review*, 130(1):292–298, 1963.

[120] N.W. Glass and R.W. Peterson. Direct comparison of the ^{12}B and ^{12}N spectra. *Physical Review*, 130(1):299–305, 1963.

[121] Editors L.C.L. Yuan and C.S. Wu. *Methods of Experimental Physics Volume 5 Nuclear Physics Part B.* Academic Press, New York and London, 1963.

[122] Editor P. Langacker. *Precision Tests of the Standard Electroweak Model.* World Scientific, Singapore, 1990.

List of publications

J.M. Hoogduin, E. Ditzel, A. Balanda, F.W.N. de Boer, H. Bokemeyer, J. Gerl, K. Heyde, J. van Klinken, A. Krasznahorkay, P. Salabura, H.J. Wollersheim, On the two first excited $K = 0$ bands in ^{238}U and ^{240}Pu, *Physics Letters*, B384:43-49, 1996.

J.M. Hoogduin, J. van Klinken, E.M. Schooneveld, A. Müller, O. Fröhlich, K.E. Stiebing, Calibration of electron and positron polarimeters at 10 to 15 MeV, *Nuclear Instruments and Methods*, A379:176-178, 1996.

E. Ditzel, J.M. Hoogduin, H. Backe, F.W.N. de Boer, H. Bokemeyer, M. Debowski, J. van Klinken, P. Salabura, H.J. Wollersheim, H.Xie, Doppler-corrected spectroscopy of conversion electrons with Mini-Oranges after heavy-ion collisions, *Nuclear Instruments and Methods*, A376:428-433, 1996.

E.M. Schooneveld, C.W.E. van Eijk, J. van Klinken, J.M. Hoogduin, P.M. Sarro, A. van den Boogaard, A Silicon Strip Readout System for a New Electromagnetic Polarimeter, *Nuclear Instruments and Methods*, A348:461-464, 1994.

J. van Klinken, A. Balanda, J.M. Hoogduin, H. Kaper, W.J. Meiring, H. Bokemeyer, F.W.N. de Boer, D. Kraft, K.E. Stiebing, Positron-electron Pair Spectrometry with Selective Mini-orange Devices, *Nuclear Instruments and Methods*, A320:508-518, 1992.

R.E. Warner, C.L. Carpenter, J.P. Fetter, W.F. Waite, H.W. Wilschut, J.M. Hoogduin, Total Nuclear Reaction Probability of 270 to 390 MeV ^{14}N Ions in Si and CsI, *Physical Review*, C48:245-249, 1993.

Samenvatting: Electron, Positron en Foton Polarimetrie

Het beeld dat wij hebben van de wereld om ons heen, wordt voor een groot gedeelte bepaald door de stand van de techniek. In den beginne waren het onze zintuigen die onze ideeën over de omgeving bepaalden. We keken omhoog naar de sterren en genoten van het uitzicht. Dat doen we gelukkig nog steeds maar we zijn sinds een half millennium geneigd om de zaken wat beter te willen bekijken. Voor het sterrenkijken begint dat met een verrekijker en eindigt dat vandaag de dag met de Hubble telescoop. Instrumenten zijn onmisbaar geworden bij het 'werken aan de grenzen van het weten'. Dat geldt zeker voor kernfysisch onderzoek. Onze 'natuurlijke detectoren' schieten hopeloos tekort om ook maar iets te kunnen zien van de deeltjes die in deze tak van de natuurkunde worden bestudeerd. Zonder speciaal voor dit doel gemaakte detectoren kan er niets worden onderzocht. De ontwikkeling van een nieuw meetinstrument waarmee de polarisatie van electronen, positronen en fotonen kan worden gemeten, is het onderwerp van dit proefschrift.

Kernfysische experimenten

In veel kernfysische experimenten botsen deeltjes met hoge snelheid op elkaar. De brokstukken van zo'n botsing, ook weer deeltjes of straling, geven informatie over het verloop van de botsing. Zo wordt bijvoorbeeld gekeken naar de snelheid van de brokstukken en hoe ze verdeeld zijn over de ruimte. Een voorbeeld van straling is zichtbaar licht. Bij de beschrijving van straling spelen fotonen, lichtdeeltjes zonder massa, een rol. Ook de toestand waarin de brokstukken zich bevinden kan informatie geven over de botsing. Het vastleggen van deeltjestoestanden is een tak van de kernfysica op zichzelf.

De deeltjes die in dit proefschrift een belangrijke rol spelen zijn electronen, positronen en fotonen. Van bundels van deze deeltjes willen we de polarisatietoestand meten. Wat dit betekent, wordt geïllustreerd aan de hand van het electron. In een sterk vereenvoudigd beeld kan een electron worden voorgesteld als een rondspinnende tol. De richting van de as van de tol stelt in dit beeld de spinrichting van het electron voor. Het meten van spintoestanden gebeurt met een polarimeter en heet polarimetrie. Er wordt gesproken van een gepolariseerde bundel electronen als de spins van de individuele electronen overwegend in een bepaalde richting wijzen.

Aanleiding voor het onderzoek

De aanleiding voor een onderzoek naar de mogelijkheden van een nieuwe polarimeter is gelegen in een onderzoeksprogramma op het KVI waarin de botsing tussen protonen wordt bestudeerd. Soms wordt er bij een botsing van twee protonen, een derde deeltje, een foton, uitgezonden. Het blijkt dat de polarisatietoestand van dit foton iets kan vertellen over de manier waarop de botsing is verlopen. Door het ontbreken van een geschikte polarimeter heeft nog geen enkele onderzoeksgroep geprobeerd de polarisatiegraad van de fotonen te meten. Een polarimeter zou een waardevolle, aanvullende en geheel nieuwe meetmethode opleveren. Een eerste verkenning leerde dat een dergelijke polarimeter ook geschikt zou zijn voor het meten van de polarisatiegraad van electronen en positronen.

Principe van een polarimeter

Er bestaan verschillende manieren om een polarimeter te maken. Een overzicht van de mogelijkheden wordt in het eerste deel van dit proefschrift gegeven. In de beoogde polarimeter ondergaan de electronen, positronen of fotonen waarvan de polarisatiegraad moet worden bepaald een botsing die gevoelig is voor de spintoestand van deze deeltjes. Uit de theorie blijkt dat in veel gevallen de botsing pas polarisatie-gevoelig is, als de deeltjes waarmee wordt gebotst ook een gerichte spin hebben. Een deel van de electronen in de atoomschillen van magnetische materialen heeft deze eigenschap. In het hart van veel polarimeters is daarom een materiaal met magnetische eigenschappen aanwezig. Daarnaast bestaat een polarimeter uit detectoren waarmee kan worden vastgesteld of er een interessante, d.w.z. polarisatie-gevoelige, botsing heeft plaatsgevonden. Een van de moeilijkheden bij het ontwerpen

van een polarimeter is dat het aantal polarisatie-gevoelige botsingen maar een fractie is van alle botsingen die in het apparaat optreden. De detectoren in de polarimeter moeten dit kleine deel uit het totaal filteren. Het zoeken naar een speld in de hooiberg beschrijft de situatie aardig.

Opbouw van de polarimeter

Figuur S.1 toont de beoogde polarimeter. Het centrale gedeelte van het apparaat wordt gevormd door magneten die zijn gemaakt van neodynium, ijzer en een beetje boron, om precies te zijn $Nd_2Fe_{14}B$ (afgekort tot NdFe). De detectoren die de polarisatie-gevoelige botsingen in dit materiaal moeten identificeren zijn Silicium Strip Detectoren (SSDs). Zowel de NdFe magneten als de SSDs zijn niet eerder in een polarimeter gebruikt.

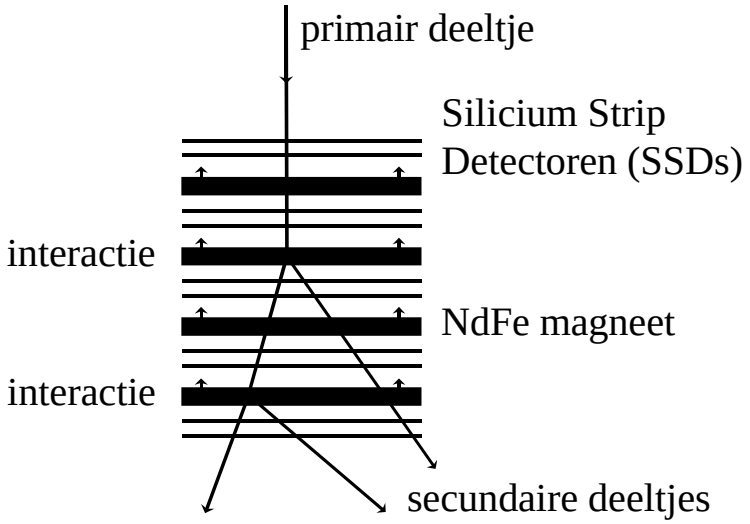

Figure S.1: *De beoogde polarimeter.*

De NdFe magneten zijn platte schijven van ongeveer een millimeter dikte en een diameter van 4 à 5 cm die loodrecht op hun oppervlak gemagnetiseerd kunnen worden (dit is in de figuur met pijltjes aangegeven). Dit laatste is een bijzondere eigenschap van het materiaal: meestal is het niet mogelijk de magnetisatierichting zonder hulp van externe magneetvelden permanent uit het vlak van de magneet te houden.

De SSDs zijn plakken silicium materiaal van minder dan een halve mil-

limeter dikte. Ze zijn onderverdeeld in evenwijdige stroken die elk apart als detector dienst doen. Wanneer een deeltje een SSD doorkruist zal de strip die wordt gepasseerd een signaal afgeven. Op deze manier wordt informatie verkregen over de positie van het deeltje bij het passeren van de detector. Om plaatsinformatie in twee richtingen te krijgen, worden steeds twee SSDs met de strips in gekruiste richtingen achter elkaar geplaatst. De sandwich van twee maal twee SSDs met één NdFe magneet er tussenin wordt in de getekende polarimeter een paar keer herhaald. Hierdoor neemt de gevoeligheid van de polarimeter toe: het aantal polarisatie-gevoelige botsing neemt namelijk toe met de aanwezige hoeveelheid magnetisch materiaal.

Figuur S.1 laat ook zien dat er tijdens de botsingen van het primaire deeltje in de polarimeter, deeltjes bijkomen: de zgn. secundaire electronen, positronen en fotonen. Er ontstaat een patroon dat lijkt op de vertakkingen van een boom en dat een 'electromagnetic shower' wordt genoemd. Tijdens een interactie kan de polarisatie van het primaire deeltje deels worden overgedragen op de secundaire deeltjes. Polarimetrie op deze secundaire deeltjes in een van de achterste sandwichlagen, is een tweede weg waarlangs de gevoeligheid van de polarimeter toeneemt.

Onderzoeksvragen

Om de realiseerbaarheid van de polarimeter te onderzoeken is een sandwich van vier SSDs en een NdFe magneet gebouwd. Met dit prototype werd het antwoord op twee vragen gezocht:

1 Zijn NdFe magneten geschikt als magnetisch materiaal in een polarimeter?

2 Hoe goed kunnen de SSDs de polarisatie-gevoelige botsingen uit alle voorkomende botsingen filteren?

Resultaten van het onderzoek

Om de eerste vraag te beantwoorden is een afschatting gemaakt van de hoeveelheid gerichte electronspins in NdFe magneten. Een eenheid $Nd_2Fe_{14}B$ bevat in totaal 489 electronen. Ongeveer 5% van deze electronen heeft zijn spin in dezelfde richting staan. Een NdFe magneet is opgebouwd uit vele eenheden $Nd_2Fe_{14}B$ die niet allemaal precies dezelfde oriëntatie hebben en bovendien

bevat een magneet altijd wat verontreinigingen van niet-magnetische materialen. Hierdoor is het effectief gerichte aantal electronspins in een NdFe magneet altijd kleiner dan de 5% per eenheid $Nd_2Fe_{14}B$. In de magneet die in de prototype polarimeter is gebruikt, bleek de effectieve polarisatie ongeveer 3.7% te bedragen.

De bruikbaarheid van het NdFe materiaal werd experimenteel getest met een bundel deeltjes waarvan de polarisatiegraad bekend is. De electronen die door sommige radioactieve bronnen worden uitgezonden zijn van nature gepolariseerd en kunnen worden benut als testbundel. Het nadeel van deze electronen is dat hun energie wat aan de lage kant is (voor electronen afkomstig van β-bronnen is deze energie maximaal 13.4 MeV); de polarimeter is uiteindelijk bedoeld voor deeltjes met een hogere energie (10 tot 100 MeV).

Uit de metingen werd niet duidelijk of NdFe magneten bruikbaar zijn als verstrooiend materiaal in de polarimeter. Het prototype bleek niet aantoonbaar gevoelig voor de polarisatie van de testbundel electronen. Er werd weliswaar een klein effect waargenomen, maar dat was niet statistisch relevant. Om dit te verklaren is het gedrag van de polarimeter met een computersimulatie bestudeerd. Daarvoor moest echter een programma worden ontwikkeld waarmee zo'n simulatie kan worden uitgevoerd. Programmatuur waarmee het gedrag van ongepolariseerde deeltjes in materie en waarmee de ontwikkeling van de 'electromagnetic shower' kan worden gevolgd, is gelukkig wel beschikbaar. Een dergelijk programmapakket is uitgebreid met polarisatiegevoeligheid. Hiertoe is allereerst de theorie om gepolariseerde electronen, positronen en fotonen en polarisatie-gevoelige botsingen te beschrijven, op een uniforme manier opgeschreven. Nadat ook het pakket geschikt was gemaakt voor de simulatie van gepolariseerde deeltjes, is deze theorie omgezet in programmacode.

Met de simulatie van de polarimeter kan worden verklaard waarom de polarimeter niet gevoelig is voor de polarisatie van de testbundel. Dit blijkt samen te hangen met het antwoord op de tweede onderzoeksvraag: Hoe goed kunnen de SSDs de polarisatie-gevoelige botsingen identificeren? Een groot gedeelte van de botsingen die als polarisatie-gevoelig werd aangewezen, bleek in werkelijkheid niet polarisatie-gevoelig te zijn. De verklaring hiervoor hangt samen met de lage energie van de testbundel elektronen. Het, op grond van de simulatie, verwachte effect komt goed overeen met het gemeten effect.

Simulaties van het gedrag van de polarimeter bij hogere energieën, laten zien dat de identificatie van de polarisatie-gevoelige botsingen bij deze energieën beter verloopt. De polarisatie-gevoeligheid die uit deze simulaties naar

voren komt, is redelijk. Toekomstig onderzoek zal moeten uitwijzen of de polarimeter zoals getekend in figuur S.1 een bruikbare uitbreiding zal zijn van het kernfysisch instrumentarium. Het ontwikkelde simulatiepakket kan daarbij een nuttige rol spelen.